THESIS FOR THE DEGREE OF DOCTOR OF PHILOSOPHY

Nonlinear Mechanics of Graphene and Mass-loading Induced Dephasing in Nanoresonators

JUAN ATALAYA

Department of Applied Physics
CHALMERS UNIVERSITY OF TECHNOLOGY
SE-412 96 Gothenburg, Sweden 2012

Nonlinear Mechanics of Graphene and Mass-loading Induced Dephasing in Nanoresonators

Juan Atalaya
ISBN 978-91-7385-740-6

Doktorsavhandlingar vid Chalmers tekniska högskola
Ny serie nr 3421
ISSN 0346-718X

Condensed Matter Theory
Department of Applied Physics
Chalmers University of Technology
SE-412 96 Gothenburg
Sweden
Telephone +46 (0)31 772 1000

Cover:
Graphene-based nanomechanical resonator subject to random mass loading caused by random adsorption of small molecules (blue spheres). The dotted circles indicate previous positions of the molecules trapped at one of the vibrational antinodes.

Typeset in LaTeX
Figures created using POV-Ray, MATLAB and Corel Draw.

Printed by Chalmers Reproservice
Chalmers University of Technology
Gothenburg, Sweden 2012

Nonlinear Mechanics of Graphene and Mass-loading Induced Dephasing in Nanoresonators

JUAN ATALAYA
Condensed Matter Theory
Department of Applied Physics
Chalmers University of Technology

ABSTRACT

I summarize the results of my research in the subjects of nonlinear mechanics of graphene resonators, mass-loading induced dephasing in nanomechanical resonators and spintronics-based mesoscopic heat engines for cooling the fundamental flexural mode of a CNT resonator.

This thesis consists of three parts. In the first part I present a mechanical description for monolayer graphene membranes. The equations of motion are derived in the long wavelength limit starting from an atomistic model, which accounts for the energy cost to change the length of the sp^2 covalent bonds and also the angle between neighboring bonds in graphene. I also propose to use nonlinear dynamics of square graphene resonators to measure the mass and position of a single adsorbed particle using only narrow-band frequency sensors.

In the second part, I consider the effects of random mass loading in nanomechanical resonators. Random mass loading leads to random modulation of the resonance frequency (dephasing process) of the vibrational eigenmodes of the resonator. I consider first the situation where the dephasing process is not affected by the motion of the resonator (no backaction). Here, the random mass loading is caused by adsorption, desorption and diffusion of small particles along the resonator. I discuss the method of interfering partial susceptibilities to calculate the susceptibility of underdamped vibrational eigenmodes. I find that the final shape of the eigenmode absorption spectrum line depends on the intensity and correlation time of the frequency noise. In the presence of dephasing, the eigenmode energy relaxation rate cannot be measured from the width of the absorption line. I also discuss a method to characterize the dephasing process. Then, I consider the case of backaction in the dephasing process for the case of particles diffusing along the resonator. The backaction is induced by an inertial force, which drives the particles towards the antinode(s) of the excited eigenmode. I show that dephasing subject to backaction can lead to bistability and rare interstate switching between small and large amplitude vibrational states (with the particles delocalized and localized at the antinode(s), respectively) if the particles diffuse comparatively fast. The diffusion induced bistability in driven resonators has a different origin from the conventional bistability and interstate switching, which occurs in driven nonlinear oscillators subject to a weak source of additive noise.

Finally, the third part deals with a proposal for a physical realization of

a mesoscopic heat engine which consists of two spin polarized leads held at different temperatures (heat reservoirs) linked by a CNT resonator in the presence of a nonuniform magnetic field. The latter induces spin-mechanical coupling between the electronic subsystem (two-level system inside the CNT) and the mechanical subsystem (fundamental flexural mode). One would expect that the effective temperature of the mechanical subsystem should be between the temperatures of the leads. However, I show that if the leads have spin polarization $\gtrsim 50$ % and the coupling between the mechanical subsystem and other baths is weaker than the spin-mechanical coupling, then it is possible for the effective temperature of the mechanical subsystem to be smaller than the temperature of the leads. In this regime, I discuss the conditions required to achieve mechanical ground state cooling.

Keywords: Graphene Mechanics, Nonlinear Dynamics, Dephasing in Nanomechanical Resonators, NEM-based Mass Spectrometry and Mesoscopic Heat Engines.

Research publications

This thesis is based on the work contained in the following papers, referred to by Roman numerals in the text:

PAPER I

Continuum Elastic Modeling of Graphene Resonators
J. Atalaya, A. Isacsson and J. M. Kinaret.
Nano Lett. **2008**, *8(12)*, 4196-4200.

PAPER II

General Elasticity Theory for Graphene Membranes Based on Molecular Dynamics
K. Samadikhah, J. Atalaya, C. Huldt, A. Isacsson and J. M. Kinaret.
Mater. Res. Soc. Symp. Proc. **2008**, 1057-II10-20.

PAPER III

Narrowband Nanomechanical Mass Spectrometry using Nonlinear Response of a Graphene Membrane
J. Atalaya, J. M. Kinaret and A. Isacsson.
EPL **2010**, 91, 48001.

PAPER IV

Diffusion-Induced Dephasing in Nanomechanical Resonators
J. Atalaya, A. Isacsson and M. I. Dykman.
Phys. Rev. B **2011**, 83, 045419.

PAPER V

Diffusion-Induced Bistability of Driven Nanomechanical Resonators
J. Atalaya, A. Isacsson and M. I. Dykman.
Phys. Rev. Lett. **2011**, 106, 227202.

PAPER VI

Spintronics-based Mesoscopic Heat Engine
J. Atalaya and L. Y. Gorelik.
Phys. Rev. B **2012**, 85, 245309.

PAPER VII

Mass-loading Induced Dephasing in Nanomechanical Resonators
J. Atalaya
Submitted to Journal of Physics C.

TABLE OF CONTENTS

CHAPTER 1

Introduction

1.1 Nanomechanics

An important line of research in condensed matter is *Nanomechanics*. The latter studies the mechanical [1–3] and dynamical properties [4–6] of nanoscale massive objects, and also the interaction between the latter and much bigger systems (reservoirs or baths), containing large number of degrees of freedom [4, 7, 8]. Nanomechanics is not only important for fundamental research but it also has practical value. In fundamental research, nanomechanics provides an opportunity to investigate the crossover between the validity of the classical and quantum descriptions of nanoscale massive objects [9, 10]. For instance, graphene-based nanomechanical resonators could be used to implement nonclassical dynamical states such as a superposition of macroscopically distinct states, known as Schrödinger cat states [11]. Other research fields related to nanomechanics are *nanooptomechanics* [12] and *nanoelectromechanics* [13]. The former deals with the interaction between light and a mechanical element (e.g., a movable mirror). Nanoelectromechanics investigates the interaction between a mechanical element (e.g., a doubly clamped nanotube) and electrons, moving along the latter, in the presence of electric fields [14]. Experimentally, it has been demonstrated that nanomechanical resonators can be used as switches (e.g., carbon nanotube based field effect transistors [15–17] and nanorelays [18]) and ultrasensitive sensors of mass [19–25], charge [26] and spin [27]. This high level of sensitivity is due to the high quality factors, $Q \sim 10^5$, of vibrational modes [28–30]. The high quality factors of the eigenmodes imply that their absorption spectrum line shapes can be distorted with ease by deterministic (e.g., Duffing nonlinearity [4]) or random fluctuations of the eigenfrequency (dephasing). In this thesis I investigate the latter possibility in the context of mass sensing applications, cf. appended papers IV and VII.

The discoveries of carbon nanotubes and, more recently, graphene have had a positive impact and raised the interest in the field of Nanomechanics. The reason is that these carbon allotropes have excellent electrical and mechanical properties [31]. They also provide the raw material for fabricating low weight, mechanically stable high frequency nanoelectromechanical resonators with very low intrinsic losses [29, 30, 32, 33]. An important feature

of these nanoresonators is the tunability of the eigenfrequencies of the vibrational modes [34, 35]. My PhD research work started with the study of the mechanical properties of monolayer graphene membranes. Specifically, I developed a nonlinear elasticity theory for graphene resonators, cf. appended papers I and II. I also studied the possibility to develop a mass sensing device using the nonlinear dynamical response of square graphene resonators, cf. appended paper III.

The high sensitivity of nanomechanical resonators makes them also sensitive to random disturbances (noise) caused by the environment (other systems which weakly interact with the nanoresonator). An important part of my PhD research has been devoted to the study of dephasing of vibrational eigenmodes of nanoresonators induced by random mass loading of small particles onto the resonator surface, cf. appended papers IV, V and VII. The "good" coupling of nanoresonators with the environment (not necessarily in thermal equilibrium) makes them also ideal candidates for energy harvesting applications [36]. In paper VI, I investigate the situation where a nanotube resonator is coupled to two electrodes, held at different temperatures (no mutual equilibrium), and demonstrate that the mechanical element can exhibit different stationary regimes; namely, cooling, heating and heat engine regimes. In particular, in the heat engine regime, the nanotube develop sustained self oscillations which can be thought as the cyclic motion of, e.g., a Stirling heat engine.

1.2 Thesis overview

Chapter 2 deals with the elasticity theory for monolayer graphene membranes. The theory can be employed to model long wavelength displacements of the membrane in graphene-based resonators. The theory accounts for the built-in tension when the membrane is subject to comparatively large out-of-plane displacements (it is assumed that all or some edges of the membrane are clamped to a rigid substrate). I present molecular dynamics results to validate the theory. Experimental data also agrees with the nonlinear elasticity theory. I refer the reader to the appended papers I and II.

Chapter 3 deals with an application of the elasticity theory for monolayer graphene to design a graphene-based mass sensing device. This work was initially motivated by Mark Kac's paper: *"can one hear the shape of a drum"* [37]. Mark Kac asked the question if there exist isospectral two-dimensional domains (i.e., two domains Ω_1 and Ω_2 with the same set of eigenvalues, λ, of the Helmholtz eigenvalue problem: $\Delta u - \lambda u = 0$ with Dirichlet boundary conditions, $u = 0$ at $\partial\Omega_i$). The answer is positive if we restrict to convex domains. Gordon, Webb and Wolpert have made a construction of two simply connected nonconvex domains with the same set of eigenvalues [38]. In my case, I am not interested in the shape of the resonator but in the mass distribution. Different mass distributions gives different eigenfrequency shifts of the

vibrational modes. I find that a mass sensing scheme, employing the nonlinearity and the degeneracy of square graphene resonators, can be developed to determine both the mass and position of a single (static) analyte adsorbed on the membrane. I refer the reader to the appended paper III.

Chapter 4 deals with a problem of high quality factor resonators; namely, dephasing. Dephasing means uncertainty in the eigenmode phase due to random fluctuations of its eigenfrequency (frequency noise). These fluctuations can significantly distort the, typically Lorentzian, eigenmode absorption spectrum line. The final shape of the latter depends on the intensity and correlation time of the frequency noise. I emphasize that dephasing alone can lead to significant changes of the absorption line without extra dissipation or nonlinear damping. My research focuses on investigating dephasing due to random mass loading in nanomechanical resonators. I discuss a model which accounts for frequency noise due to diffusion, adsorption and desorption of analytes onto the resonator surface. The results presented in this chapter are relevant for mass sensing applications. I argue that it also possible to determine mass transport coefficients, such as diffusion coefficient. I refer the reader to the appended papers IV and VII.

Chapter 5 deals with diffusion induced bistability of driven nanomechanical resonators. Generally speaking, nonlinear phenomena in nanomechanical resonators can be effectively induced by a comparatively fast frequency noise process subject to backaction (i.e., the frequency noise is influenced by the motion of the resonator). In particular, I consider the situation of particles diffusing along a one-dimensional resonator, whose fundamental flexural mode is underdamped and driven near resonance. Here, the backaction is caused by an inertial force, which drives the particles towards the vibrational antinode. I find that if the particles diffuse comparatively fast (i.e., the diffusion length, within the eigenmode energy relaxation time, is much larger than the resonator length), then the eigenmode dynamics exhibits bistability between a large amplitude vibrational state, where the particles are accumulated at the antinode, and a small amplitude state, where the particles are almost uniformly distributed along the resonator. Moreover, the interstate switching events occur on a time scale much larger than the eigenmode energy relaxation time. I investigate the onset of the bistability near the bifurcation points and find that the interstate switching rate depends exponentially on the number of particles, N, and diffusion coefficient, D, with an exponent proportional to $(ND)^{-1}$. I refer the reader to the appended paper V.

Finally, in chapter 6, I study the performance of a mesoscopic heat engine using a quantum mechanical description. In particular, I consider a spintronic-based mesoscopic heat engine which consists of a carbon nanotube suspended between two spin polarized leads held at different temperatures. The system is subject to a nonuniform magnetic field, which induces an electronic two-level system (TLS) inside the nanotube and also a spin-mechanical coupling between the TLS and the fundamental flexural mode of the nanotube (me-

chanical subsystem). I find that there exist three distinct regimes of operation of the mesoscopic heat engine; namely, cooling, heating and heat engine regimes. In the cooling (heating) regime, the mechanical subsystem acquires an effective temperature which is smaller (larger) than the temperatures of the baths. In the heat engine regime, the mechanical subsystem develops sustained self oscillations [39]. This work was motivated by Linden et al.: "*How Small Can Thermal Machines Be? The Smallest Possible Refrigerator*" [40]. Linden et al. use a three-particle interaction (hard to realize experimentally) between three qubits in order to show that it is possible to cool one of the qubits (the other two qubits are in contact with reservoirs held at different temperatures) to a temperature smaller than the temperatures of the heat reservoirs. In this chapter I consider a realistic realization (the structure under consideration has been recently realized experimentally by Hueso et al. [41]) of a mesoscopic heat engine. I refer the reader to the appended paper VI.

CHAPTER 2

Elasticity theory of graphene membranes

In this chapter I briefly describe the elasticity theory for graphene membranes at zero temperature. A more detailed derivation is given in my master thesis [42] and also in the papers I and II. At finite temperature T, the shape of a free-standing graphene membrane exhibits small out-of-plane ripples which have a correlation length $l_c \lesssim 8$ nm and amplitude $h \lesssim 1$ nm at temperatures $T \lesssim 300$ K [2,43,44]. In the absence of external applied tension, ripple formation also lead to in-plain contraction of the membrane. The elasticity theory discussed below accounts for the motion of the membrane in the long wavelength limit where the graphene is modeled as a smooth surface. Here, I do not consider the small ripple corrections [1,3,45–49].

The elasticity theory for monolayer graphene is derived from an atomistic model which accounts for the energy cost, U_{sp^2}, to change the length of the sp^2 bonds and also the angle between neighboring bonds in the membrane [50–52],

$$U_{sp^2} = \sum_{i=1}^{N} \left\{ \sum_{i_k} \frac{\alpha}{8a_0^2} \left(\bar{r}_{ii_k}^2 - a_0^2\right)^2 + \sum_{i_j<i_k} \frac{\beta}{a_0^2} \left(\bar{r}_{ii_j} \cdot \bar{r}_{ii_k} + \frac{1}{2}a_0^2\right)^2 + \gamma \bar{D}_i^2 \right\} \quad (2.1)$$

In the above formula, the parameters $\alpha = 155.9\,\mathrm{J/m^2}$, $\beta = 25.5\,\mathrm{J/m^2}$ and $\gamma = 7.4\,\mathrm{J/m^2}$ are obtained by fitting the phonon spectrum that results from Eq. (2.1) to experimental data [52]. The index i labels one of the N carbon atoms of the graphene flake and the indices i_j or i_k label one of the three nearest neighbor atoms of i. Thus, $\bar{r}_{ii_k}$ is a bond vector, $a_0 = 1.421$ Å is the equilibrium bond length of graphene at zero temperature, and

$$\bar{D}_i = \bar{r}_{ii_1} + \bar{r}_{ii_2} + \bar{r}_{ii_3},$$

where i_1, i_2 and i_3 are the indices of the three nearest neighbor atoms of the ith atom.

The first two terms of Eq. (2.1) quantify the energy cost to stretch the membrane. The last term in Eq. (2.1) quantifies the energy cost to bend the membrane. In a general deformation, such as a spherical shape, both stretching and bending terms give finite contributions to the potential energy, U_{sp^2}.

The equations of motion for the membrane in the long wavelength limit are obtained in two steps. First, I derive an expression for the elastic energy, which

is a long wavelength approximation of the atomistic formula U_{sp^2} [Eq. (2.1)]. Then, I use the least action principle to obtain the Euler-Lagrange equations of motion for the membrane. I also introduce concepts of continuum mechanics such as strain and stress and discuss two regimes of deformation; namely, the stretching and the bending regimes.

In the long wavelength approximation of the equations of motion of a graphene membrane, the shape of the membrane is approximated by a smooth surface, Ω. This surface is parametrized by two parameters ξ^1 and ξ^2, which are defined in a two-dimensional parameter space Ω_ξ, cf. Fig. 2.1, by

$$\Omega : \bar{r} = \bar{r}(t, \xi^1, \xi^2),$$

where t is the time parameter. Here, $\bar{r}(t, \xi^1, \xi^2)$ represents the position of the graphene surface in the three-dimensional physical space. Similarly, I use the same parameters ξ^1 and ξ^2 to parametrize the undeformed graphene surface Ω_0 in physical space, cf. Fig. 2.1,

$$\Omega_0 : \bar{r}_0 = \bar{r}_0(\xi^1, \xi^2).$$

At a given instant of time, the relative displacement between two points $\bar{r}$ and $\bar{r} + \Delta\bar{r}$ on the deformed graphene surface Ω is approximately given by

$$\Delta\bar{r} \approx \bar{g}_k \Delta\xi^k + \frac{1}{2}\Gamma^m_{kl}\Delta\xi^k\Delta\xi^l\bar{g}_m + \frac{1}{2}L_{kl}\Delta\xi^k\Delta\xi^l\bar{n}, \tag{2.2}$$

and the corresponding points in parameter space are $\bar{\xi}$ and $\bar{\xi}+\Delta\bar{\xi}$, respectively. I use the convention of summation over repeated indices. The tangent vectors $\bar{g}_k = \partial\bar{r}(\bar{\xi}, t)/\partial\xi^k$, $k = \{1, 2\}$, span the tangent space T at the point $\bar{r}$, cf. Fig. 2.1. The unit normal vector to the surface at $\bar{r}$ is $\bar{n} = \bar{g}_1 \times \bar{g}_1/\|\bar{g}_1 \times \bar{g}_2\|$. The coefficients Γ^m_{kl} are known as the Christoffel symbols and the coefficients L_{kl} are the components of the curvature tensor $\hat{L} = L_{kl}\bar{g}^k\bar{g}^l$ where $L_{kl} = \bar{n} \cdot \partial\bar{g}_k/\partial\xi^l = -\partial\bar{n}/\partial\xi^l \cdot \bar{g}_k$. Also, $\bar{g}_k = g_{kl}\bar{g}^l$ and $\bar{g}^k = g^{kl}\bar{g}_l$ where $g_{kl} = \bar{g}_k \cdot \bar{g}_l$ are the components of the metric tensor and g^{kl} are the inverse metric tensor components defined by $g^{kl}g_{lm} = \delta^k_m$ and δ^k_m is the Kronecker delta. The coefficients Γ^m_{kl} and L_{kl} are related by the following relation

$$\frac{\partial\bar{g}_k}{\partial\xi^l} = \Gamma^m_{kl}\bar{g}_m + L_{kl}\bar{n}. \tag{2.3}$$

In Eq. (2.2), the first two terms belong to the two-dimensional tangent space T. For $\|\bar{\xi}\| \ll 1$, I may neglect the second order terms in ξ^k and keep only the first order contribution: $\bar{g}_k\Delta\xi^k$. Note that the second order terms along the normal direction can not be neglected because there are no first order terms along this direction. Thus, I obtain

$$\Delta\bar{r} \approx \bar{g}_k \Delta\xi^k + \frac{1}{2}L_{kl}\Delta\xi^k\Delta\xi^l\bar{n}, \tag{2.4}$$

and similarly for the undeformed surface Ω_0,

$$\Delta\bar{r}_0 \approx \bar{g}_{0k}\Delta\xi^k + \frac{1}{2}L_{0kl}\Delta\xi^k\Delta\xi^l\bar{n}. \tag{2.5}$$

I use the latter two equations for two carbon atoms forming a covalent bond, i.e. $\Delta\bar{r} = \bar{r}_{ij}$ and $\Delta\bar{r}_0 = \bar{r}_{0ij}$ where $\bar{r}_{ij}$ and $\bar{r}_{0ij}$ are the same covalent bond in the deformed and the undeformed graphene membranes, respectively. From Eq. (2.5), it follows

$$\Delta\xi^k \approx \bar{r}_{0ij}\cdot\bar{g}_0^k, \tag{2.6}$$

and substitution of the above relation in Eq. (2.4) leads to (no summation over i, j)

$$\begin{aligned}
\bar{r}_{ij} &\approx \bar{r}_{0ij}\cdot\bar{g}_0^k\bar{g}_k + \frac{1}{2}\big(\bar{r}_{0ij}\cdot L_{kl}\bar{g}_0^k\bar{g}_0^l\cdot\bar{r}_{0ij}\big)\bar{n} \\
&= \bar{r}_{0ij}\cdot\bar{\nabla}_0\bar{r} + \frac{1}{2}\big(\bar{r}_{0ij}\cdot\bar{g}_0^r\bar{g}_r\cdot L_{kl}\bar{g}^k\bar{g}^l\cdot\bar{g}_s\bar{g}_0^s\cdot\bar{r}_{0ij}\big)\bar{n} \\
&= \bar{r}_{0ij}\cdot\bar{\nabla}_0\bar{r} + \frac{1}{2}\big(\bar{r}_{0ij}\cdot\check{L}\cdot\bar{r}_{0ij}\big)\bar{n}.
\end{aligned} \tag{2.7}$$

Above, $\bar{\nabla}_0\bar{r} = \bar{g}_0^k\partial\bar{r}/\partial\xi^k = \bar{g}_0^k\bar{g}_k$ is the gradient of the map $\bar{r}(t,\bar{r}_0)$. In the above equation, $\check{L}$ is the curvature tensor projected onto the tangent plane T_0 of the undeformed graphene surface Ω_0,

$$\check{L} = \bar{\nabla}_0\bar{r}\cdot\hat{L}\cdot\bar{\nabla}_0\bar{r}^\dagger. \tag{2.8}$$

The elastic energy density $W_0(\bar{r}_0)$ is obtained by inserting the approximation (2.7) for the deformed bond vector $\bar{r}_{ij}$ in the atomistic formula for the potential energy U_{sp^2}, cf. Eq. (2.1). The sum over the carbon atoms i in Eq. (2.1) is approximated by an integral,

$$U_{sp^2} \approx \iint_{\Omega_0} d\Omega_0\; W_0(\bar{r}_0),$$

where $W_0(\bar{r}_0)$ is given by

$$W_0(\bar{r}_0) = \frac{4\sqrt{3}}{9}\left\{\sum_j \frac{\alpha}{8}\left(\frac{\bar{r}_{ij}}{a_0}\cdot\frac{\bar{r}_{ij}}{a_0} - 1\right)^2 + \sum_{j<k}\beta\left(\frac{\bar{r}_{ij}}{a_0}\cdot\frac{\bar{r}_{ik}}{a_0} + \frac{1}{2}\right)^2 + \gamma\frac{\bar{D}_i}{a_0}\cdot\frac{\bar{D}_i}{a_0}\right\}, \tag{2.9}$$

and

$$\begin{aligned}
\bar{r}_{ij}\cdot\bar{r}_{ij} &= \bar{r}_{0ij}\cdot\hat{g}\cdot\bar{r}_{0ij} + \frac{1}{4}[\bar{r}_{0ij}\cdot\check{L}\cdot\bar{r}_{0ij}]^2, \\
\bar{r}_{ij}\cdot\bar{r}_{ik} &= \bar{r}_{0ij}\cdot\hat{g}\cdot\bar{r}_{0ik} + \frac{1}{4}(\bar{r}_{0ij}\cdot\check{L}\cdot\bar{r}_{0ij})(\bar{r}_{0ik}\cdot\check{L}\cdot\bar{r}_{0ik}), \\
\bar{D}_i\cdot\bar{D}_i &= \frac{1}{4}[\bar{r}_{0ij_1}\cdot\check{L}\cdot\bar{r}_{0ij_1} + \bar{r}_{0ij_2}\cdot\check{L}\cdot\bar{r}_{0ij_2} + \bar{r}_{0ij_3}\cdot\check{L}\cdot\bar{r}_{0ij_3}]^2.
\end{aligned} \tag{2.10}$$

In the above formula, $\hat{g} = \bar{\nabla}_0 \bar{r} \cdot \bar{\nabla}_0 \bar{r}^\dagger = g_{kl} \bar{g}_0^k \bar{g}_0^l$ is the deformation tensor in the basis $\bar{g}_0^k$. Assuming that the undeformed graphene surface Ω_0 is on the $z = 0$ plane, the undeformed bond vectors $\bar{r}_{0ij}$ of the atom depicted as black dots in Fig. 2.1 are

$$\bar{r}_{0ij} = \{a_0 \bar{e}_x, -\frac{a_0}{2}\bar{e}_x + \frac{\sqrt{3}a_0}{2}\bar{e}_y, -\frac{a_0}{2}\bar{e}_x - \frac{\sqrt{3}a_0}{2}\bar{e}_y\}, \tag{2.11}$$

and the corresponding bond vectors for the atoms depicted as red dots in Fig. 2.1 are the opposite of the above bond vectors. Below, I will assume that the displacement of both type of atoms are described by the same displacement field

$$\bar{u} \equiv \bar{r}(t, \bar{\xi}) - \bar{r}_0(\bar{\xi}).$$

Then, the contributions of both type of atoms to the elastic energy are equal. This assumption is reasonable if we are interested in modes whose wavelength is much larger than the typical distance ($\sim a_0$) between the two atoms of the unit cell of monolayer graphene.

For a general deformation, the elastic energy density $W_0(\bar{r}_0)$ [Eq. (2.9)] depends on the deformation tensor, $\hat{g}$, and the curvature tensor, $\hat{L}$. Now, I will consider two regimes of the graphene mechanics; namely, the stretching and bending regimes where the main contribution to the elastic energy comes from the deformation tensor $\hat{g}$ and the curvature tensor $\hat{L}$, respectively.

2.1 Stretching regime

In the stretching regime the main contribution to the elastic energy density $W_0(\bar{r}_0)$ comes from the local in-plane deformation of the bond configuration. The elastic energy is then approximated by the formula (2.9) where only the $\hat{g}$-dependent terms are kept. Below, I use Cartesian coordinates $\xi^1 = x$, $\xi^2 = y$ and assume that the undeformed membrane is on the $z = 0$ plane. The displacement field is

$$\bar{u} = \big(u(x,y), v(x,y), w(x,y)\big),$$

where u and v represent in-plane displacements, parallel to the $z = 0$ plane, and w represents the out-of-plane displacement, perpendicular to the $z = 0$ plane. The stretching energy W_0^S is then given by [53]

$$W_0^S = \frac{Eh}{2(1-\nu^2)}\big[E_{xx}^2 + E_{yy}^2 + 2\nu E_{xx}E_{yy} + 2(1-\nu)E_{xy}^2\big], \tag{2.12}$$

where E_{xx}, E_{xy} and E_{yy} are the components of the Cauchy strain tensor $\hat{E}$

$$\begin{aligned} E_{xx} &= u_x + \big(u_x^2 + v_x^2 + w_x^2\big)/2, \\ E_{xy} &= \big(u_y + v_x + u_x u_y + v_x v_y + w_x w_y\big)/2, \\ E_{yy} &= v_y + \big(u_y^2 + v_y^2 + w_y^2\big)/2. \end{aligned} \tag{2.13}$$

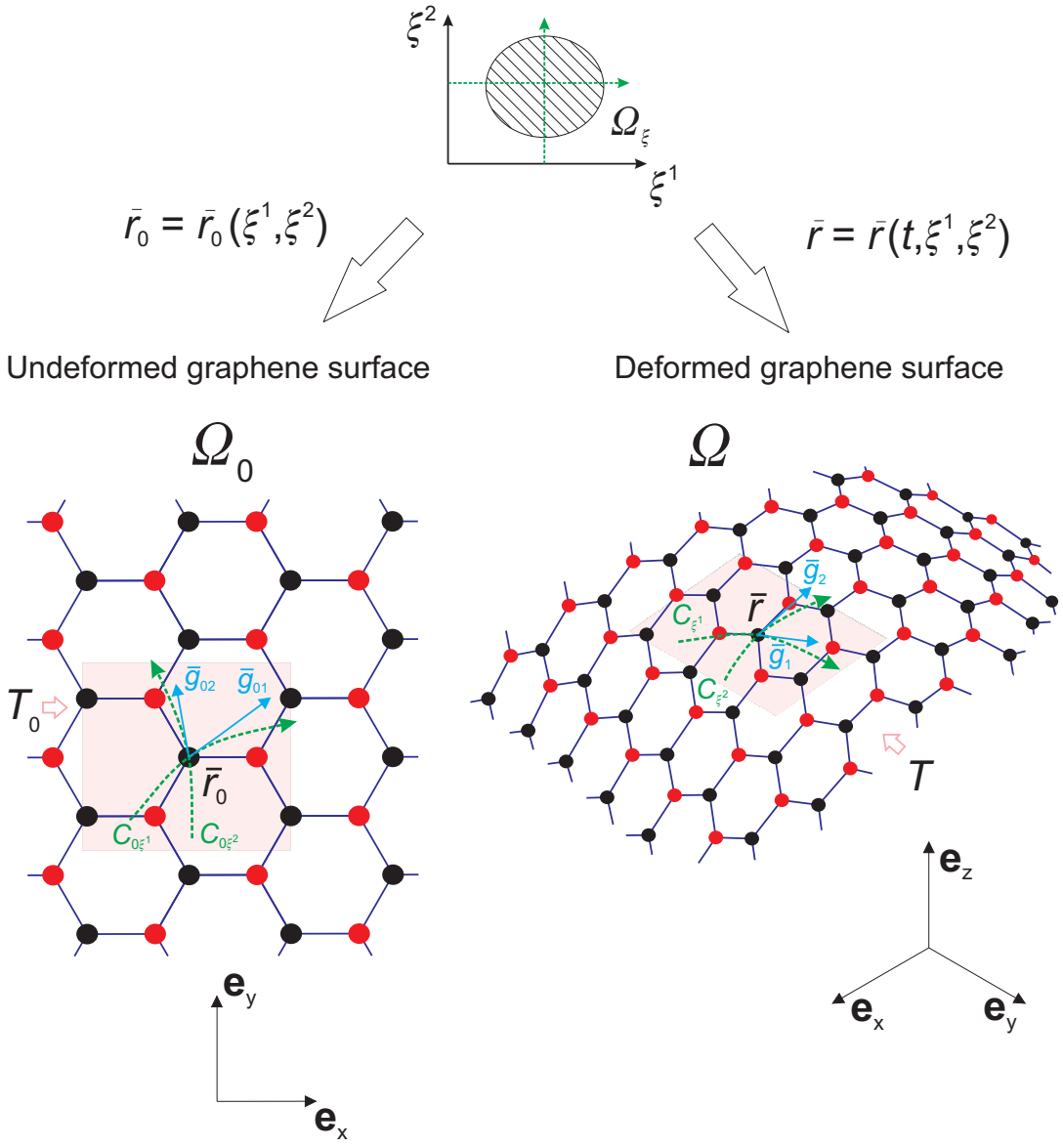

Figure 2.1: The flat surface Ω_0 and the smooth surface Ω depict an undeformed and deformed graphene membrane, respectively. The surface Ω is defined by a time-dependent mapping $\Omega : \bar{r} = \bar{r}(t, \xi^1, \xi^2)$ from a two-dimensional domain Ω_ξ (top) to the three-dimensional physical space spanned by the unit vectors $\mathbf{e}_x$, $\mathbf{e}_y$ and $\mathbf{e}_z$. Here, t is the time parameter. The figure also depicts the tangent plane T to Ω at the point $\bar{r}$. The curves C_{ξ^k}, $k = \{1, 2\}$, are the images of the straight lines depicted in Ω_ξ. The tangent vector to C_{ξ^k} is $\bar{g}_k = \partial\bar{r}/\partial\xi^k$. Similar definitions also hold for Ω_0.

In the above equations, the subscripts on u, v, w denote differentiation, i.e. $u_x = \partial u/\partial x$ etc. and the coefficient Eh is, in the theory of thin plates, the Young modulus multiplied by the thickness of the plate [53, 54]. I point out that, in the present elasticity theory for graphene, Eh is a single parameter. It is not necessary to assume a thickness for graphene. The Poisson ratio is ν. Both parameters Eh and ν are related to the Lamé parameters λ and μ as $Eh = 4\mu(\lambda+\mu)/(\lambda+2\mu), \nu = \lambda/(\lambda+2\mu)$. The Lamé parameters are in turn determined by the parameters of the atomistic formula for the potential energy U_{sp^2}: $\mu = 4\sqrt{3}(\alpha/8+\beta)/3$ and $\lambda = 4\sqrt{3}(\alpha/8-\beta/2)/3$.

The elastic energy density W_0^S can also be written in the invariant form (basis independent)

$$W_0^S = \frac{\lambda+2\mu}{2} I_1^2(\hat{E}) - 2\mu I_2(\hat{E}). \tag{2.14}$$

Above, I_1 and I_2 are the two principal invariants of the strain tensor $\hat{E}$ defined as

$$\begin{aligned} \hat{E} &= \frac{1}{2}(\hat{g}-\hat{I}), \\ &= \hat{\epsilon}_0(\bar{u}) + \frac{1}{2}\bar{\nabla}_0\bar{u}\cdot\big(\bar{\nabla}_0\bar{u}\big)^\dagger, \end{aligned} \tag{2.15}$$

and

$$\hat{\epsilon}_0(\bar{u}) = \frac{1}{2}\big(\bar{\nabla}_0\bar{u} + (\bar{\nabla}_0\bar{u})^\dagger\big),$$

is the infinitesimal strain tensor. The identity tensor is $\hat{I} = \bar{g}_k\bar{g}^k$. The first principal invariant $I_1(\hat{E})$ corresponds to the trace of $\hat{E}$ and the second invariant is $I_2 = \big[I_1^2(\hat{E}) - I_1(\hat{E}^2)\big]/2$. The form (2.14) for the elastic energy also shows that graphene is an isotropic elastic material.

The strain tensor $\hat{E}$ is a nonlinear function of the derivatives of the displacement field $\bar{u}$. The general expression for the stretching energy (2.14) can be simplified in the case that the out-of-plane displacement is dominant. This is typically the case in graphene-based resonators where the driven modes are the out-of-plane vibrational modes. Neglecting the second order terms u_x^2, v_y^2, u_xu_y and v_xv_y in the expression for the strain components, i.e. $E_{xx} \approx u_x + w_x^2/2$, $E_{yy} \approx v_y + w_y^2/2$ and $E_{xy} \approx (u_y+v_x)/2 + w_xw_y/2$, results in the following expression for the elastic energy of the membrane

$$\begin{aligned} W_0^{\mathrm{vK}} &= \frac{\lambda+2\mu}{2}\Big(u_x^2 + v_y^2 + u_xw_x^2 + v_yw_y^2 + \big(w_x^2+w_y^2\big)^2/4\Big) \\ &\quad +\lambda\big(u_xv_y + u_xw_y^2/2 + v_yw_x^2/2\big) + \frac{\mu}{2}\Big(\big(u_y+v_x\big)^2 + 2u_yw_xw_y + 2v_xw_xw_y\Big). \end{aligned} \tag{2.16}$$

The above formula coincides with the von Karman's expression for the elastic energy of a thin plate [53].

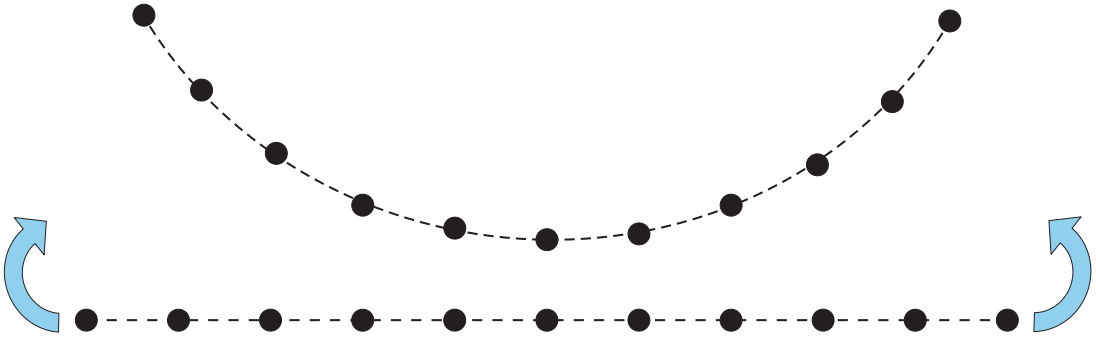

Figure 2.2: Folding a graphene membrane without applying tension (stretching).

If the membrane is subject to an initial strain (such that $u_x = \delta_x$, $v_y = \delta_y$ and $u_y = v_x = 0$ with $\delta_{x,y} \ll 1$) at zero vertical deflection ($w = 0$) and the out-of-plane displacement is small such that the induced in-plane displacement gradients are smaller than $\delta_{x,y}$, then we have the following expression for the elastic energy

$$W_0^S = \frac{\lambda + 2\mu}{2}\Big(\delta_x^2 + \delta_y^2 + \delta_x w_x^2 + \delta_y w_y^2 + \big(w_x^2 + w_y^2\big)^2/4\Big) + \lambda\big(\delta_x\delta_y + \delta_x w_y^2/2 + \delta_y w_x^2/2\big). \tag{2.17}$$

Above, it has been assumed that $u_x \approx \delta_x$ and $v_y \approx \delta_y$, $u_y \approx 0$ and $v_x \approx 0$. The initial strain, considered in Eq. (2.17), may be the result of the manufacturing processes of graphene resonators. I refer to Eq. (2.17) as the out-of-plane approximation since it only involves the out-of-plane displacement field $w(x, y)$.

2.2 Bending regime

This regime refers to a process of folding a graphene membrane without applying any tension. For instance, Fig. 2.2 shows the folding of a graphene membrane into a cylinder-like shape (deformation into a sphere-like shape requires both stretching and bending energy cost). The energy cost due to bending can be estimated as $\iint d\Omega_0\, W_0^B$, where the bending energy density is given by [1]

$$W_0^B \approx \frac{\kappa}{2}(2a_0 H)^2, \tag{2.18}$$

and $\kappa = \sqrt{3}a_0^2\gamma/2$ is the bending rigidity. $H = I_1(\hat{L})/2$ is the local mean curvature and $I_1(\hat{L})$ is the first principal invariant of the curvature tensor $\hat{L}$. Using $\gamma = 7.4\ \mathrm{J/m^2}$ [52], the bending rigidity for monolayer graphene is approximately $\kappa \approx 0.8$ eV.

In typical graphene resonators, graphene is clamped to a rigid substrate and we are mainly interested in the out-of-plane displacement. It turns out that in this case the stretching energy accounts for most of the elastic energy. Figure 2.3 shows that for a given out-of-plane deformation the stretching energy is almost equal to what we would obtain using the atomistic formula U_{sp^2}

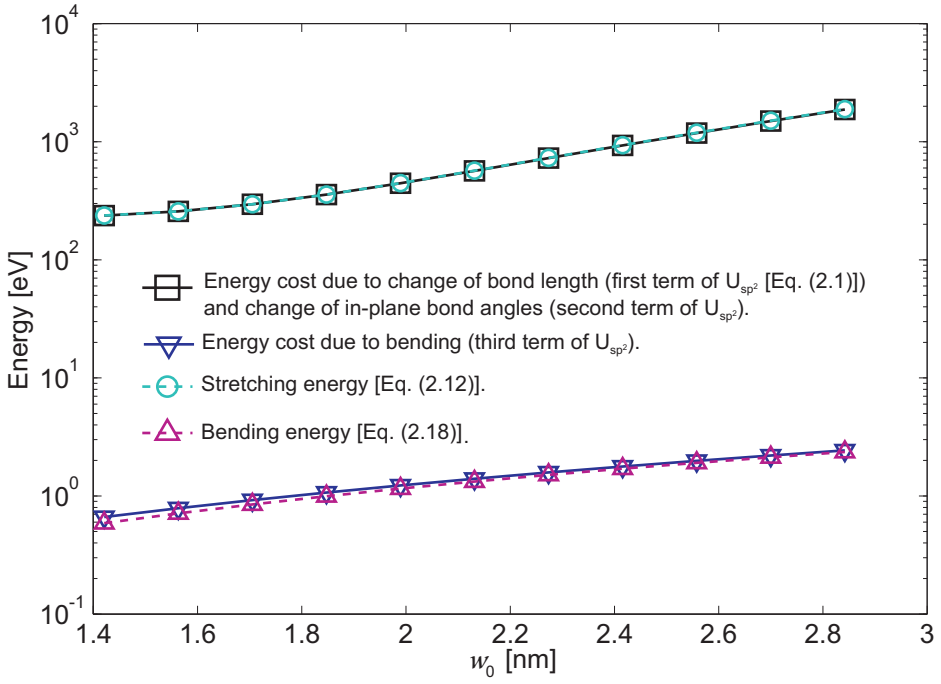

Figure 2.3: Stretching and bending energies as functions of deflection for a square clamped graphene flake of side $2a \approx 6$ nm. The energy calculations correspond to displacements given by $u = u_0 \sin(\pi x/a)\cos(\pi y/2a)$, $v = v_0 \cos(\pi x/2a)\sin(\pi y/a)$ and $w = w_0 \cos(\pi x/2a)\cos(\pi y/2a)$ where $u_0 = v_0 = a_0$, $w_0 \in [10a_0, 20a_0]$ and $a_0 = 1.421$ Å is the graphene lattice constant. The figure shows that the stretching energy [Eq. (2.12)] accounts for most of the energy cost to deform a clamped graphene membrane. Here, the stretching energy is at least two orders of magnitude greater than the bending energy calculated using Eq. (2.18).

[Eq. (2.1)] and the stretching energy is at least two orders of magnitude larger than the bending energy computed using Eq. (2.18).

2.3 Equations of motion in the stretching regime

The classical equations of motion for the graphene surface $\Omega(t)$ are obtained from the least action principle. The classical action $S[\bar{r}]$ is

$$S[\bar{r}, t] = \int_0^t dt \iint_{\Omega_0} d\Omega_0 \, L(\bar{r}, \dot{\bar{r}}),$$

where $L(\bar{r}, \dot{\bar{r}}) = \rho_0 (\partial_t \bar{r})^2/2 - W_0^S(\bar{r})$ is the Lagrangian density and ρ_0 is the graphene mass density. The classical trajectory $\bar{r}^{cl}$ satisfies the equation

$$\frac{\delta S}{\delta \bar{r}}[\bar{r}^{cl}] = 0.$$

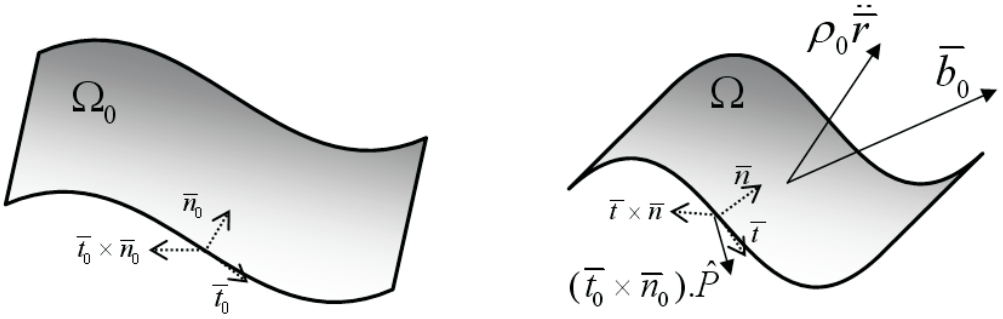

Figure 2.4: Interpretation of the Piola stress tensor $\hat{P}$. The latter gives the forces on the boundary $\partial\Omega$ of Ω per unit of length of the boundary $\partial\Omega_0$. That is, the differential of force on $\partial\Omega$ is equal to $ds_0(\bar{t}_0 \times \bar{n}_0) \cdot \hat{P}$, where $ds_0, \bar{t}_0$ and $\bar{n}_0$ are the length element, tangent and normal unit vectors at $\partial\Omega_0$. External body forces $\bar{b}_0$ are also depicted.

In order to identify the stress tensor in the theory, it is useful to write the equation of motion in its integral form [42]

$$\iint_{\Omega_0} d\Omega_0 \, \rho_0 \ddot{\bar{r}} = \oint_{\partial\Omega_0} ds_0 \, (\bar{t}_0 \times \bar{n}_0) \cdot \hat{P}. \tag{2.19}$$

Above, $\bar{t}_0$ is the unit vector tangent to the boundary $\partial\Omega_0$, $\bar{n}_0$ is the unit vector normal to the surface Ω_0, ds_0 is the differential of length in the boundary $\partial\Omega_0$, cf. Fig. 2.4. In Eq. (2.19), I identity $\hat{P}$ as a measure of the stress built in the membrane because the inertial force $\iint d\Omega_0 \, \rho_0 \ddot{\bar{r}}$ is balanced by the force applied only on the boundary: $\oint ds_0 (\bar{t}_0 \times \bar{n}_0) \cdot \hat{P}$. In the literature, $\hat{P}$ is known as the Piola stress tensor and, for graphene, it is measured in units of N/m.

The differential form of the equations of motion, in Cartesian coordinates, is

$$\ddot{\bar{u}}(x,y) + c\dot{\bar{u}}(x,y) = \rho_0^{-1} \mathcal{D}\hat{P}[\bar{u}(x,y)] + {m_c}^{-1} \bar{F}_0(x,y,t), \tag{2.20}$$

where I have also included a (phenomenological) viscous dissipative term, $c\dot{\bar{u}}$, with a damping rate coefficient c, $\bar{F}_0$ is an external force distribution, m_c is the carbon mass and the linear differential operator $\mathcal{D}$ acts on $\hat{P}$ as

$$\mathcal{D}\hat{P} = \sum_{\chi=x,y,z} \hat{\chi}(\partial_x P_{x\chi} + \partial_y P_{y\chi}).$$

The components of the Piola stress tensor in Cartesian coordinates are

$$\begin{aligned}
P_{xx} &= (1+u_x)[(\lambda+2\mu)E_{xx}+\lambda E_{yy}]+2\mu u_y E_{xy},\\
P_{xy} &= 2\mu(1+v_y)E_{xy}+v_x[(\lambda+2\mu)E_{xx}+\lambda E_{yy}],\\
P_{xz} &= \lambda w_x(E_{xx}+E_{yy})+2\mu w_x E_{xx}+2\mu w_y E_{xy},\\
P_{yx} &= 2\mu(1+u_x)E_{xy}+u_y[(\lambda+2\mu)E_{yy}+\lambda E_{xx}],\\
P_{yy} &= (1+v_y)[(\lambda+2\mu)E_{yy}+\lambda E_{xx}]+2\mu v_x E_{xy},\\
P_{yz} &= \lambda w_y(E_{xx}+E_{yy})+2\mu w_y E_{yy}+2\mu w_x E_{xy}. \qquad (2.21)
\end{aligned}$$

Equations (2.20) and (2.21) are the equations of the elasticity theory for graphene membranes subject to finite strain [cf. Eq. (2.13)] in the stretching regime. These equations may be simplified by assuming that $u_x, u_y, v_x, v_y \ll 1$ and I obtain

$$\begin{aligned}
P_{xx} &\approx (\lambda+2\mu)E_{xx}+\lambda E_{yy},\\
P_{xy} &\approx 2\mu E_{xy},\\
P_{xz} &\approx \lambda w_x(E_{xx}+E_{yy})+2\mu(w_x E_{xx}+w_y E_{xy}),\\
P_{yx} &\approx 2\mu E_{xy},\\
P_{yy} &\approx \lambda E_{xx}+(\lambda+2\mu)E_{yy},\\
P_{yz} &\approx \lambda w_y(E_{xx}+E_{yy})+2\mu(w_y E_{yy}+w_x E_{xy}), \qquad (2.22)
\end{aligned}$$

where the strain components are given by Eq. (2.13) without the quadratic terms in the in-plane displacements: $u_x^2, u_x u_y$, etc. The equations of motion for the membrane that results from Eq. (2.22) are known as the von Karman equations of thin plate theory [53, 54].

In the out-of-plane approximation [cf. Eq. (2.17)], the equation of motion for $w(x,y,t)$ is

$$\ddot{w}(x,y,t)+c\dot{w}(x,y,t)-\sum_{\chi=x,y}\frac{\partial_\chi(w_\chi T_\chi)}{\rho_0}=\frac{F_{0z}}{m_c}, \qquad (2.23)$$

where

$$\begin{aligned}
T_x &= (\lambda+2\mu)\delta_x+\lambda\delta_y+(\lambda/2+\mu)(w_x^2+w_y^2),\\
T_y &= (\lambda+2\mu)\delta_y+\lambda\delta_x+(\lambda/2+\mu)(w_x^2+w_y^2). \qquad (2.24)
\end{aligned}$$

Above, I have introduced again the parameters δ_x and δ_y representing initial strains in the x and y directions, respectively. Note that T_x and T_y depend nonlinearly on the displacement field $w(x,y)$.

If one mode is expected to dominate the out-of-plane deformations, the out-of-plane approximation [Eq. (2.23)] may be projected onto the dominant mode to obtain an ordinary rather than a partial differential equation. For

instance, if the dominant mode in a square graphene resonator of side $2a$ is the fundamental mode,

$$w(x,y,t) = w(t)\cos\left(\frac{\pi x}{2a}\right)\cos\left(\frac{\pi y}{2a}\right),$$

then the equation of motion for the vibrational amplitude $w(t)$ is the Duffing equation [55]

$$\ddot{w}(t) + c\dot{w}(t) + \omega_0^2 w(t) + \frac{5\pi^4(\lambda+2\mu)}{128a^4\rho_0}w^3(t) = \frac{F(t)}{m_c}. \tag{2.25}$$

The driving force is

$$F(t) = \frac{1}{a^2}\iint dxdy\, F(x,y,t)\cos\left(\frac{\pi x}{2a}\right)\cos\left(\frac{\pi y}{2a}\right),$$

and the vibrational resonant frequency ω_0 of the driven mode is

$$\omega_0 = \frac{\pi}{a}\sqrt{\frac{(\lambda+\mu)(\delta+\delta^2/2)}{\rho_0}}.$$

Above, I have assumed that $\delta_x = \delta_y = \delta$. It is not necessary to project the membrane dynamics onto one mode. Interaction between different vibrational modes in the membrane may be also studied within the out-of-plane approximation. In this case, a system of coupled Duffing equations is obtained, cf. Eq. (3.6).

2.4 Comparison of the elasticity theory with molecular dynamics and experiments

Validation of the elasticity theory is performed by comparison with molecular dynamics calculations and with experimental data of graphene resonators. In the validation of the theory with molecular dynamics, I consider a rectangular fully clamped graphene flake with dimensions of 6.6 nm by 7.6 nm and subject to a uniform constant external force of 1 nN per atom applied along the z axis (graphene is initially on the $z = 0$ plane). I solve numerically the equations of motion of molecular dynamics (MD) [56] and of the continuum elasticity theory (CET) and calculate the out-of-plane displacement $w(x,y)$. The relative difference in $w(x,y)$ obtained from MD and CET is evaluated by

$$r(x,y) = 100\cdot\left|\big(w_{\text{MD}}(x,y) - w_{\text{CET}}(x,y)\big)/w_{\text{MD}}(x,y)\right|\%.$$

Figure 2.5 shows the comparison between MD and the general elasticity theory [Eqs. (2.20)-(2.21)]. It is also compared MD and the approximations of the

general elasticity theory: von Karman's theory [Eqs. (2.20), (2.22)], the out-of-plane approximation [Eq. (2.23)] and the fundamental mode approximation [Eq. (2.25)]. The figure shows that the general elasticity theory is in excellent agreement with molecular dynamics with a relative difference $r \lesssim 2\%$. The von Karman's theory shows good agreement at the central region of the graphene flake, where the out-of-plane displacement $w(x, y)$ is much larger than the in-plane displacements $u(x, y), v(x, y)$. Close to the clamping regions, the difference can be $r \gtrsim 20\%$ because the dismissed terms related to the in-plane displacements, u and v, become important. The out-of-plane approximation also shows good agreement with the molecular dynamics at the central region. In the case of study, the fundamental mode approximation is a bit worse than the out-of-plane approximation because the uniform applied force distribution also excites other modes.

Experimental data on doubly and fully clamped graphene resonators is used to test the elasticity theory. Comparisons with experimental data of J. S. Bunch et al. [57], C. Lee et al., and C. Chen et al. [58,59] show that the elasticity theory is able to predict the equilibrium shapes for a given applied pressure. Furthermore, the dynamical features of the Duffing equation [Eq. 2.24] have also been observed in these experiments [57,58]. Agreement with such experiments is achieved for values of Poisson ratio and effective Young modulus (Eh) equal to 0.18 and 300 N/m, respectively. The above mechanical description for single layer graphene membranes may also be used to study few layer graphene membranes [57] by appropriately changing the Young modulus and Poisson ratio parameters.

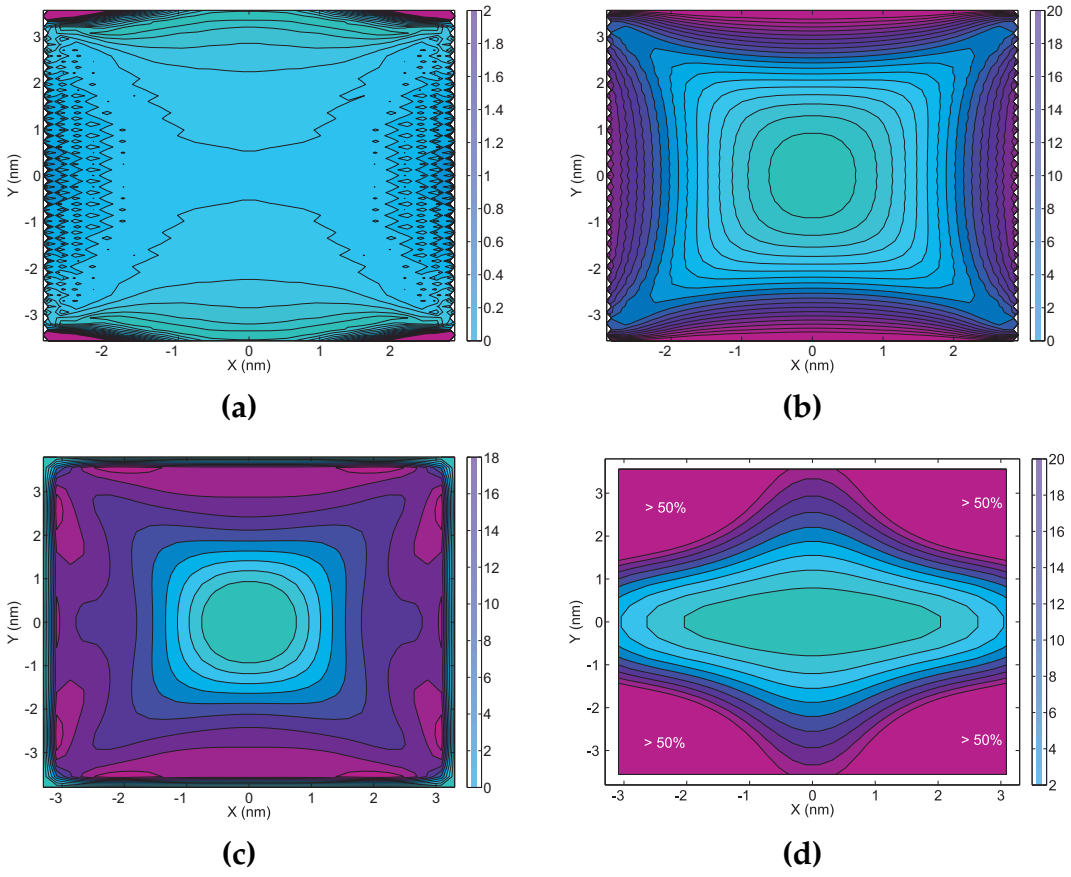

Figure 2.5: (a): Comparison between molecular dynamics (MD) and general elasticity theory [Eqs. (2.20)-(2.21)]. **(b):** Comparison between MD and von Karman's theory [Eqs. (2.20), (2.22)]. **(c):** Comparison between MD and the out-of-plane approximation [Eq. (2.23)]. **(d):** Comparison between MD and fundamental mode approximation [Eq. (2.25)]. Color bars indicate the relative difference $r(x, y)$ (%) between continuum elasticity theory and MD, see text.

CHAPTER 3

Narrow-band mass measurement scheme using nonlinear dynamics of graphene resonators

It has been demonstrated that nanoelectromechanical (NEM) devices are very suitable for sensor technology. In particular, it has been shown that NEM resonators can be employed to measure mass [20–25, 60] and charge [14, 26, 61] with very high precision. In the case of mass measurement applications, NEM resonators are useful because of the combination of properties such as low mass density, high vibrational frequencies and low intrinsic losses. These features are present, e.g., in carbon nanotube based nanoresonators where vibrational frequencies of $f_0 \gtrsim 4$ GHz and quality factors of $Q \sim 10^5$ have been recently achieved [29, 30, 33, 62]. NEM resonators are also interesting because they can be driven into the nonlinear dynamical regime [5,63–65]. In this chapter I demonstrate how to exploit nonlinear dynamical properties of graphene resonators to develop a scheme that determines not only the mass but also the position of an adsorbed particle on the membrane. Realization of this scheme may open the possibility for on-chip mass spectrometry [20, 23, 32, 66].

3.1 NEM-based mass measurement

Mass measurement using NEM resonators is based on the measurement of the resonance frequency shift, $\Delta\omega < 0$, of certain vibrational mode(s) of the resonator. For particles with mass, m, much smaller than the effective mass, M_0, of the vibrational mode, the frequency shift is proportional to the particle mass

$$-\frac{\Delta\omega}{\omega_0} \approx \mathcal{R}(\bar{X}_p)\frac{m}{M_0}, \tag{3.1}$$

where ω_0 is the bare resonance frequency of the vibrational mode and the coefficient $\mathcal{R}(\bar{X}_p)$ depends on the position, $\bar{X}_p$, of the particle on the resonator and also on the spatial profile $\phi(x)$ of the vibrational mode. The mass responsivity coefficient $\mathcal{R}(\bar{x})$ is equal to

$$\mathcal{R}(\bar{X}) = \frac{1}{2}\phi^2(\bar{X}),$$

and the vibrational mode effective mass is $M_0 = \int d^2\bar{X}\,\rho_0\phi^2(\bar{X})$ where ρ_0 is the bare mass density of the resonator.

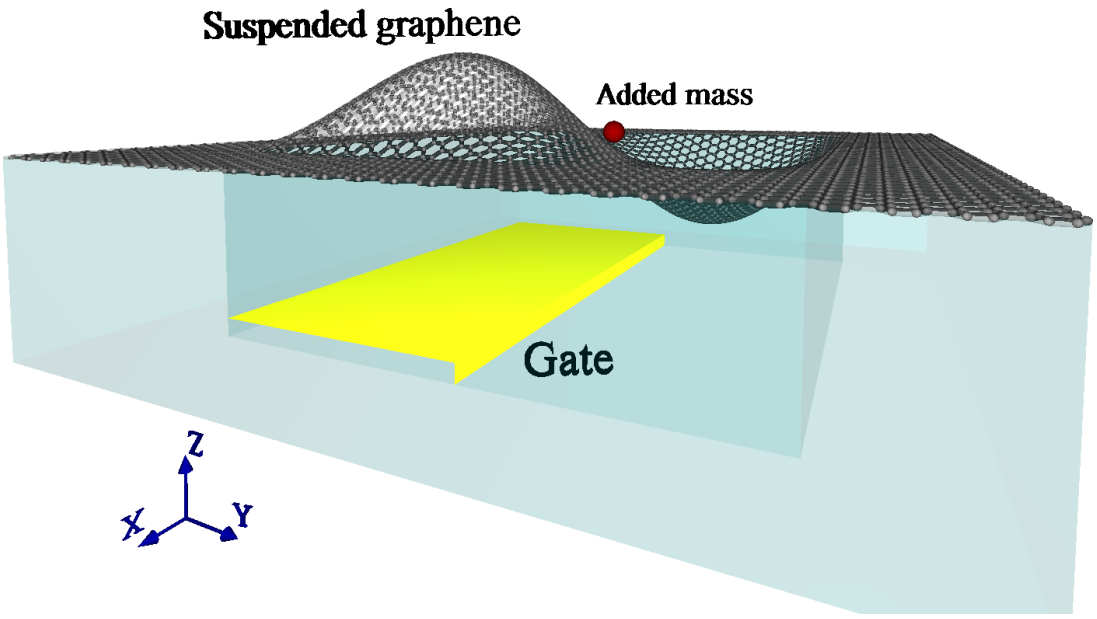

Figure 3.1: A square graphene resonator working as a mass measurement device. Mechanical vibrations are driven by a gate electrode which is symmetric along the x axis and asymmetric along the y axis. One of the first two degenerate vibrational modes is also depicted.

Figure 3.1 depicts a square graphene resonator working as a mass measurement device. The resonator is actuated by a gate electrode. It is also depicted one of the first two degenerate vibrational modes. Below, I will discuss a mass measurement scheme for this type of resonator. The aim is to determine the mass and the position of a single adsorbed particle on the membrane.

3.2 Single particle mass measurement scheme

Equation (3.1) has so far been the fundamental equation for mass measurement using NEM resonators [25]. It is easy to see that in order to uniquely determine the mass, m, of the adsorbed particle from the frequency shift $\Delta\omega$ it is necessary to know in advance the position of the particle, $\bar{X}_p$. In the case of two dimensional resonators the position of the particle introduces two new unknowns: $\bar{X}_p = (X_p, Y_p)$. The three unknowns m, X_p and Y_p may be determined from the frequency shifts of three different vibrational modes. Thus, a scheme probing only the linear response of the system requires three detectors tuned to three different vibrational modes. Below, I demonstrate that by exploiting the intrinsic nonlinearity of graphene resonators, it is possible to develop a scheme where only one detector (e.g., tuned to the fundamental mode) is required to determine the position and mass of the adsorbed particle.

3.2.1 The model

The mechanics of graphene is described within the out-of-plane approximation, cf. Eq. (2.23),

$$\rho\ddot{w} + \rho_0 c\dot{w} - \sum_{\xi=X,Y} \partial_\xi(T_\xi \partial_\xi w) = P_z(X,Y,t), \tag{3.2}$$

where $w(X,Y,t)$ is the membrane out-of-plane displacement, $P_z(X,Y,t)$ is the applied force per unit of area, ρ is the mass density of the system, the dissipative term $\rho_0 c\dot{w}$ is introduced phenomenologically and ρ_0 is the mass density of pristine graphene. The tension of the membrane $T_{X,Y}$ depends on the out-of-plane displacement

$$T_X = T_Y = T_0 + T_1\|\nabla w\|^2,$$

where T_0 is the initial uniform biaxial tension and $T_1 = \lambda/2 + \mu \approx 112$ N/m, cf. Eq. (2.24). The tension at zero deflection, T_0, is a free parameter which determines the vibrational resonance frequency of small oscillations.

Adsorption of a small particle on the membrane changes the bare mass density ρ_0 to

$$\rho(\bar{X}) = \rho_0 + m\delta(\bar{X} - \bar{X}_p), \tag{3.3}$$

where the mass and position of the particle are m and $\bar{X}_p = (X_p, Y_p)$, respectively, and $\delta(\bar{X})$ is the Dirac delta function in two dimensions. I assume that the particle size is much smaller than the membrane size.

Below, I consider two-dimensional resonators with degenerate eigenmodes and, in particular, a square graphene resonator with side length L_0 and bare mass $M = \rho_0 L_0^2$. I also introduce relative coordinates $\bar{x} = \bar{X}/L_0$, length scale $h_0 = L_0\sqrt{T_0/T_1}$ for the out-of-plane displacement and time scale $t_0 = L_0\sqrt{\rho_0/T_0}$. The out-of-plane displacement $w(X,Y,t)$ is scaled as

$$u(x,y,\tau) = w(L_0 x, L_0 y, t_0\tau)/h_0. \tag{3.4}$$

I expand $u(\bar{x},\tau)$ in terms of the normalized eigenmodes $\phi_m(\bar{x})$ of the corresponding linearized problem, cf. Eq. (3.7),

$$u(\bar{x},\tau) = \sum_{m=1}^{\infty} u_m(\tau)\phi_m(\bar{x}). \tag{3.5}$$

The eigenmode vibrational amplitudes $u_m(\tau)$ satisfy the following system of coupled Duffing equations

$$D_m(\ddot{u}_m + \omega_m^2 u_m) + \gamma\dot{u}_m + \sum_{r,s,t=1}^{\infty} A_{mrst} u_r u_s u_t = p_m(\tau), \tag{3.6}$$

where ω_m is the scaled eigenfrequency of the mth eigenmode,

$$D_m = 1 + (m/M)\phi_m^2(\bar{x}_p),$$

the scaled damping coefficient is $\gamma = ct_0$, the coefficients of the nonlinear terms are $A_{mrst} = \iint dxdy\,(\nabla\phi_m \cdot \nabla\phi_r)(\nabla\phi_s \cdot \nabla\phi_t)$, the scaled driving force of the mth mode is

$$p_m(\tau) = \iint dxdy\,\phi_m(\bar{x})p_z(\bar{x},\tau),$$

and $p_z(\bar{x},\tau) = P_z(L_0\bar{x}, t_0\tau)t_0^2/(\rho_0 h_0)$ is the scaled applied pressure.

3.2.2 Graphene resonators in the linear regime

The eigenmodes (vibrational modes) are defined by the following eigenvalue problem

$$\nabla^2\phi_n = -\tilde{\rho}(\bar{x})\omega_n^2\phi_n, \tag{3.7}$$

where $\phi_n(\bar{x})$ and ω_n are the spatial profile and the scaled eigenfrequency of the nth eigenmode, respectively. The parameters of the adsorbed particle m, $\bar{x}_p$ enter in the scaled eigenfrequencies ω_n through the scaled mass density

$$\tilde{\rho}(\bar{x}) = 1 + (m/M)\delta(\bar{x} - \bar{x}_p).$$

For $\epsilon \equiv m/M \ll 1$, the eigenvalue problem (3.7) may be solved using perturbation theory with ϵ as the small parameter. The unperturbed problem is

$$\nabla^2\phi_{n0} = -\omega_{n0}^2\phi_{n0}. \tag{3.8}$$

For nondegenerate modes of the unperturbed problem, the scaled eigenfrequencies ω_n are equal to

$$\omega_n^2 = \omega_{n0}^2(1 - \epsilon\phi_{n0}^2(\bar{x}_p)) + \mathcal{O}(\epsilon^2). \tag{3.9}$$

Thus, for nondegenerate eigenmodes, the mass responsivity function $\mathcal{R}_n(\bar{x})$ is

$$\mathcal{R}_n(\bar{x}) = \frac{1}{2}\phi_{n0}^2(\bar{x}). \tag{3.10}$$

In general, for two degenerate modes of the unperturbed problem (3.8), the added mass splits the frequency degeneracy in such a way that only one of the eigenmodes lowers its eigenfrequency whereas the other does not vary its eigenfrequency to all orders in ϵ. The latter eigenmode has a node line which contains the adsorption point of the particle, $\bar{x}_p$.

For a square resonator, the spatial profiles of the first two degenerate modes of the eigenvalue problem (3.8) are

$$\phi_{20}(x,y) = 2\sin(\pi x)\sin(2\pi y) \quad \text{and} \quad \phi_{30}(x,y) = 2\sin(2\pi x)\sin(\pi y). \tag{3.11}$$

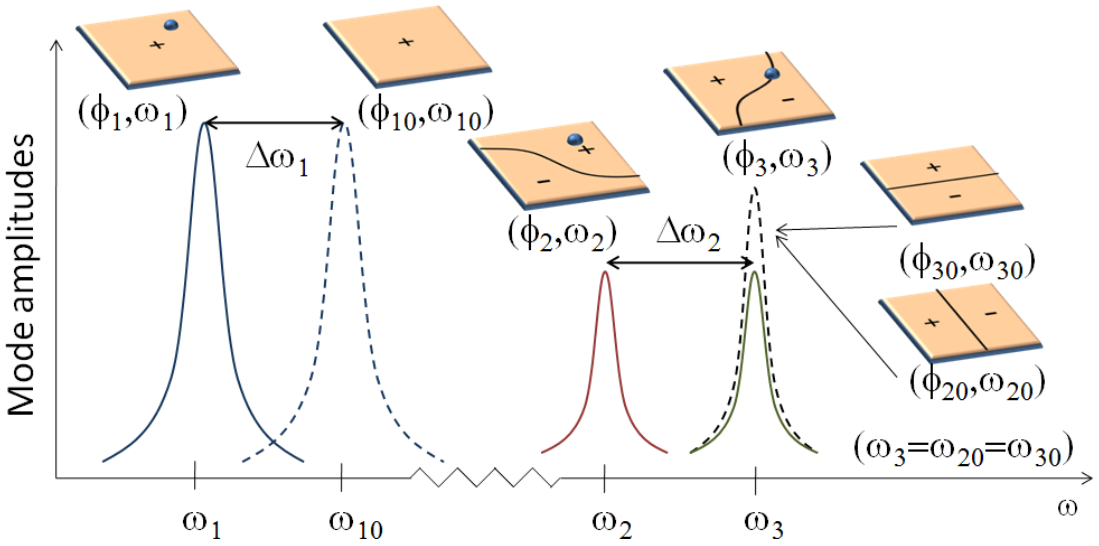

Figure 3.2: Amplitudes for the three lowest lying flexural eigenmodes as functions of drive frequency ω for weak driving. **Dashed lines:** Linear response in the absence of added mass. The unperturbed mode shapes are written ϕ_{10}, ϕ_{20} and ϕ_{30} and are indicated on the plaquettes. The plaquettes show the location of nodelines and the '$\pm$'-signs show the antinodes. The two modes ϕ_{20} and ϕ_{30} are degenerate. **Solid lines:** Linear response in the presence of an added mass. The mode functions are ϕ_1, ϕ_2 and ϕ_3. Their shapes are indicated on the plaquettes with a blue dot at the location of the added mass.

These eigenmodes have scaled eigenfrequencies equal to $\omega_{20} = \omega_{30} = \sqrt{5}\pi$. The added mass splits the frequency degeneracy and the new eigenfrequencies are

$$\begin{aligned} \omega_2^2 &= \omega_{20}^2(1-\epsilon\mathcal{N}^2) \\ \omega_3 &= \omega_{30}, \end{aligned} \tag{3.12}$$

where $\mathcal{N} = [\tilde{\phi}_2^2 + \tilde{\phi}_3^2]^{1/2}$, $\tilde{\phi}_k = \phi_{k0}(\bar{x}_p)$ and $k = \{2,3\}$. Also, the corresponding eigenmodes spatial profile, to zeroth order in ϵ, are $\phi_2(\bar{x}) = [\tilde{\phi}_2\phi_{20}(\bar{x}) + \tilde{\phi}_3\phi_{30}(\bar{x})]/\mathcal{N}$ and $\phi_3(\bar{x}) = [\tilde{\phi}_2\phi_{30}(\bar{x}) - \tilde{\phi}_3\phi_{20}(\bar{x})]/\mathcal{N}$. Note that $\phi_3(\bar{x}_p)$=0. These results are depicted in Fig. 3.2.

The analytical formulas (3.9) and (3.12) can be used to uniquely determine the parameters m, x_p and y_p of the adsorbed particle. Using Eqs. (3.9) and (3.12) for, e.g., the modes 1, 2 and 4 (modes are labeled in ascending order with respect to their eigenfrequency), I obtain the following equations for the particle position, $\bar{x}_p = (x_p, y_p)$,

$$\begin{aligned} 1 - s \equiv \frac{1}{10}\frac{\omega_{20}^2 - \omega_2^2}{\omega_{10}^2 - \omega_1^2} &\approx \cos^2(x_p\pi) + \cos^2(y_p\pi), \\ \frac{1}{16}\frac{\Delta\omega_4/\omega_4}{\Delta\omega_1/\omega_1} &\approx \cos^2(x_p\pi)\cos^2(y_p\pi). \end{aligned} \tag{3.13}$$

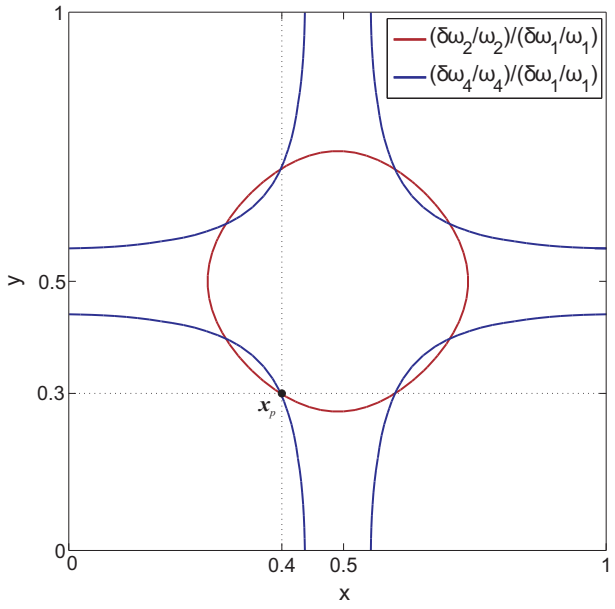

Figure 3.3: Determination of the location $\bar{x}_p = (x_p, y_p)$ of the analyte using Eqs. (3.9) and (3.12). The exact values are $x_p = 0.4$ and $y_p = 0.3$.

The solution of the above equations is depicted in Fig. 3.3. The position of the analyte is obtained up to the symmetry of the square. The analyte mass m is obtained from $m = \mathcal{R}_1^{-1} M \Delta\omega_1$.

3.2.3 Graphene resonators in the nonlinear regime

Nonlinear dynamics is treated in the weakly nonlinear regime and it is also assumed that the system is underdamped. The equation of motion for the vibrational mode amplitudes $u_m(\tau)$ are, cf. Eq. (3.6),

$$\ddot{u}_m + \omega_m^2 u_m + \tilde{\epsilon}\gamma\dot{u}_m + \sum_{r,s,t=1}^{\infty} \tilde{\epsilon}(1 - \epsilon\tilde{\phi}_m^2) A_{mrst} u_r u_s u_t = \tilde{\epsilon} p_m(\tau)(1 - \epsilon\tilde{\phi}_m^2) + \mathcal{O}(\epsilon^2), \tag{3.14}$$

where $\epsilon \equiv m/M \ll 1$, $\tilde{\phi}_m = \phi_{m0}(\bar{x}_p)$ and $\phi_{m0}(\bar{x})$ is the spatial profile of the mth unperturbed eigenmode, cf. Eq. (3.8). Above, I have also introduced another small parameter $\tilde{\epsilon} \ll 1$ to point out that we are dealing with a weakly nonlinear underdamped system. In what follows I neglect all second order terms in ϵ and $\tilde{\epsilon}$ in Eq. (3.14).

In the mass sensing scheme only the first three vibrational modes are directly driven near resonance. Hence, it is only necessary to consider the equa-

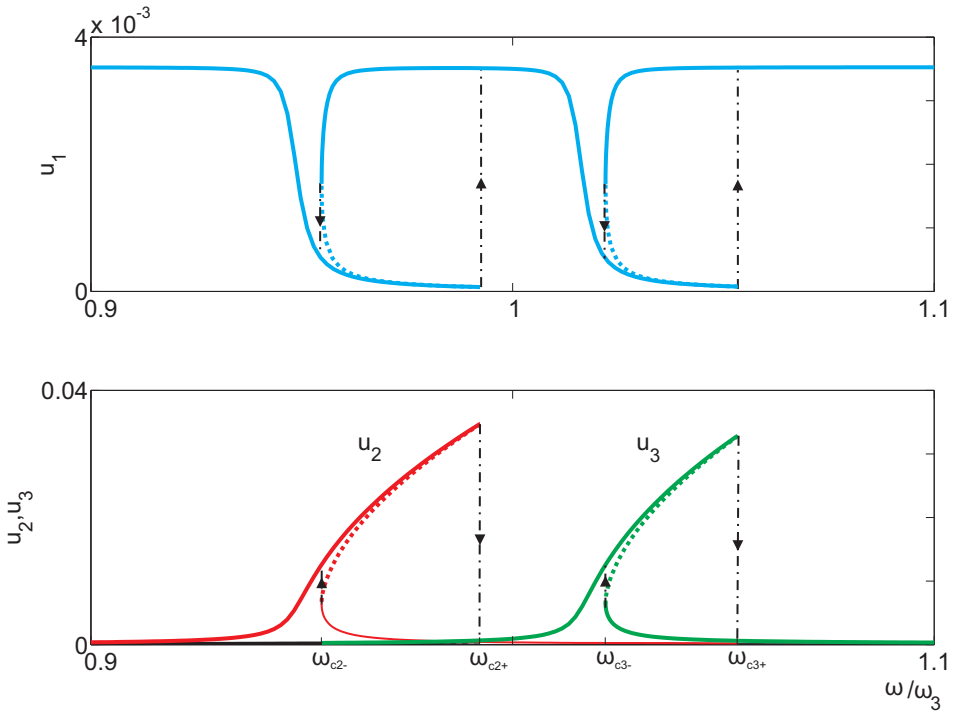

Figure 3.4: Dynamical response of the system when modes 1, 2 and 3 are simultaneously driven near resonance, cf. Eq. (3.15). Mode 1 is driven in the linear regime at resonance with $p_1(\tau) = p_1 \cos(\omega_1 \tau)$ and the modes 2 and 3 are driven in the weakly nonlinear regime with $p_2(\tau) = p_2 \cos(\omega\tau)$ and $p_3(\tau) = p_3 \cos(\omega\tau)$, respectively. These modes are parametrically coupled through Eqs. (3.15). This type of coupling enables us to determine the resonance frequencies and saddle-node bifurcation frequencies $\omega_{c,2\pm}$ and $\omega_{c,3\pm}$ of the system from measurements performed only on mode 1.

tions of motion of these modes and Eq. (3.14) simplifies to ($\tilde{\epsilon} = 1$)

$$\begin{aligned} u_1'' + \gamma u_1' + (\omega_1^2 + 5[Au_2^2 + Au_3^2])u_1 + Au_1^3 &= p_1(\tau), \\ u_2'' + \gamma u_2' + (\omega_2^2 + 5[Au_1^2 + Cu_3^2])u_2 + Bu_2^3 &= p_2(\tau), \\ u_3'' + \gamma u_3' + (\omega_3^2 + 5[Au_1^2 + Cu_2^2])u_3 + Bu_3^3 &= p_3(\tau), \end{aligned} \tag{3.15}$$

where $A = 5\pi^4$, $B = 161\pi^4/4 + 3\pi^4\tilde{\phi}_2^2\tilde{\phi}_3^2/(2\mathcal{N}^4)$, $C \approx 41\pi^4/5$ and $\mathcal{N} \equiv \left[\tilde{\phi}_2^2 + \tilde{\phi}_3^2\right]^{1/2}$. To first order in ϵ, the resonance frequency of the fundamental mode is $\omega_1 = \omega_{10}(1 - \epsilon\tilde{\phi}_1^2/2)$, and, for a square membrane, $\omega_2 = \omega_{20}(1 - \epsilon\mathcal{N}^2/2)$ and $\omega_3 = \omega_{20}$. The unperturbed scaled eigenfrequencies are $\omega_{10} = \sqrt{2}\pi$ and $\omega_{20} = \omega_{30} = \sqrt{5}\pi$. Comparison between numerical solution of the full equations (3.6) and the approximate equations (3.15) justifies the approximations leading to Eqs. (3.15).

Figure 3.4 depicts the response of the system when modes 1, 2 and 3 are simultaneously driven near resonance. Mode 1 is driven in the linear regime with $p_1(\tau) = p_1 \cos(\omega_1 \tau)$, and modes 2 and 3 are driven in the nonlinear regime

with $p_2(\tau) = p_2 \cos(\omega\tau)$ and $p_3(\tau) = p_3 \cos(\omega\tau)$, respectively. If the frequency splitting $|\omega_2 - \omega_3|$ is not too small, the dynamics of modes 2 and 3 can be described by two Duffing oscillators [55]. These two Duffing oscillators, above certain critical drive strength, exhibit bistability in a narrow frequency range: $\omega \in [\omega_{c2-}, \omega_{c2+}]$ (mode 2) and $\omega \in [\omega_{c3-}, \omega_{c3+}]$ (mode 3), where $\omega_{c2\pm}$ and $\omega_{c3\pm}$ are the saddle-node bifurcation frequencies of the second and third eigenmode, respectively, cf. Fig. 3.4. The stable dynamical states within the bistability regions are states with constant amplitude and phase. However, if the bistability regions of modes 2 and 3 significantly overlap (for small enough $|\omega_2 - \omega_3|$), then stable states with oscillating amplitude and phase may also develop (limit cycles) [5].

Equation (3.15) indicates that the resonance frequency of one mode depends parametrically on the square of the oscillation amplitude of the other modes. I refer to this type of coupling as *parametric coupling*. Specifically, from Eq. (3.15), the parametric coupling between the driven modes 1, 2 and 3 leads to an effective resonance frequency of the fundamental mode: $\omega_{1eff} = \omega_1^2 + 5A^2\big(\langle u_2\rangle^2 + \langle u_3\rangle^2\big)$, where $\langle\cdot\rangle$ denotes time average over the oscillation period ($\approx 2\pi/\omega_{20}$) of modes 2 or 3. This type of coupling can be used to determine the frequencies $\omega_{2,3}$, $\omega_{c2\pm}$ and $\omega_{c3\pm}$ from measurements performed on the mode 1. For instance, for the situation depicted in Fig. 3.4, each time that the driving frequency ω is swept through $\omega_{2,3\pm}$, the abrupt jumps in the oscillation amplitudes of modes 2 and 3 induce also jumps in the oscillation amplitude of the probed mode 1, which is driven all the time at resonance in the linear regime [6].

3.2.4 The mass measurement scheme

The goal of the present mass measurement scheme is to determine the position and mass of the adsorbed particle on the square membrane. The particle position is determined from the parameters r and s,

$$r \equiv \cos^2(\pi y_p)/\cos^2(\pi x_p), \tag{3.16}$$

$$s \equiv 1 - [\cos^2(\pi x_p) + \cos^2(\pi y_p)]. \tag{3.17}$$

The parameter $s(\omega_1, \omega_2)$ is determined by the resonance frequencies of the modes 1 and 2, cf. Eqs. (3.9) and (3.12),

$$1 - s \approx \frac{1}{10}\frac{\omega_{20}^2 - \omega_2^2}{\omega_{10}^2 - \omega_1^2}. \tag{3.18}$$

In order to determine r, the resonator is driven into the nonlinear regime with a special scaled pressure $p_z(\bar{x}, \tau) = p(\tau)g(\bar{x})$ where $g(\bar{x})$ obeys the symmetry relation: $g(x, y) = g(|x - 0.5|, y)$ and x, $y \in [0, 1]$. Then, the scaled forces that

appear in Eq. (3.15) are

$$\begin{aligned} p_1(\tau) &= D_1 p(\tau), \\ p_2(\tau) &= D_2 p(\tau)\cos(\pi y_p) \\ p_2(\tau) &= D_2 p(\tau)\cos(\pi x_p), \end{aligned}$$

where $D_1 = \int d^2\bar{x}\,\phi_{10}(\bar{x})g(\bar{x})$ and $D_2 = \int d^2\bar{x}\,\phi_{30}(\bar{x})g(\bar{x})/\mathcal{N}$. The ratio of the scaled forces $p_2(\tau)$ and $p_3(\tau)$ is equal to $\sqrt{r}$. For a Duffing oscillator, it can be shown that, cf. appendix of paper III, $(\omega_n^2 - \omega_{cn-}^2)^3 \approx (9/4)^2 B p_n^2$ $(n = 2, 3)$ where ω_{cn-} is the smallest saddle-node bifurcation frequency of the nth mode, cf. Fig. 3.4. The parameter $r(\omega_{c2-}, \omega_{c3-})$ is given by

$$r = \left(\frac{\omega_2^2 - \omega_{c2-}^2}{\omega_3^2 - \omega_{c3-}^2}\right)^3. \tag{3.19}$$

Hence, both parameters $s(\omega_1, \omega_2)$ and $r(\omega_{c2-}, \omega_{c3-})$ are determined by frequency measurements in the linear and nonlinear regimes, respectively. The position of the particle is determined up symmetry of the square from r and s, cf. Eqs. (3.16) and Eq. (3.17), the mass responsivity $\mathcal{R}_1$ can be written in terms of r and s as

$$\mathcal{R}_1(\bar{x}_p) = -2\omega_{10}\frac{(s+r)(1+rs)}{(1+r)^2}, \tag{3.20}$$

and the mass of the particle is $m = \mathcal{R}_1^{-1} M \Delta\omega_1$.

Figure 3.5 depicts the scheme for single-particle mass measurement. First, we find out whether there is a single analyte adsorbed on the resonator. This is done by measuring the frequency shifts of the fundamental mode, $\Delta\omega_1$, and of the mode 3, $\Delta\omega_3$. A finite $\Delta\omega_1$ indicates that there are adsorbed particles on the membrane. A vanishing $\Delta\omega_3$ indicates that the adsorbed particles are located on the nodal line of mode 3 (very unlikely for a uniform flux of particles). If $\Delta\omega_1 \neq 0$ and $\Delta\omega_3 = 0$, we have a single-particle adsorption event and then we may proceed with the nonlinear part of the scheme. Here, the resonator is driven into the nonlinear regime and the saddle-node bifurcation frequencies ω_{c2-} and ω_{c3-}, cf. Fig. 3.4, are measured. Then we use Eqs. (3.18), (3.19) and (3.20) to calculate the particle position $\bar{x}$, mass responsivity $\mathcal{R}_1$ and the particle mass m.

All the quantities needed by the mass measurement scheme ($\omega_{1,2,3}$, ω_{c2-} and ω_{c3-}) can be measured by a narrow-band detector tuned at the fundamental mode resonance frequency, cf. appended paper III.

3.2.5 Performance study

In this section I discuss the sensitivity and range of applicability of the mass measurement scheme. Let us consider first the range of values of m where the scheme is applicable. The upper limit for m comes from the requirement that

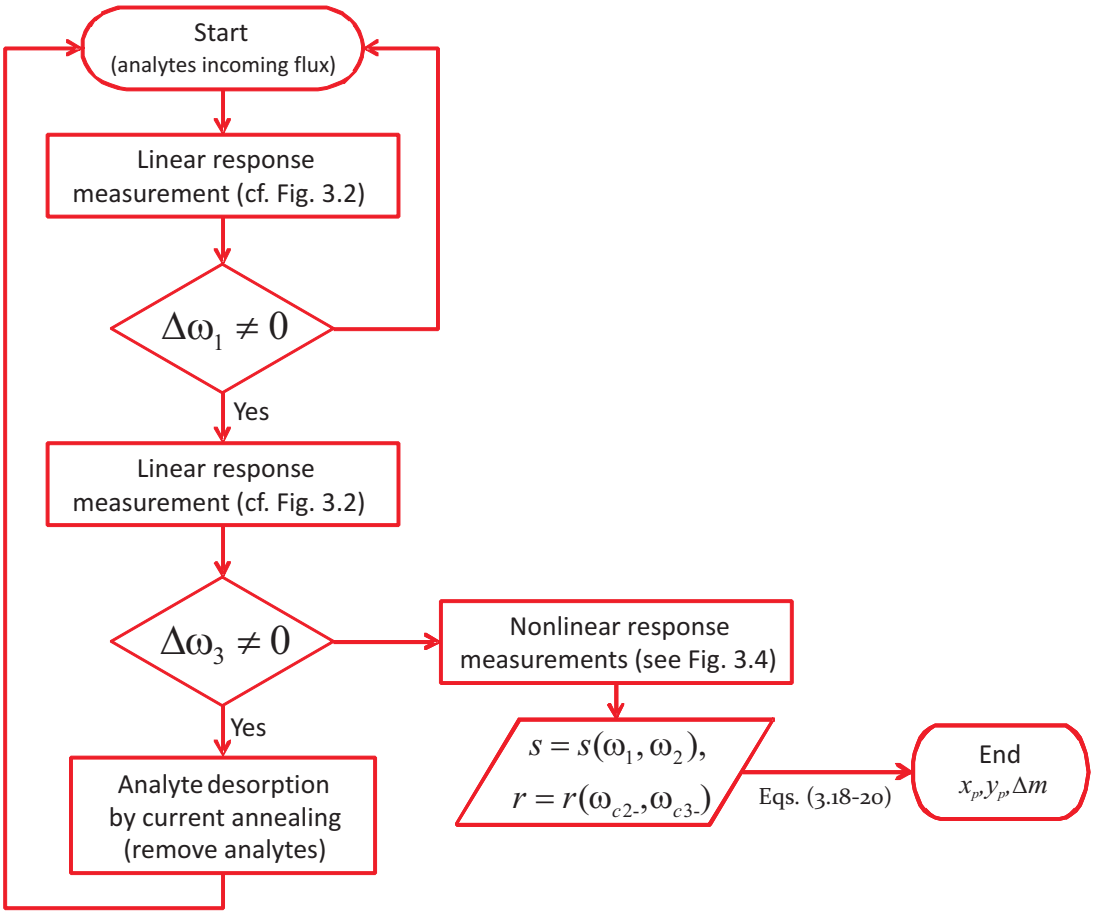

Figure 3.5: Single-particle mass measurement scheme.

the analyte mass should be much smaller than the resonator mass, i.e. $m \ll M$, for the above results, based on perturbation theory in ϵ, to hold [cf. Fig. 3.6 (a)]. The lower limit for m comes from the requirement that the bistability regions of modes 2 and 3 should not overlap, cf. Fig. 3.4. This imposes the following condition on the resonance frequencies of modes 2 and 3

$$\omega_3 - \omega_2 \geq \delta\omega_{2c} \equiv \frac{\sqrt{3}\omega_2}{2Q}, \tag{3.21}$$

where Q and $\delta\omega_{2c}$ are the quality factor and frequency detuning of the critical point for the onset of Duffing nonlinearity of the second eigenmode. Using the approximations for the resonance frequencies of modes 2 and 3, cf. Eqs. (3.9) and (3.12), in Eq. (3.21) leads to

$$\epsilon\big[\sin^2(\pi x_p)\sin^2(2\pi y_p) + \sin^2(2\pi x_p)\sin^2(\pi y_p)\big] \geq \frac{\sqrt{3}}{4Q}. \tag{3.22}$$

The above inequality does not hold for analytes landing close to the center of the square membrane, $\bar{x}_c = (0.5, 0.5)$. However, for $||\bar{x}_p - \bar{x}_c|| \ll 1$, the knowledge of the particle position is not critical because the mass responsivity of the fundamental mode, $\mathcal{R}_1(\bar{x}_p) \approx 1 + \mathcal{O}\big(\|\bar{x}_p - \bar{x}_c\|^2\big)$, is not very sensitive to $\bar{x}_p$. For a square resonator of side $L_0 = 1$ μm ($M \approx 760$ ag) and with a quality factor of $Q = 3000$, the scheme should work for analytes with mass larger than 1 ag (1 ag $\equiv 10^{-21}$ kg.).

Thermal noise and the system nonlinearity limit the relative precision with which the resonance frequency of the nth mode can be measured. The relative precision of the frequency measurements, $|\Delta\omega_n/\omega_n|$, is given by [67],

$$|\Delta\omega_n/\omega_n| < Q^{-1}10^{-\mathrm{DR_n}/20},$$

where DR_n is the dynamical range (determined by the thermal noise intensity and the nonlinearity of the system) of nth mode. For graphene, the dynamical ranges for modes $n = 1, 2, 3$ are

$$\mathrm{DR}_n = 10\log_{10}\left[\frac{R_n}{Q}\left(\frac{T_0}{T_1}\right)\frac{T_0 L_0^2}{k_B T}\right], \tag{3.23}$$

where $R_1 \approx 0.6$, $R_2 = R_3 \approx 0.3$ are constants, T_0 is the initial tension for flat graphene, $T_1 = \lambda/2 + \mu \approx 112$ N/m, T is the environment temperature and k_B is the Boltzmann constant. For instance, for a device with $L_0 = 1$ μm, $Q = 3000$, $\omega_1/2\pi = \sqrt{T_0/2M} = 2$ GHz and $T = 300$ K, the modes resonance frequencies can be determined with a precision of 1 ppm.

The saddle-node bifurcation frequencies ($\omega_{c2\pm}$, $\omega_{c3\pm}$) can be measured by sweeping the driving frequency ω upwards and downwards and making note of the driving frequencies when jumps in the fundamental mode vibrational amplitude occur [55]. This method fails in the presence of significant thermal

additive noise because the latter causes the jumps to occur before the onset of the saddle-node bifurcation [4]. However, it has been demonstrated that the saddle-node bifurcation frequencies (and also the natural resonance frequencies) can be indirectly determined by measuring the basin activation energies for transition between the stable foci. This method has been employed to measure the bifurcation saddle-node frequencies and the natural fundamental resonance frequency of a nanobeam with a relative precision of ≈ 0.1 ppm [68].

Figure 3.6 depicts the performance of the scheme. Figure 3.6 (a) demonstrates the applicability of the perturbation theory, cf. Eqs. (3.9) and (3.12). Inside the contour lines, perturbation theory holds up to an error of 5% for particles with relative mass $\epsilon \equiv m/M \leq \epsilon_{\max}$. Figure 3.6 (b) depicts the contours of minimum ϵQ where Eq. (3.19) is applicable. Recall that the latter equation was obtained in the limit of $Q \to \infty$ (cf. appendix of paper III) and under the assumption that the bistability regions of modes 2 and 3 do not overlap, cf. Eq. (3.22). Figure 3.6 (c) depicts a comparison between the true and predicted values of the mass and position of the adsorbed particle.

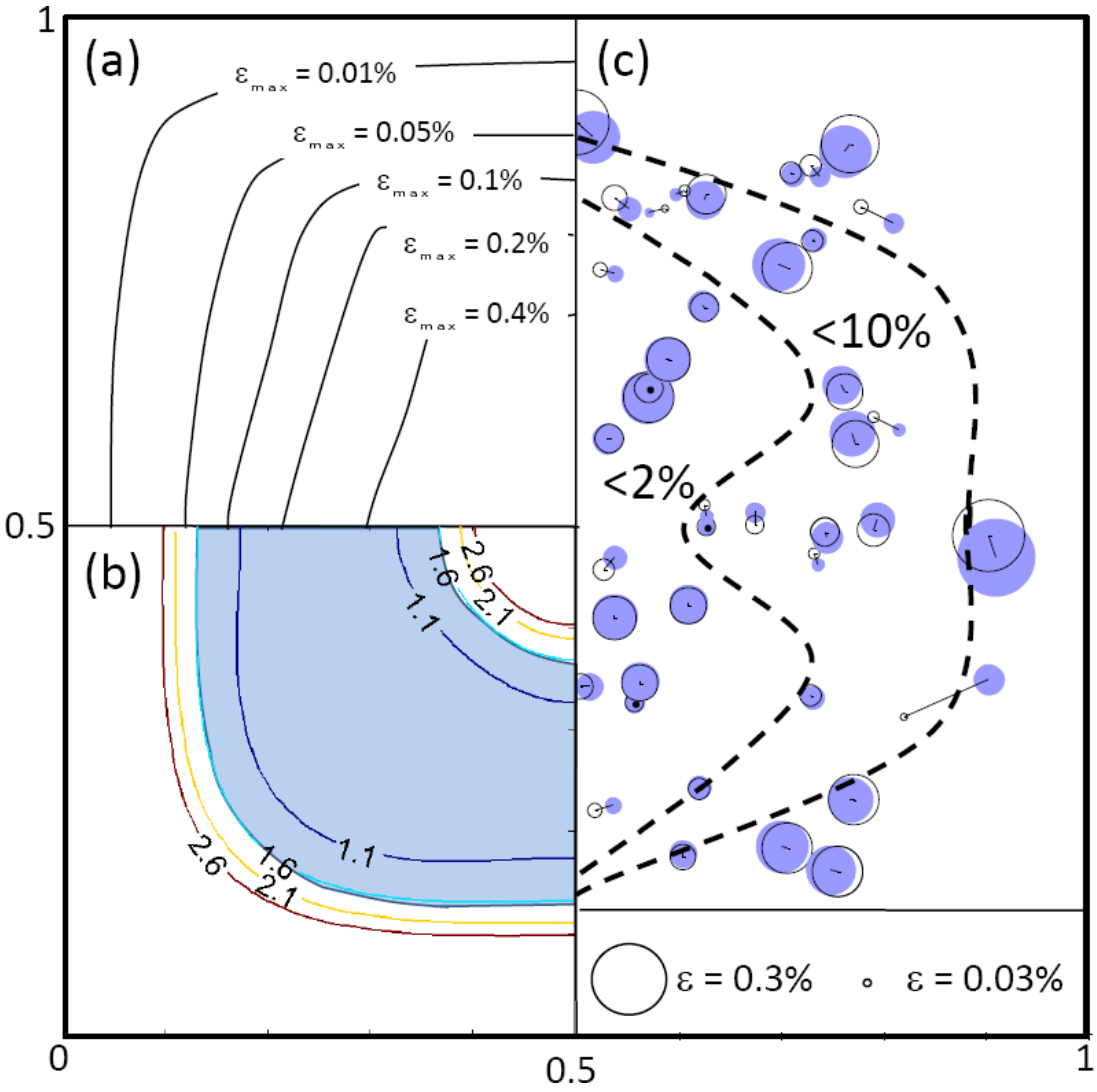

Figure 3.6: (a) Maximal values of $\epsilon \equiv m/M$ due to limitations of first order perturbation theory. Within each contour, first order perturbation theory in ϵ allows mass fractions up to $\epsilon_{\max}$ to be determined with a 5% accuracy. **(b)** Contours of minimum ϵQ where Eq. (3.19) is applicable. In the shaded area, Eq. (3.19) is valid for $\epsilon > 1.6/Q$. **(c)** Determination of randomly deposited masses using numerical integration of Eq. (3.6) for a sheet with $Q = 3000$. The masses were uniformly distributed in the range $0.02\% < \epsilon < 0.35\%$. Frequencies were determined using an accuracy of $|\Delta\omega/\omega| \approx 0.5 \cdot 10^{-4}$. The positions of the deposited masses are shown by shaded symbols. The open symbols are the positions determined by using equations (3.18) and (3.19). The size of the markers are proportional to ϵ. The dashed lines indicate regions where the relative error $|(\epsilon - \epsilon_{\text{exact}})/\epsilon_{\text{exact}}|$ is less than 2% or 10%.

CHAPTER 4

Mass-loading induced dephasing in nanomechanical resonators

In the previous chapter I described a mass sensing scheme to determine the mass and position of a particle, adsorbed on a square graphene resonator. It was assumed that the particle remains at the same spot during the frequency shifts measurements. In this chapter, I consider the case that the particle is not static. It performs a Brownian motion and attaches and detaches at random positions on the resonator. In this situation, the resonator vibrational modes change their eigenfrequencies because their effective masses change.

I study the effect of a fluctuating eigenfrequency in the susceptibility of a vibrational mode. One would think that the susceptibility is given by a weighted sum of partial susceptibilities, corresponding to the different possible values of the eigenfrequencies. I show that this simple picture does not apply when the frequency fluctuations have a comparatively short correlation time. I describe a general method, based on the Einstein-Fokker-Planck equation [69], to calculate the susceptibility and higher order moments of the vibrational amplitude of underdamped resonantly driven vibrational modes. I assume that the eigenfrequency noise does not depend on the vibrational state (no backaction). Backaction can arise in high frequency nanomechanical resonators loaded with particles and it can lead to bistability and rare interstate switching, cf. chapter 5.

I emphasize that the eigenfrequency noise can be characterized by studying the amplitude and phase fluctuations of forced oscillations. Specifically, under certain conditions, cumulants of the (complex, see below) amplitude fluctuations are nonzero if frequency noise is nonzero. Hence, nanomechanical resonators could be used to measure not only the mass of small particles but also transport-related quantities such as diffusion coefficients and binding energies [25]. The realization of these applications requires good models for the frequency noise. The transport-related parameters can then be obtained by comparison between the model predictions for the cumulants and experimental data.

4.1 The model

Nanomechanical resonators are known to have vibrational modes with very high quality factors (e.g., quality factors of $Q \sim 10^5$ have been recently achieved in CNT-based resonators [29,30]). Thus, it is a good approximation to model the dynamics of the mode amplitude, $q(t)$, as a harmonic oscillator weakly coupled to a thermal bath (e.g., phonons [4,8]). The equation of motion for the amplitude of the mode, driven near resonance, is

$$\ddot{q} + 2\Gamma\dot{q} + \omega_0^2 q = 2\frac{F}{M}\cos(\omega_F t) + f_T(t)/M, \tag{4.1}$$

where M is the effective mass of the vibrational mode, $F\cos(\omega_F t)$ is the driving force and ω_F is the driving frequency. The terms $2\Gamma\dot{q}$ and $f_T(t)$ are introduced by linear coupling to the bath modes for the special case of Ohmic dissipation [7]. The dissipative term is $2\Gamma\dot{q}$ and $f_T(t)$ is a white and Gaussian stochastic force with two-time correlation function:

$$\langle f_T(t_1) f_T(t_2)\rangle = 4k_B T\Gamma M\delta(t_1 - t_2).$$

Here, $\langle\cdot\rangle$ denotes ensemble average, T is the bath temperature, k_B is the Boltzmann constant, $\delta(\cdot)$ is the Dirac function and ω_0 is the renormalized vibrational frequency, which is approximately equal (again for weak coupling to the bath) to the bare mode eigenfrequency (given by the square root of the ratio between the spring constant and the effective mass) [7].

Because of the weak coupling to the bath ($\Gamma \ll \omega_0$), the oscillator state changes very little within the oscillation period $2\pi/\omega_F$. Thus, it is meaningful to introduce the slow complex dynamical variables $u(t)$ and $u^*(t)$, defined by

$$\begin{aligned} q(t) &= u(t)\exp(i\omega_F t) + u^*(t)\exp(-i\omega_F t), \\ \dot{q}(t) &= i\omega_F\big[u(t)\exp(i\omega_F t) - u^*(t)\exp(-i\omega_F t)\big]. \end{aligned} \tag{4.2}$$

The above transformation implies the condition

$$\dot{u}(t)\exp(i\omega_F t) + \dot{u}^*(t)\exp(-i\omega_F t) = 0.$$

The equation for $u(t)$ is (neglecting fast oscillating terms with frequency $2\omega_0$)

$$\dot{u}(t) = -[\Gamma + i\delta\omega]u(t) + \frac{F}{2iM\omega_F} + \tilde{f}_T(t), \tag{4.3}$$

where $\tilde{f}_T(t) = f_T(t)\exp(-i\omega_F t)/(2i\omega_F M)$ and

$$\langle \tilde{f}_T(t_1)\tilde{f}_T^*(t_2)\rangle = (k_B T\Gamma/M\omega_F^2)\delta(t_1 - t_2).$$

The equation for $u^*(t)$ is the complex conjugate of the equation for $u(t)$. The Markovian equation (4.3) for the slow dynamic variable $u(t)$ is also known as

the rotating wave approximation (RWA). The conditions for the applicability of the RWA are weak coupling to the bath ($\Gamma \ll \omega_0$) and that the coupling function $F(\omega)$ (this function is given by the density of states of the bath modes weighted by the coupling factors between the bath modes and the oscillator [7]) be smooth at $\omega \approx \omega_0$. The frequency detuning $\delta\omega \equiv \omega_F - \omega_0$ is also assumed to be small ($|\delta\omega| \ll \omega_0$). In the presence of frequency noise, Eq. (4.3) takes the form

$$\dot{u}(t) = -[\Gamma + i(\delta\omega - \xi(t))]u(t) + \frac{F}{2iM\omega_F} + \tilde{f}_T(t), \tag{4.4}$$

where the $\xi(t)$ is the frequency noise. The stochastic process $\xi(t)$ is assumed to be stationary and it is characterized by its standard deviation $\Delta \equiv \left\langle \left[\xi(t) - \langle\xi(t)\rangle\right]^2 \right\rangle^{1/2}$ and its correlation time τ_c, which is defined by $\left\langle \big(\xi(t) - \langle\xi(t)\rangle\big)\xi(0) \right\rangle \sim \Delta^2 \exp(-t/\tau_c)$. In what follows, the vibrational frequency ω_0 is the largest frequency in the theory,

$$\Delta, \tau_c^{-1}, \Gamma, |\delta\omega| \ll \omega_0, \quad \delta\omega \equiv \omega_F - \omega_0, \tag{4.5}$$

and there is no restriction in the relative size between the quantities appearing at the left-hand side of the above inequality.

The theoretical model is complete when the model for the stochastic process $\xi(t)$ is given. This process is assumed to be Markovian and defined by the master equation,

$$\partial_t p(\xi, t) = \hat{W} p(\xi) \equiv \sum_{\xi'} \hat{W}(\xi, \xi') p(\xi', t), \tag{4.6}$$

where $p(\xi, t)$ is the probability distribution of $\xi(t)$ at time t and $\hat{W}(\xi, \xi')$ is the matrix of transition probabilities per unit of time between different ξ-states. It is assumed that $\hat{W}$ does not depend on the oscillator state, $u(t)$. From Eq. (4.4), the joint probability density $P(u, u^*, \xi, t)$ satisfies the Einstein-Fokker-Planck equation [69]

$$\begin{aligned} \partial_t P(u, u^*, \xi, t) &= \hat{W}P + \partial_u\big([\Gamma + i(\delta\omega - \xi)]uP\big) - \frac{F}{2iM\omega_F}\partial_u P \\ &\quad + \partial_{u^*}\big([\Gamma - i(\delta\omega - \xi)]u^*P\big) + \frac{F}{2iM\omega_F}\partial_{u^*}P + \frac{k_B T\Gamma}{M\omega_F^2}\partial^2_{u,u^*}P. \end{aligned} \tag{4.7}$$

The average response of the oscillator to forced oscillations is given by

$$\langle q(t)\rangle = \langle u^*(t)\rangle e^{-i\omega_F t} + \langle u(t)\rangle e^{i\omega_F t} \equiv \frac{F}{2M\omega_F}\left[\chi(\delta\omega)e^{-i\omega_F t} + \chi^*(\delta\omega)e^{i\omega_F t}\right]. \tag{4.8}$$

The above equation defines the oscillator (scaled) susceptibility function, $\chi(\delta\omega)$. The scaled susceptibility can be calculated from

$$\chi(\delta\omega) = \left(\frac{2M\omega_F}{F}\right)\sum_{\xi}\int dudu^*\; u^* P_{st}(u, u^*, \xi), \tag{4.9}$$

where $P_{st}(u, u^*, \xi)$ is the stationary solution of Eq. (4.7). Because the additive noise $\tilde{f}_T(t)$ in Eq. (4.4) does not enter in the calculation of the moments of $u(t)$ [70], I set $\tilde{f}_T(t)$ to zero.

The oscillator susceptibility is determined by the interrelation between the oscillator energy relaxation rate, Γ, and the standard deviation, Δ, and the reciprocal correlation time τ_c^{-1} of the frequency noise. Now, I discuss the limit cases of slow ($\tau_c \to \infty$) and fast ($\tau_c \to 0$) frequency noise.

Let us assume for a moment that the process $\xi(t)$ has a discrete range of values. In the slow frequency noise limit, the correlation time, τ_c, is the largest time scale: $\tau_c \gg \Gamma^{-1}, \Delta^{-1}$. This implies that the noise process stays at a certain value $\xi(t) = \xi_0$ for a time long enough for the vibrational mode to relax to its stationary amplitude value, given by $(2M\omega_F/F)u^* = i[\Gamma - i(\delta\omega - \xi_0)]^{-1}$, cf. Eq. (4.4). Assuming that the system is ergodic, the susceptibility function $\chi(\delta\omega)$ is given by a sum of partial susceptibilities, $\chi(\xi; \delta\omega) = i[\Gamma - i(\delta\omega - \xi)]^{-1}$, weighted by the probability $p_{st}(\xi)$,

$$\chi(\delta\omega) \equiv \sum_{\xi} \chi(\xi; \delta\omega) \approx \sum_{\xi} \frac{ip_{st}(\xi)}{\Gamma - i(\delta\omega - \xi)}, \quad \tau_c \gg \max\{\Gamma^{-1}, \Delta^{-1}\}. \tag{4.10}$$

In the limit of fast frequency noise, the correlation time of the latter, τ_c, is much smaller than the oscillator ring down time, Γ^{-1}, and the characteristic time to resolve a frequency change equal to Δ (this time is $\gtrsim \Delta^{-1}$). In this limit, the oscillator can not resolve the frequency changes, separated by a time $\sim \tau_c$, and the partial susceptibilities corresponding to different ξ can not be distinguished,

$$\chi(\delta\omega) \approx \sum_{\xi} \frac{ip_{st}(\xi)}{\Gamma + \Delta^2\tau_c - i(\delta\omega - \langle\xi(t)\rangle)}, \quad \omega_0^{-1} \ll \tau_c \ll \min\{\Gamma^{-1}, \Delta^{-1}\}. \tag{4.11}$$

The oscillator absorption spectrum (imaginary part of the susceptibility) is a Lorentzian centered at $\langle\xi(t)\rangle$. The increase $\Delta^2\tau_c$ in the linewidth is the result of phase diffusion. The accumulated phase $\varphi(\bar{T}) = \sum_{i=0}^{i=N-1} \int_{t_i}^{t_{i+1}} ds \, \left[\xi(s) - \langle\xi(s)\rangle\right]$ (where $t_0 = 0$, $t_N = \bar{T}$, $t_{i+1} - t_i = \Delta t$ and $\tau_c \ll \Delta t \ll \Gamma^{-1}, \Delta^{-1}$) can be seen as the position of a random walker on the line with diffusion coefficient $D_\varphi = 2\Delta^2\tau_c$ and $\langle\varphi^2(\bar{T})\rangle = D_\varphi\bar{T}$. The Lorentzian shape of the absorption spectrum in the limit of fast frequency fluctuations is known in the field of nuclear magnetic resonance as motional narrowing (the absorption spectral line becomes narrower as the frequency fluctuations get faster). Moreover, this is the limit case where the theory of spectral linewidths of Weisskopf-Wigner [71] cannot be applied because the assumption that the linewidths be smaller than the transition energies or frequencies does not hold.

4.2 The method of the interfering partial susceptibilities

Here, I derive the equation that determines the partial susceptibilities for a Markovian type of frequency noise, cf. Eq. (4.6). Multiplying equation (4.7) by u^* and integrating over the variables u and u^* (and assuming that $P \to 0$ for $|u| \to \infty$), I find that the partial susceptibilities $\chi(\xi;\delta\omega)$ satisfy the equation

$$(\Lambda^* + i\xi)\chi(\xi;\delta\omega) - \hat{W}\chi(\xi;\delta\omega) = ip_{st}(\xi), \tag{4.12}$$

where $\Lambda = \Gamma + i\delta\omega$ and $p_{st}(\xi)$ is the stationary solution of Eq. (4.6). Note that the operator $\hat{W}$, defining the frequency noise, couples the partial susceptibilities. The total susceptibility, $\chi(\delta\omega)$, results from the interference of the coupled complex partial susceptibilities, $\chi(\xi;\delta\omega)$,

$$\chi(\delta\omega) = \sum_{\xi} \chi(\xi;\delta\omega). \tag{4.13}$$

In the limit case of slow frequency noise ($\tau_c \gg \Gamma^{-1}, \Delta^{-1}$), the second term on the left-hand side of Eq. (4.12) can be neglected and then we obtain the result given by Eq. (4.10). In the limit of fast frequency noise ($\tau_c \ll \Gamma^{-1}, \Delta^{-1}$), we have that $\hat{W}\chi(\xi;\delta\omega) \approx 0$ and the partial susceptibilities are proportional to $p_{st}(\xi)$. The proportionality constant can be obtained by projecting Eq. (4.12) over the left eigenvector, with zero eigenvalue, of $\hat{W}$. This leads us to the result (to zeroth order in τ_c) given by Eq. (4.11).

4.3 Specific cases

In this section I consider frequency noise models, which are relevant for mass measurement applications based on NEM resonators. I discuss first the case where one analyte freely diffuses along a one-dimensional resonator. The analyte is not allow to leave the resonator. Next, I consider the situation where analytes enter (adsorption) and leave (desorption) a certain fixed point of the resonator. Here, there is no diffusion. Finally, I present a frequency noise model which accounts for diffusion and adsorption and desorption of particles at random points on the resonator.

4.3.1 Diffusion-induced dephasing in nanomechanical resonators

This section summarizes the results of paper IV for diffusion-induced dephasing in nanomechanical resonators. As discussed in chapter 3, the eigenfrequency shift $\xi(t) = \Delta_D(x(t))$ of a certain eigenmode, due to a particle located

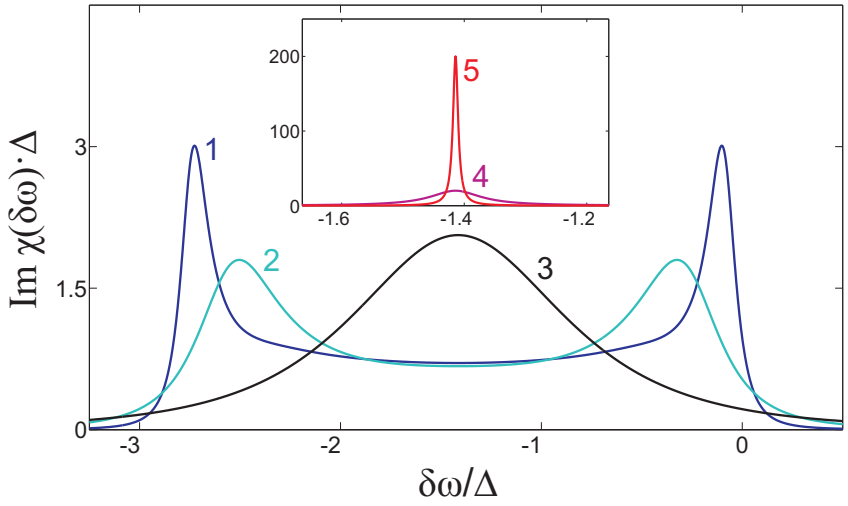

Figure 4.1: Oscillator absorption spectrum, Im$\chi(\delta\omega)$, for the fundamental mode of a doubly clamped resonator with a particle freely diffusing along it. The frequency detuning, $\delta\omega = \omega - \omega_0$, is scaled by the standard frequency deviation Δ. Curves 1 through 5 refer to $\Delta\tau_c = 50, 5, 0.5, 0.05$ and 0.005, respectively. These results refer to resonator damping rate $\Gamma = 0$.

at $x(t)$, is

$$\Delta_D(x) = -\frac{m\omega_0}{2M}\phi^2(x), \tag{4.14}$$

where m is the particle mass, $M \gg m$ is the eigenmode vibrational effective mass and $\phi(x)$ is the mode shape. Below, I consider the fundamental flexural mode with $\phi(x) = \sqrt{2}\cos(\pi x/L)$ (this mode shape is an approximation for the mode profile of the fundamental flexural mode of a doubly clamped nanobeam near the antinode). The Brownian motion of the adsorbed particle is described by the (Stratonovich) stochastic differential equation [69]

$$m\kappa\dot{x} = -\partial_x U(x) + m\kappa D^{1/2}\zeta(t), \tag{4.15}$$

where κ is the friction coefficient of the particle, D is the diffusion coefficient and $\zeta(t)$ is a Gaussian white process with two-time correlator: $\langle\zeta(t_1)\zeta(t_2)\rangle = 2\delta(t_1 - t_2)$. The diffusion coefficient is related to the friction coefficient by the Einstein relation $D\kappa m = k_B T$. I have also included a potential $U(x)$ (implemented by, e.g., surface functionalization), which may confine the motion of the particle to a certain region on the resonator. The particle is assumed to be overdamped; i.e., the inertia term $m\ddot{x}$ has been neglected in Eq. (4.15). Note also that $U(x)$ does not depend on the oscillator state. This possibility (back-action) will be discussed in chapter 5.

The equation for the partial susceptibility density $\chi(x;\delta\omega)$ is

$$\big(\Lambda^* + i\Delta_D(x)\big)\chi(x;\delta\omega) - D\big[\partial_x^2\chi(x;\delta\omega) + \frac{1}{k_BT}\partial_x(U'(x)\chi(x;\delta\omega))\big] = ip_{st}(x). \tag{4.16}$$

In paper IV, the above equation has been solved for $U(x) = \alpha(x - x_0)^2$ (harmonic confining potential) and $U(x) = 0$ (free diffusion), subject to the condition that the particle is not allowed to leave the resonator (this implies reflecting boundary conditions in $\chi(x;\delta\omega)$: $D\partial_x\chi(x;\delta\omega) + (1/k_BT)U'(x)\chi(x;\delta\omega) = 0$ at $x = \pm L/2$).

Figure 4.1 depicts the results for free diffusion. In this case, the frequency noise has a standard deviation equal to $\Delta = \omega_0 m/(M\sqrt{8})$ and correlation time equal to $\tau_c = (L/2\pi)^2/D$. The latter is proportional to the time for the particle to diffuse a distance equal to the resonator length, L. Figure 4.1 shows how the oscillator absorption spectrum, $\mathrm{Im}\chi(\delta\omega)$, changes as function of the scaled frequency detuning, $\delta\omega/\Delta$. For particles diffusing fast along the resonator ($\tau_c \ll \Delta^{-1}$), the absorption spectrum converges to a Lorentzian line with a linewidth $\approx \Gamma + \Delta^2\tau_c$ (motional narrowing).

For slow diffusing particles ($\tau_c \gg \Delta^{-1}$), the absorption spectrum acquires a shape very different from the conventional Lorentzian shape, cf. Fig. 4.1. In this particular case, the absorption spectrum has two peaks at $\delta\omega = \{-\gamma, 0\}$, where $\gamma = \omega_0 m/M$. These peaks are a consequence of a divergent (density of states) $p_{st}(\xi)$ at $\xi_{\min} = -\gamma$ and $\xi_{\max} = 0$. This density of states is defined by $p_{st}(\xi) \equiv \big\langle\delta\big(\xi - \Delta(x(t))\big)\big\rangle_{x(t)} = [-\Delta(\gamma + \Delta)]^{-1/2}/\pi$, and

$$\chi(\delta\omega) \approx \int_{-\gamma}^{0} d\xi\, \frac{ip_{st}(\xi)}{\Gamma - i(\delta\omega - \xi)}, \quad \tau_c \to \infty.$$

From the above expression, the absorption spectrum can be calculated in the limit of $\Gamma \to 0^+$,

$$\mathrm{Im}\chi(\delta\omega) \approx \int_{-\gamma}^{0} d\xi\, \pi\delta(\delta\omega - \xi)p_{st}(\xi) = \frac{1}{\sqrt{-\delta\omega(\gamma + \delta\omega)}}\Theta(-\delta\omega)\Theta(\gamma + \delta\omega), \tag{4.17}$$

where $\Theta(\cdot)$ is the Heaviside function. Thus, the scaled susceptibility diverges as $|\delta\omega|^{-1/2}$ close to the edges of the frequency noise range.

4.3.2 Dephasing induced by adsorption and desorption of particles in a nanomechanical resonator

The method of the interfering partial susceptibilities has been used in the previous section to calculate the susceptibility of an oscillator subject to a continuous, non-Gaussian and colored (finite correlation time) frequency noise process. In this section, I consider the case where the frequency noise results from particles attaching and detaching at a fixed point, x_0, on the resonator

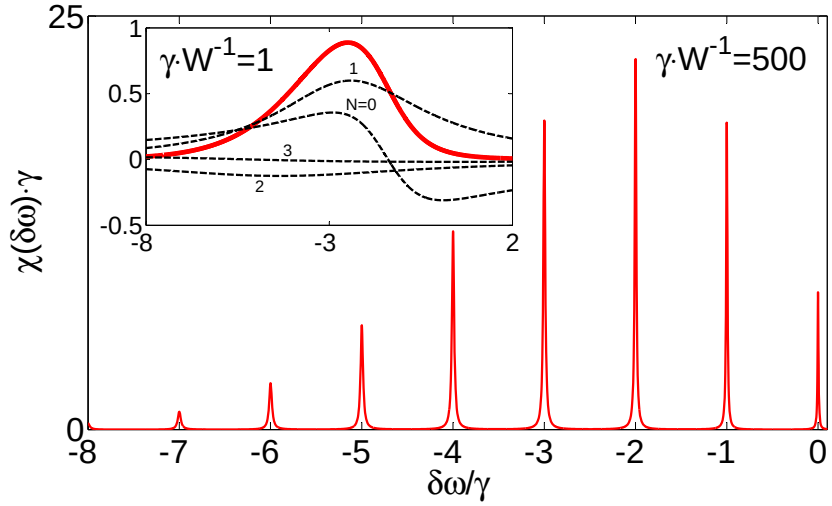

Figure 4.2: Oscillator absorption spectrum, Im$\chi(\delta\omega)$, for a resonator eigenmode with particles attaching and detaching from a fixed spot (no diffusion). The spectrum is given as function of the scaled frequency detuning, $\delta\omega/\gamma$, where γ is the frequency shift caused by adsorption or desorption of a particle. The desorption rate is W. **Inset:** Limit case of comparatively fast adsorption and desorption, $W \gtrsim \gamma$. The dashed curves depict the partial absorption spectra, Im$\chi(N;\delta\omega)$, corresponding to N particles on the resonator. The solid curve depicts the total absorption spectrum in the motional narrowing limit.

and the particles do not diffuse [72]. The frequency noise is discrete and it is given by

$$\xi(t) = -\gamma N(t), \tag{4.18}$$

where $\gamma = \phi^2(x_0)\omega_0 m/2M$ [Eq. (4.14)] is the size of the frequency jump when a particle attaches or detaches from the resonator and $N(t) = \{0, 1, ...\}$. I assume that $N(t)$ follows a Poisson process with master equation

$$\dot{P}(N) = -W(N+\bar{N})P(N) + W(N+1)P(N+1) + W\bar{N}P(N-1), \tag{4.19}$$

where $\bar{N}$ is the average number of particles on the resonator and W is the desorption rate per particle. The standard frequency deviation is $\Delta = \sqrt{\bar{N}}\gamma$. The desorption rate is given by the Kramer's formula $W \simeq \bar{\omega}\exp(-E_b/k_BT)$, where $\bar{\omega}$ is the attempt frequency, E_b is the binding energy between the particle and the resonator surface [73]. In the stationary regime, the Poisson process describes a balance between a flux of particles impinging on the resonator and a flux of particles leaving the resonator.

The equation for the partial susceptibility, $\chi(N;\delta\omega)$, is

$$W[(N+\bar{N})\chi(N;\delta\omega) - \bar{N}\chi(N-1;\delta\omega) - (N+1)\chi(N+1;\delta\omega)] + (\Lambda^* - \gamma N i)\chi(N;\delta\omega) = iP_0(N), \tag{4.20}$$

where $P_0(N) = e^{-\bar{N}}\bar{N}^N/N!$ is the Poisson distribution and $\Lambda = \Gamma + i\delta\omega$.

The oscillator absorption spectrum is depicted in Fig. 4.2 as function of the scaled frequency detuning $\delta\omega/\gamma$. In the limit case of slow frequency noise, the partial susceptibilities, $\chi(\delta\omega; N)$, decouple and acquire the limit form

$$\chi(N;\delta\omega) \approx \frac{iP_0(N)}{\Gamma + \Gamma_N - i(\delta\omega + N\gamma)}, \quad W^{-1} \gg \max\{\Gamma^{-1}, \gamma^{-1}\}, \tag{4.21}$$

where $\Gamma_N = W(\bar{N} + N)$ is the decay rate of the Nth frequency noise state. As depicted in Fig. 4.2, the absorption spectrum exhibits a fine structure with Lorentzian lines centered at $\delta\omega = -\gamma N$ and linewidths $\approx \Gamma + \Gamma_N$.

In the limit case of fast and small frequency jumps the partial susceptibilities acquire the form,

$$\chi(N;\delta\omega) \approx \frac{iP_0(N)}{\Gamma + \gamma^2\bar{N}/W - i(\delta\omega + \bar{N}\gamma)}, \quad W^{-1} \ll \min\{\gamma^{-1}, \Gamma^{-1}\}. \tag{4.22}$$

As depicted in the inset of Fig. 4.2, the partial absorption spectra, Im$\chi(N;\delta\omega)$, interfere so that the total absorption spectrum tends to a Lorentzian line (for small but finite $W^{-1}\Delta$ the spectrum is slightly asymmetric).

4.3.3 Dephasing induced by adsorption, diffusion and desorption of particles in a nanomechanical resonator

Here, I consider dephasing due to adsorption, diffusion and desorption of small particles on a one-dimensional resonator. The frequency noise, $\xi(t)$, varies either continuously when particles diffuse along the resonator or discontinuously when the particles enter or leave the resonator. I discuss first the case of a single particle and then the case of many particles acting independently on the resonator.

Single particle case. The state of the particle is described by its position on the resonator, $x(t) \in [-L/2, L/2]$, and by a discrete variable $\eta(t) = \{0, 1\}$. The resonator length is L. The variable $\eta(t)$ has the value of one (zero) when the particle is (is not) on the nanoresonator. The frequency noise $\xi(t)$ is given by,

$$\xi(t) = -\nu\eta(t)\phi^2(x(t)), \tag{4.23}$$

where $\phi(x)$ is the mode shape, $\nu = m\omega_0/2M$, m is the analyte mass, $M = \int dx\, \rho_0\phi(x)^2$ is the mode effective mass and ρ_0 is the bare resonator mass density.

The transition probability matrix $\hat{W}(x, \eta; x', \eta')$, cf. Eq. (4.6), for the frequency noise process, $\xi(t)$, is defined by

$$\begin{aligned} \partial_t p_{\eta=1}(x,t) &= -\Gamma_o(x)p_1(x,t) + \Gamma_i(x)f(x)p_0(t) + \hat{L}_D(x)p_1(x,t), \\ \partial_t p_{\eta=0}(t) &= \int_{-L/2}^{L/2} dx\, [\Gamma_o(x)p_1(x,t) - \Gamma_i(x)f(x)p_0(t)], \end{aligned} \tag{4.24}$$

where $p_1(x,t)$ is the probability density that the particle is at position x at the instant t. Similarly, $p_0(t)$ is the probability that the particle is not on the nanoresonator at the instant t. The incoming flux distribution per particle is $f(x)$, which is normalized as $\int dx\, f(x) = 1$, and $\Gamma_{i(o)}(x)$ is the probability per unit of time that the particle is adsorbed (desorbed) at the position x. The operator $\hat{L}_D(x)$ describes diffusion of an overdamped particle, cf. Eq. (4.15),

$$\hat{L}_D p_1(x,t) = \partial_x(U'(x)p_1)/\kappa m + D\partial_x^2 p_1, \tag{4.25}$$

where κ and D are the particle friction and diffusion coefficients, respectively, and $U(x)$ is a potential acting on the particle. Equation (4.25) does not consider the effect of inertia trapping discussed in Ref. [74] and in chapter 5. I also assume reflecting boundary conditions: $U'(x)p_1(x,t)/\kappa m + D\partial_x p_1(x,t) = 0$ at $x = \pm L/2$. Note that Eq. (4.24) can be extended to include other subsystems. For instance, the substrate may be considered as a new subsystem which exchanges particles with the resonator subsystem through the clamping regions. In this case additional particle exchange rates, $\Gamma_{i/o}(x = \pm L/2)$, need to be provided.

Below, I consider the nanoresonator fundamental flexural mode with shape

$$\phi(x) = \sqrt{2}\cos(\pi x/L).$$

This mode shape corresponds to the vibrational fundamental mode of a string. Here, it is used as an approximation to the fundamental flexural mode of a doubly clamped nanobeam near the antinode. The particle may be adsorbed at any point on the resonator with equal probability; i.e., $f(x) = 1/L$ in Eq. (4.24). Also, the adsorbed particle freely diffuses along the resonator.

The susceptibility $\chi(\delta\omega)$ is given by the solution of Eq. (4.12) with $\hat{W}$ defined by the master equation (4.24), whose stationary solution is $p_{0,st} = \Gamma_o/(\Gamma_i + \Gamma_o)$ and $p_{1,st}(x) = (1/L) \times \Gamma_i/(\Gamma_i + \Gamma_o)$. The total susceptibility, $\chi(\delta\omega)$, is equal to the sum of the partial susceptibilities $\chi_0(\delta\omega)$ (no particle on resonator) and $\chi_1(x;\delta\omega)$ (particle at position x),

$$\chi(\delta\omega) = \chi_0(\delta\omega) + \int_{-L/2}^{L/2} dx\, \chi_1(x;\delta\omega). \tag{4.26}$$

The partial susceptibilities satisfy the equations

$$\begin{aligned} \left[\Lambda^* - i\nu\phi^2(x) + \Gamma_o - D\partial_x^2\right]\chi_1(x;\delta\omega) - \Gamma_i f(x)\chi_0(\delta\omega) &= ip_{1,st}(x), \\ \left(\Lambda^* + \Gamma_i\right)\chi_0(\delta\omega) - \Gamma_o \int dx\, \chi_1(x;\delta\omega) &= ip_{0,st}, \end{aligned} \tag{4.27}$$

where $\Lambda^* = \Gamma - i\delta\omega$. The analytical solution for the above equation can be obtained by writing the partial susceptibility $\chi_1(x;\delta\omega)$ as

$$\chi_1(x;\delta\omega) = \sum_{k\geq 0} A_k \cos(2\pi k x/L).$$

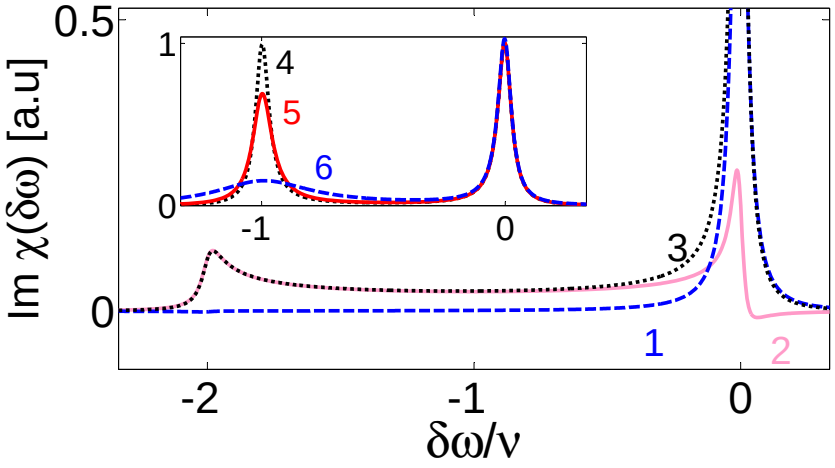

Figure 4.3: Oscillator absorption spectrum, Im$\chi(\delta\omega)$, for the fundamental mode of a doubly clamped resonator with a particle attaching, diffusing and detaching from arbitrary points on the resonator. Curves 1 (dashed) and 2 (solid) depict the partial absorption spectra Im$\chi_0(\delta\omega)$ and Im$\int dx\, \chi_1(\delta\omega, x)$, corresponding to zero and one particle on the resonator, respectively, and curve 3 (dotted) depicts Im$\chi(\delta\omega)$ for the case of nondiffusing particles ($D = 0$). **Inset:** Curve 4 (dotted) depicts Im$\chi(\delta\omega)$ for the limit case of infinitely fast diffusing particles (telegraph noise) and curves 5 and 6 depict Im$\chi(\delta\omega)$ for diffusion coefficients $D = 25\Gamma_o L^2$ and $D = 2\Gamma_o L^2$. Adsorption and desorption rates are $\Gamma_i = \Gamma_o = \nu/30$ and 2ν is maximum frequency shift of a particle landing at center of the resonator. The oscillator damping rate is $\Gamma = 0$.

The coefficients A_k satisfy a difference equation system which can be solved in terms of continued fractions and then I obtain

$$\begin{aligned}\int_{-L/2}^{L/2} dx\, \chi_1(x;\delta\omega) &= \frac{L\cdot ip_{1,st.} + i\Gamma_i p_{0,st.}/\big(\Gamma+\Gamma_i - i\delta\omega\big)}{R(D,\delta\omega) - \Gamma_i\Gamma_o/\big(\Gamma+\Gamma_i-i\delta\omega\big)},\\ \chi_0(\delta\omega) &= \frac{\Gamma_o\int dx\,\chi_1(x;\delta\omega) + ip_{0,\,st.}}{\Gamma+\Gamma_i-i\delta\omega},\end{aligned} \tag{4.28}$$

where R is given by

$$R(D,\delta\omega) = \Theta(0) + \cfrac{\nu^2/2}{\Theta(1) + \cfrac{\nu^2/4}{\Theta(2) + \cfrac{\nu^2/4}{\ddots}}}, \tag{4.29}$$

and $\Theta(n) = \Gamma+\Gamma_o - i(\delta\omega+\nu) + n^2\tau_D^{-1}$, where $\tau_D = D^{-1}(L/2\pi)^2$ is the frequency noise correlation time due to only diffusion, cf. section 4.3.1.

Equations (4.26) and (4.28) are the solution for the susceptibility. In particular, it contains the cases of single particle diffusion (cf. section 4.3.1) and

dephasing due to a two-state frequency noise process, discussed in the celebrated papers by Anderson [75] and Kubo and Tomita [76,77].

Figure 4.3 depicts the results for the oscillator absorption spectrum, $\mathrm{Im}\chi(\delta\omega)$, for the limit cases of slow ($\tau_D \to \infty$) and fast ($\tau_D \to 0$) diffusing particles along the resonator, and for comparatively small adsorption and desorption rates: $\Gamma_i, \Gamma_o, \Gamma \ll \nu$.

In the limit case of slow diffusion ($\tau_D \to \infty$) and finite $\Gamma_{i,o}$, the absorption spectrum line is similar to the one depicted in Fig. 4.1 with some distinct features; namely, a pronounced peak at $\delta\omega = 0$ and no divergencies at the edges of the frequency noise range when $\Gamma \to 0^+$ and $\tau_D \to \infty$, cf. Eq. (4.17). These features can be understood in terms of the partial susceptibilities. The pronounced peak in the absorption line at $\delta\omega = 0$ is due to the contribution of the partial susceptibility corresponding to no particle on the resonator, $\mathrm{Im}\chi_0(\delta\omega)$. This peak is approximately Lorentzian with a half linewidth $\approx \Gamma + \Gamma_i$ and height $\propto p_{0,st} = \Gamma_o/(\Gamma_o + \Gamma_i)$. The departure from the Lorentzian shape is caused by coupling with the partial susceptibilities corresponding to a particle being at position x, $\chi_1(x; \delta\omega \approx 0)$. For the frequency range $\delta\omega < -(\Gamma + \Gamma_i)$, the absorption spectrum is given mainly by the contribution $\chi_1(x; \delta\omega)$. The latter has a form similar to the one found in section 4.3.1. In particular, for $\delta\omega \approx -2\nu$ and $\Gamma \to 0+$, the total susceptibility is approximately given by

$$\begin{aligned} \chi(\delta\omega) &\approx \int dx\, \chi_1(x;\delta\omega) \approx \int dx\, \frac{i p_{1,st}(x)}{\Gamma_o - i(\delta\omega + \nu\phi(x)^2)} \\ &= \frac{iLp_{1,st}}{\sqrt{\big(\Gamma_o - i\delta\omega\big)\big(\Gamma_o - i(\delta\omega + 2\nu)\big)}}, \quad \tau_D \to \infty, \Gamma \to 0^+. \end{aligned} \tag{4.30}$$

Note that the susceptibility does not diverge at $\delta\omega = -2\nu$. The above results agrees with Eq. (4.17) if we set the desorption rate to zero, $\Gamma_o = 0$.

The inset of Fig. 4.3 depicts the limit case of fast diffusing particles ($\tau_D \to 0$) again for small but finite adsorption and desorption rates: $\Gamma_{i,o} \ll \nu$. The absorption spectrum line is approximately given by two Lorentzian lines centered at $\delta\omega = 0$ and $\delta\omega = -\langle\nu\phi(x)^2\rangle$, where the average is performed with the stationary distribution $p_{1,st}(x)$. The heights and half linewidths of these Lorentzians are approximately equal to $p_{0,st}/(\Gamma_i+\Gamma)$, $p_{1,st}L/(\Gamma_o+\Gamma)$ and $\Gamma+\Gamma_i$, $\Gamma + \Gamma_o$; respectively. This corresponds to the results obtained previously for dephasing of an oscillator subject to telegraph-noise [70,75–77]. The effect of diffusion is to broaden the Lorentzian centered at $\delta\omega = -\nu$ by an amount $\approx \nu^2 L^2/8\pi^2 D$. As the particle diffusion gets slower (τ_D increases), this Lorentzian gets broader and it eventually loses its Lorentzian form and it acquires the shape given by Eq. (4.30). The Lorentzian line centered at $\delta\omega = 0$ is not affected by diffusion.

The stationary values of the (scaled) moments of the complex amplitude

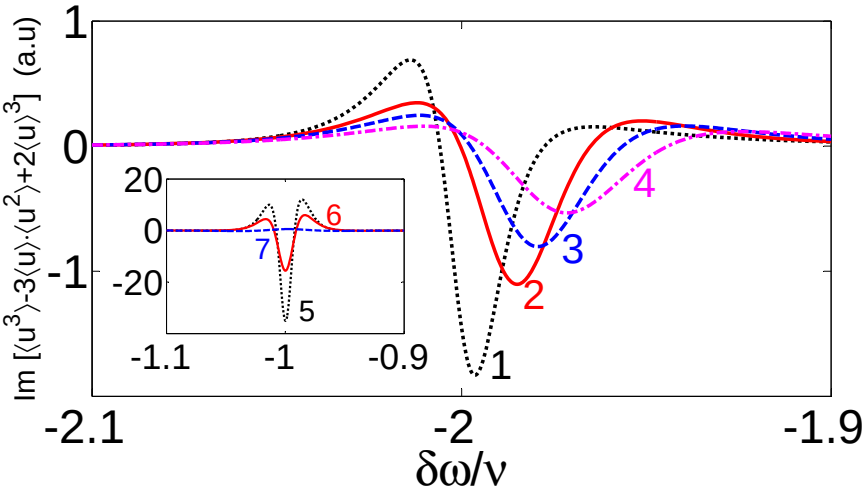

Figure 4.4: Effect of diffusion on the third cumulant κ_3 of the complex vibrational amplitude $u(t)$. Curve 1 (dotted) depicts the limit case of nondiffusing particles. Curves 2 (solid), 3 (dashed) and 4 (dash-dotted) depict the results for particles with diffusion coefficients $D = 10^{-3} \cdot \Gamma_o L^2, 2 \cdot 10^{-3} \Gamma_o L^2$ and $4 \cdot 10^{-3} \Gamma_o L^2$, respectively. **Inset**: Curve 5 (dotted) depicts the limit case of infinitely fast diffusing particles (telegraph noise). Curves 6 (solid) and 7 (dashed) depict the results for $D = 250 \Gamma_o L^2$ and $D = 20 \Gamma_o L^2$, respectively. Other parameters: $\Gamma_i = \Gamma_o = \nu/30$ and $\Gamma = 0$.

$u(t)$, $\chi^{(n)}(\delta\omega)$, are given by

$$\begin{aligned} \chi^{(n)}(\delta\omega) &\equiv \left(\frac{2M\omega_F}{F}\right)^n \langle u^n(t)\rangle_{st} \\ &= \left(\frac{2M\omega_F}{F}\right)^n \sum_{\xi} \int du\, du^*\; u^n P_{st}(u, u^*, \xi), \end{aligned} \tag{4.31}$$

where $P_{st}(u, u^*, \xi)$ is the stationary solution of Eq. (4.7).

From Eq. (4.31), it follows that the scaled stationary values of the higher order moments of $u(t)$ can be expressed in terms of the scaled partial moments,

$$\chi^{(n)}(\xi; \delta\omega) = \left(\frac{2M\omega_F}{F}\right)^n \int du\, du^*\; u^n P_{st.}(u, u^*, \xi). \tag{4.32}$$

The scaled partial moments $\chi^{(n)}(\xi; \delta\omega)$ are complex quantities and they satisfy the following coupled equations, cf. Eq. (4.7), [72,78]

$$\hat{W}\chi^{(n)}(\xi; \delta\omega) - n\big(\Lambda - i\xi\big)\chi^{(n)}(\xi; \delta\omega) = ni\chi^{(n-1)}(\xi; \delta\omega), \tag{4.33}$$

where $\Lambda = \Gamma + i\delta\omega$, $\tilde{\chi}^{(0)}(\xi; \delta\omega) = p_{st}(\xi)$ and $p_{st}(\xi)$ is the stationary distribution of Eq. (4.6). In particular, for the type of frequency noise considered in this

section, the equations for the coupled scaled partial moments $\chi_1^{(n)}(x;\delta\omega)$ and $\chi_0^{(n)}(\delta\omega)$ are

$$\begin{aligned}\big[-n(\Lambda+i\nu\phi^2(x))-\Gamma_o+D\partial_x^2\big]\chi_1^{(n)}(x;\delta\omega)+\Gamma_i f(x)\chi_0^{(n)}(\delta\omega) &= ni\chi_1^{(n-1)}(x;\delta\omega),\\ -\big(n\Lambda+\Gamma_i\big)\chi_0^{(n)}(\delta\omega)+\Gamma_o\int dx\,\chi_1^{(n)}(x;\delta\omega) &= ni\chi_0^{(n-1)}(\delta\omega).\end{aligned} \tag{4.34}$$

Higher-order moments of $u(t)$ are calculated by solving numerically the coupled system (4.33). Figure 4.4 depicts the third cumulant $\kappa_3 = \langle u^3\rangle - 2\langle u\rangle\cdot\langle u^2\rangle + 2\langle u\rangle^3$ for both limit cases of fast and slow diffusing particles. The magnitude and shape of the higher order moments, as function of the scaled frequency detuning $\delta\omega/\nu$, depend on the parameters that define the dephasing process (i.e., diffusion coefficient, adsorption and desorption rates) and these dependencies are more significant for higher-order moments and cumulants of $u(t)$. In practice, their measurement may provide enough information to characterize the dephasing process based on a frequency noise model such as the one discussed in this section.

Many particles case. Now I consider the problem of how to calculate the susceptibility when many particles act on the resonator. This problem can in general be solved in terms of partial susceptibilities with an appropriate master equation for the frequency noise. However, the problem simplifies when the particles act independently on the resonator. Also, assuming that the particles have identical parameters (mass, diffusion coefficient, adsorption and desorption rates), the total frequency noise is equal to a sum of independent and identical processes $\xi_i(t)$, which are realizations of the one-particle process (4.23),

$$\xi(t) = \sum_{i=1}^{N}\xi_i(t), \tag{4.35}$$

where N is the total number of particles in the system (in or out of the resonator).

Particles can be either in the resonator or outside of the resonator. For the process (4.35), the number of particles on the resonator $n(t)$ evolves according to a Bernoulli process with master equation

$$\dot{P}_n = -\big[\Gamma_o n+\Gamma_i(N-n)\big]P_n+(n+1)\Gamma_o P_{n+1}+\Gamma_i\big(N-(n-1)\big)P_{n-1}, \tag{4.36}$$

where $\Gamma_{i(o)}$ is the adsorption (desorption) rate per particle and $\bar{N} = N\Gamma_i/(\Gamma_i+\Gamma_o)$ is the average number of particles on the resonator. For $\bar{N}\ll N$ and $\Gamma_i = (\bar{N}/N)\Gamma_o \ll \Gamma_o$, the stationary distribution of Eq. (4.36) becomes independent of total number of particles in the system, N, and it tends to the Poisson distribution.

The linear differential equation (4.4) can be formally solved for $u^*(t)$ (for a given realization of $\xi(t)$) to obtain the following result for the susceptibility

$$\chi(\delta\omega) = i \int_{-\infty}^{0} dt\, e^{\Lambda^* t} g_\xi(t), \tag{4.37}$$

where $\Lambda^* = \Gamma - i\delta\omega$ and $g_\xi(t) \equiv \left\langle \exp\left(i \int_0^t dt_1 \xi(t_1)\right)\right\rangle_{\xi(t)}$. For the frequency noise, $\xi(t)$, given as a sum of independent processes $\xi_i(t)$,

$$g_\xi(t) = \prod_{i=1}^{N} \langle e^{i \int_0^t dt_1 \xi_i(t_1)} \rangle_{\xi_i(t)}, \tag{4.38}$$

and for identical processes $g_\xi(t) = g^N(t)$, where $g(t) \equiv \left\langle \exp\left(i \int_0^t dt_1 \xi_i(t_1)\right)\right\rangle_{\xi_i(t)}$. Thus, for identical and independent processes, $\xi_i(t)$, the oscillator susceptibility is

$$\chi(\delta\omega) = i \int_{-\infty}^{0} dt\, e^{\Lambda^* t} \cdot g^N(t). \tag{4.39}$$

The above equation suggests a solution for the partial susceptibilities (for single particle) in the form

$$\chi_1(x;\delta\omega) = \int_{-\infty}^{0} dt\, e^{\Lambda^* t} \tilde{\chi}_1(x,t), \quad \chi_0(\delta\omega) = \int_{-\infty}^{0} dt\, e^{\Lambda^* t} \tilde{\chi}_0(t). \tag{4.40}$$

Using Eq. (4.27), the equations for the time-dependent partial susceptibilities, $\tilde{\chi}_1(x,t)$ and $\tilde{\chi}_0(t)$, are

$$\begin{aligned} \partial_t \tilde{\chi}_1(x,t) &= \left[\Gamma_o - i\nu\phi(x)^2 - D\partial_x^2\right]\tilde{\chi}_1(x,t) - \Gamma_i f(x)\tilde{\chi}_0(t), \\ \partial_t \tilde{\chi}_0(t) &= \Gamma_i \tilde{\chi}_0(t) - \Gamma_o \int dx\, \tilde{\chi}_1(x,t), \end{aligned} \tag{4.41}$$

with initial conditions $\tilde{\chi}_1(x,0) = ip_{1st}(x) = i(1/L)\Gamma_i/(\Gamma_i + \Gamma_o)$ and $\tilde{\chi}_0(0) = ip_{0st} = i\Gamma_o/(\Gamma_o + \Gamma_i)$, and reflecting boundary conditions: $\partial_x \tilde{\chi}(x = \pm L/2, t) = 0$. The frequency-noise-dependent function $g(t)$ is equal to

$$g(t) = \int dx\, \tilde{\chi}_1(x,t) + \tilde{\chi}_0(t). \tag{4.42}$$

The solution to the problem for many identical particles acting independently on the resonator is then given in terms of the single-particle problem (4.41) and Eqs. (4.39) and (4.42).

Figure 4.5 shows the oscillator susceptibility function $\chi(\delta\omega)$ for an average number of adsorbed particles $\bar{N} = 3$. The limit case of infinitely fast diffusing particles ($\tau_D \to 0$) corresponds to the results obtained previously for discrete frequency jumps with a stationary Poisson distribution [72]. In particular, for $\Gamma_o, \Gamma \ll \nu$, the oscillator susceptibility exhibits a fine structure

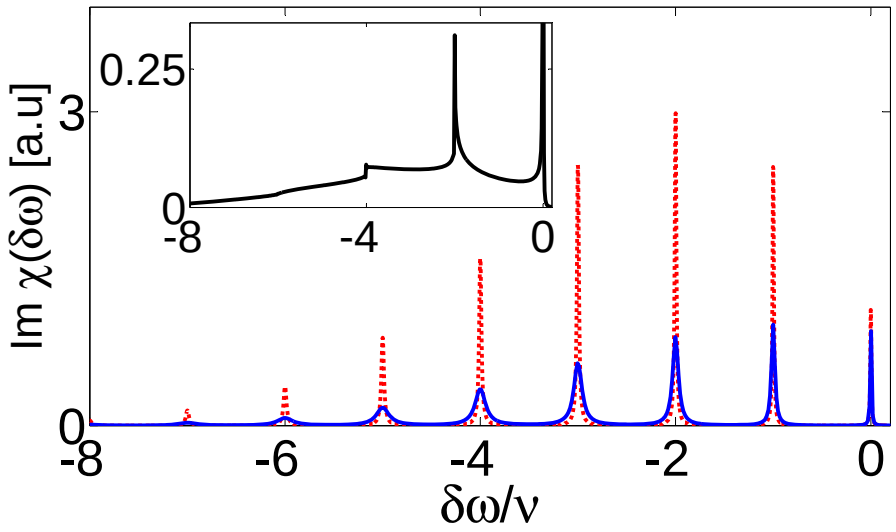

Figure 4.5: Oscillator absorption spectrum $\mathrm{Im}\chi(\delta\omega)$ for an average number of adsorbed particles $\bar{N} = 3$. The dotted curve depicts the results for the limit case of infinitely fast diffusing particles ($D \to \infty$). The solid line depicts the result for diffusion coefficient $D = 500\Gamma_o L^2$. **Inset:** Limit case of slowly diffusing particles ($D \to 0$). Other parameters: $N = 10^4$, $\Gamma_o = 0.002\nu$, $\Gamma_i = (N_o/N)\Gamma_o$ and $\Gamma = 0$.

as shown in Fig. 4.5 (dotted curve). Here, the total susceptibility is formed by Lorentzians centered at frequencies $\delta\omega = -j\nu$ ($j = 0, 1, \cdots$) with half linewidths $\Gamma + (j + N_0)\Gamma_o$ and heights proportional to $P_j = \exp(-\bar{N})\bar{N}^j/j!$ (Poisson distribution). In the case of particles with finite diffusion coefficients, D, the half linewidths of these Lorentzians is increased by an amount $\approx j\nu^2 L^2/(8\pi^2 D)$, cf. Fig. 4.5 (solid curve). The inset depicts the limit case of slowly diffusing particles ($\tau_D \to \infty$). Here, we observe that the absorption spectrum line, $\mathrm{Im}\chi(\delta\omega)$, exhibits sharp peaks. These peaks are not Lorentzians and they become sharper as Γ_o decreases. They also appeared for a single particle acting on the nanoresonator, cf. Eq. (4.30). The above results agree with Monte Carlo simulations [79,80].

4.4 The fluctuation-dissipation theorem in the presence of dephasing

The aim of this section is to relate the results for the oscillator susceptibility, given by the oscillator response to a weak driving force, and the oscillator power spectrum, determined by the oscillator response to a thermal additive white noise force. Under certain conditions, the latter are directly propor-

tional, cf. Eq. 4.43. I point out that the results for the susceptibility are not affected by a white source of additive noise if Eqs. (4.46) and (4.47) hold. I also discuss the conditions that allow us to take the averages over the thermal additive noise and frequency noise independently, cf. Eq. (4.55).

The fluctuation-dissipation theorem states that the oscillator absorption spectrum, $\mathrm{Im}\chi(\delta\omega)$, is proportional to the oscillator power spectrum, $\mathrm{Re}\mathcal{Q}(\delta\omega)$,

$$\mathrm{Im}\chi(\delta\omega) = (2\pi M\omega_0^2/k_BT)\mathrm{Re}\mathcal{Q}(\delta\omega), \tag{4.43}$$

where the power spectrum is defined by [4],

$$\mathrm{Re}\mathcal{Q}(\delta\omega) \equiv \pi^{-1}\mathrm{Re}\int_0^\infty dt\, e^{i\omega t}\langle q(t)q(0)\rangle_{\xi(t),f_T(t);F=0}, \tag{4.44}$$

and the average is performed over the thermal additive noise, $f_T(t)$, and the frequency noise, $\xi(t)$, with zero driving field, $F = 0$ in Eq. (4.1).

It turns out that the fluctuation-dissipation relation holds if the joint stationary probability density of the undriven system ($F = 0$) can be written as

$$\rho_{st}(u, u^*, \xi) = \rho_B(|u|^2)p_{st}(\xi), \tag{4.45}$$

where $\rho_B(|u|^2) \propto \exp(-C_T|u|^2)$ is the Boltzmann distribution with $C_T^{-1} \propto k_BT$, and $p_{st}(\xi)$ is the frequency noise stationary distribution, cf. Eq. (4.6). In particular, the fluctuation-dissipation theorem does not hold when the frequency noise depends on the oscillator state (backaction).

The Einstein-Fokker-Planck (EFP) equation for the joint distribution, ρ, is

$$\partial_t\rho(u, u^*, \xi, t) = \mathcal{L}[\rho] - \frac{F}{2iM\omega_F}\big[e^{it\delta\omega}\partial_u\rho - e^{-it\delta\omega}\partial_{u^*}\rho\big], \tag{4.46}$$

where $\mathcal{L}[\rho]$ is given by

$$\mathcal{L}[\rho] = \partial_u(K(|u|^2, \xi)u\rho) + \partial_{u^*}(K^*(|u|^2, \xi)u^*\rho) + \frac{k_BT}{M\omega_0^2}\partial^2_{u,u^*}\big(\Gamma_{nl}(|u|^2, \xi)\rho\big) + \hat{W}\rho. \tag{4.47}$$

Above, the slow dynamical variables $u(t)$ and $u^*(t)$ are defined by

$$\begin{aligned} q(t) &= u(t)e^{i\omega_0t} + u^*(t)e^{-i\omega_0t} \\ \dot{q}(t) &= i\omega_0\big[u(t)e^{i\omega_0t} - u^*(t)e^{-i\omega_0t}\big]. \end{aligned} \tag{4.48}$$

Note that in this section I use the bare eigenfrequency ω_0 as the reference frequency for the rotating wave approximation (RWA). The functions K and Γ_{nl} can only depend on the slow variable $|u|^2$; u and u^* can not appear separately because the corresponding terms (prior to averaging over the period $2\pi/\omega_0$ in the RWA) are proportional to $\exp(\pm i\omega_0t)$ which are averaged to zero in the RWA. Similarly, the operator $\hat{W}$, defining the frequency noise process, can depend only on $|u|^2$.

If we neglect $\langle u(t)u(0)\rangle_{\xi(t),f_T(t);F=0}$ (weakly nonlinear oscillator weakly coupled to the thermal bath) and also fast oscillating terms with frequency $2\omega_0$, the power spectrum can be written in the form

$$\mathrm{Re}\mathcal{Q}(\delta\omega) \approx \pi^{-1}\mathrm{Re}\int_0^\infty dt\, e^{it\delta\omega}\langle u^*(t)u(0)\rangle_{\xi(t),f_T(t);F=0}, \tag{4.49}$$

where

$$\langle u^*(t)u(0)\rangle_{\xi(t),f_T(t);F=0} = \sum_\xi \int dudu^*\ u^* e^{\mathcal{L}t} u\rho_{st}(u,u^*,\xi), \qquad \mathcal{L}[\rho_{st}] = 0. \tag{4.50}$$

Now, I find an expression for the oscillator absorption spectrum, $\mathrm{Im}\chi(\delta\omega)$. To first order in F, the stationary solution of the EFP equation is

$$\rho(t) \approx \left(\frac{F}{2iM\omega_F}\right) e^{-it\delta\omega}\int_0^\infty dt_1\, e^{it_1\delta\omega} e^{\mathcal{L}t_1}\partial_{u^*}\rho_{st} + \text{c.c.} \tag{4.51}$$

The scaled oscillator susceptibility is $\chi(\delta\omega) = (2M\omega_F/F)\exp(i\delta\omega t)\langle u^*\rangle_{\rho(t)}$,

$$\begin{aligned}\chi(\delta\omega) \approx -i\int_0^\infty dt_1 e^{it_1\delta\omega}\sum_\xi\int dudu^*\ u^* e^{\mathcal{L}t_1}\partial_{u^*}\rho_{st} \\ + ie^{2it\delta\omega}\int_0^\infty dt_1 e^{-it_1\delta\omega}\sum_\xi\int dudu^*\ u^* e^{\mathcal{L}t_1}\partial_u\rho_{st},\end{aligned} \tag{4.52}$$

the second term at the right hand side of Eq. (4.51) is a spurious term which should disappear for the fluctuation-dissipation theorem to hold. The absorption spectrum is equal to

$$\mathrm{Im}\chi(\delta\omega) \approx -\mathrm{Re}\int_0^\infty dt_1 e^{it_1\delta\omega}\sum_\xi\int dudu^*\ u^* e^{\mathcal{L}t_1}\partial_{u^*}\rho_{eq} + \text{spurious term}, \tag{4.53}$$

The expressions for the oscillator power spectrum [Eqs. (4.49) and (4.50)] and for the absorption spectrum [Eqs. (4.52) and (4.53)] suggest that the condition for the fluctuation-dissipation relation to hold is: $\partial_{u^*}\rho_{st} = -C_T u\rho_{st}$ with $C_T = 2M\omega_0^2/k_BT$. This implies that $\rho_{st}(u,u^*,\xi) = (1/Z)p_{st}(\xi)\exp(-C_T|u|^2)$ where Z is a normalization constant. Note that this form for ρ_{st} cancels the spurious term of Eq. (4.53). Moreover, $\rho_{st}(|u|^2,\xi)$ must satisfy that $\mathcal{L}[\rho_{st}] = 0$; this requires that $\hat{W}$ should not dependent on $|u|^2$ (no backaction) and

$$\mathrm{Re}K(r,\xi) - \Gamma_{nl}(r,\xi) + \frac{k_BT}{2M\omega_0^2}\partial_r\Gamma_{nl} = 0. \tag{4.54}$$

4.5 Dephasing of a nonlinear oscillator

Here, I discuss under which conditions the averaging over the thermal additive noise, $f_T(t)$, and the frequency noise, $\xi(t)$, can be performed independently. If this is possible, then the oscillator susceptibility can be written in a convolution form,

$$\chi(\delta\omega) = \int d\omega_1 \; \chi_{osc}(\omega_1)\chi_\xi(\delta\omega - \omega_1), \tag{4.55}$$

where $\chi_{osc}(\omega)$ is the oscillator susceptibility in the absence of frequency noise and $\chi_\xi(\omega)$ is a dephasing dependent quantity equal to

$$\chi_\xi(\omega) = \int_0^\infty dt \, e^{-i\omega t} \langle e^{-i\int_0^t dt_1 \, \xi(t_1)} \rangle_{\xi(t)}. \tag{4.56}$$

A necessary condition for the validity of Eq. (4.55) is that the fluctuation-dissipation relation holds. That is, in the absence of driving, the joint probability density of the system is given by Eq. (4.45). The sufficient conditions are discussed in this section.

For Eq. (4.55) to hold, it is also required that the EFP operator, $\mathcal{L}$, can be separated as $\mathcal{L}(\cdot) = \mathcal{L}_{osc}(\cdot) - i\xi\partial_u(u(\cdot)) + i\xi\partial_{u^*}(u^*(\cdot)) + \hat{W}$, where $\mathcal{L}_{osc}$ contains only nondephasing terms. This separation is possible if $\partial_\xi \mathrm{Re}K = \partial_\xi \Gamma_{nl} = 0$ and $\partial^2_{r,\xi}\mathrm{Im}K = 0$, where $r = |u|^2$. That is, the vibrational frequency is modulated as $\xi + \tilde{K}(r)$, where the first term is due to the frequency noise and the second term is due to an intrinsic nonlinearity (e.g., Duffing nonlinearity). From Eq. (4.52), the susceptibility is given by

$$\begin{aligned} \chi(\delta\omega) &\approx iC_T \int_0^\infty dt \, e^{it\delta\omega} \sum_\xi \int dudu^* \, u^* e^{\mathcal{L}t} u\rho_B(r)p_{st}(\xi) \\ &= iC_T \int_0^\infty dt \, e^{it\delta\omega} \int dudu^* \, u^* e^{t\mathcal{L}_{osc}} u\rho_B(r) \cdot \sum_\xi \bar{p}_\xi(t), \end{aligned} \tag{4.57}$$

where $\bar{p}_\xi(t)$ satisfies

$$\partial_t \bar{p}_\xi(t) = \hat{W}\bar{p}_\xi(t) - i\xi\bar{p}_\xi(t), \tag{4.58}$$

and $\bar{p}_\xi(0) = p_{st}(\xi)$. Equation (4.57) can also be written as [75]

$$\chi(\delta\omega) \approx i\int_0^\infty dt \, e^{it\delta\omega} \frac{\langle u^*(t)u(0)\rangle_{osc}}{\langle |u(0)|^2\rangle_{osc}} \cdot \left\langle e^{-i\int_0^t dt_1 \, \xi(t_1)} \right\rangle_{\xi(t)}. \tag{4.59}$$

Hence, the oscillator susceptibility can be determined in terms of the correlator $\langle u^*(t)u(0)\rangle_{osc}$, which is determined only by the intrinsic nonlinearity of the system, and the dephasing-dependent factor: $\left\langle \exp\left(-i\int_0^t dt_1 \, \xi(t_1)\right)\right\rangle_{\xi(t)}$. In other words, if the fluctuation-dissipation theorem holds and also $\partial_\xi \mathrm{Re}K = \partial_\xi \Gamma_{nl} = 0$ and $\partial^2_{r,\xi}\mathrm{Im}K = 0$, then it is possible to take the thermal and frequency noise averages separately. The convolution form (4.55) for the susceptibility follows from Eq. (4.59) and a well-known property of Fourier transform.

CHAPTER 5

Diffusion-induced bistability of driven nanomechanical resonators

In the previous chapter I discussed decoherence of a vibrational mode of a resonator subject to random mass loading. Here, it was assumed that the motion of the resonator does not affect the frequency noise process (i.e., the motion of the particles, adsorbed onto the resonator, is not affected by the resonator dynamics). It was shown that fluctuations in the eigenfrequency can broaden and even change the shape of the oscillator absorption line from the standard Lorentzian shape (e.g., the oscillator absorption spectrum may develop a fine structure if the eigenfrequency fluctuations are discrete and comparatively slow). However, if the frequency fluctuations are comparatively fast, the effect of the frequency noise is reduced to a simple shift and to a small increase of the linewidth which is proportional to the noise correlation time and to the variance of the frequency noise (motional narrowing limit, cf. Eq. (4.11)).

In this chapter, I consider the possibility that the frequency fluctuations are affected by the motion of the resonator (backaction). For the problem of Brownian particles diffusing along the resonator, backaction means that the particles are influenced by an inertial force which drives them toward the vibrational antinodes. I show that backaction and dephasing can lead to bistability and rare interstate switching behavior when the particles diffuse comparatively fast along the resonator. The bistability discussed here is different from the one commonly observed in driven nonlinear oscillators subject to a weak source of additive noise [4, 64, 65].

5.1 Trapping of molecules at the antinodes of vibrational modes

The inertia trapping of molecules at the antinodes of vibrational modes of a resonator (e.g., nanobeam) can be understood by looking at the kinetic term of the system Lagrangian,

$$\mathcal{T}_{kin} = \frac{1}{2}\int dx\ \mu(x)\phi^2(x)\dot{q}^2(t), \tag{5.1}$$

where $\mu(x)$ is the mass density of the system and the resonator displacement, due to a mode with shape $\phi(x)$ and amplitude $q(t)$, is $\varphi(x,t) = \phi(x)q(t)$. Below, I consider a one-dimensional resonator with mass density $\mu(x) = M/L + m\sum_{i=1}^{N}\delta(x-x_i)$ where M and L are the bare mass and length of the resonator, respectively, and the mass loading is due to N particles with mass m at positions x_i. I also consider the fundamental vibrational mode with bare resonance frequency ω_0 and mode shape $\phi(x) = 2^{1/2}\cos(\pi x/L)$. This mode is assumed to be underdamped and driven by a force $F\cos(\omega_F t)$. The vibrational amplitude has the form $q(t) = (F/4M\omega_F\Gamma)[u(t)e^{i\omega_F t} + u^*(t)e^{-i\omega_F t}]$, where the scaled complex amplitude $u(t)$ changes over a time scale given by the reciprocal of the mode energy relaxation rate, $\Gamma \ll \omega_F \approx \omega_0$, and

$$u(t) = (2M\Gamma/F)(\omega_F q - i\dot{q})\exp(-i\omega_F t).$$

The kinematic interaction given by Eq. (5.1) is not only responsible for the shift of the mode eigenfrequency, $\Delta\omega_D(\{x_i\})$, which depends on the mass distribution as

$$\Delta\omega_D(\{x_i\}) = -\frac{\omega_0 m}{2M}\sum_{i=0}^{N}\phi^2(x_i), \tag{5.2}$$

but also provides an effective potential, U_{eff}, acting on the diffusing particles:

$$\begin{aligned} U_{eff}(\{x_i\},t) &\approx -\frac{m\langle\dot{q}^2\rangle_{T_F}}{2}\sum_i \phi^2(x_i), \\ &= -m\big(F/4M\Gamma\big)^2|u(t)|^2\sum_i\phi^2(x_i). \end{aligned} \tag{5.3}$$

Above, I assume that the diffusion is slow within the oscillation period $T_F = 2\pi/\omega_F$; i.e., $(DT_F)^{1/2} \ll L$ where D is the diffusion coefficient.

Figure 5.1 depicts the effective potential U_{eff} acting on the diffusing particles. In the absence of diffusion, the particles are driven toward the vibrational antinode.

Inertia trapping has been observed in recent experiments and it has been suggested that this effect could be used to trap diffusing particles along the resonator in mass measurement experiments [20, 24].

Diffusion induced bistability (DIB) of driven resonators results from the competition of two counteracting factors: inertia trapping and diffusion. Inertia trapping tries to confine the particles at the antinode of the fundamental flexural mode. This results in a mass distribution peaked at the center of the nanobeam, $x = 0$, cf. Fig. 5.2 (b). Diffusion opposes to the effect of inertia confinement and favors a uniform mass distribution (assuming reflecting boundary conditions at the nanobeam ends: $x = \pm L/2$), cf. Fig.5.2 (a). Moreover, the mode eigenfrequency depends on the mass distribution according to Eq. (5.2). One condition for DIB is that the vibrational mode, with mass configuration

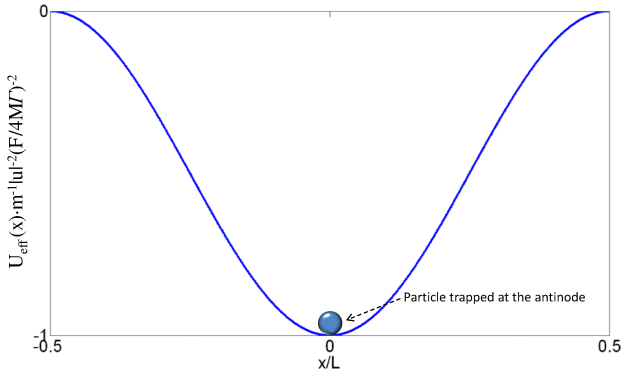

Figure 5.1: Effective potential driving the particles on the resonator to the vibrational antinode of the fundamental flexural mode.

depicted in Fig. 5.2 (b), is driven near resonance and that the resulting oscillation amplitude is sufficiently large: $m\langle\dot{q}^2\rangle_{T_F} \gtrsim k_BT$, where k_BT is the thermal energy. The other condition is that $L \lesssim (D/\Gamma)^{1/2}$; that is, the particles diffuse comparatively fast within the time Γ^{-1}. If these two conditions are satisfied then the configuration depicted in Fig. 5.2 (b) is selfconsistently sustained for a time much longer than Γ^{-1}. Moreover, if the particles are spread over the whole resonator, then the vibrational amplitude is small (because the mode eigenfrequency is larger than the driving frequency) and the confinement is week [$m\langle\dot{q}^2\rangle_{T_F} \ll k_BT$]. Consequently, the configuration depicted in Fig. 5.2 (a) can also be selfconsistently sustained for a time much longer than Γ^{-1}.

5.2 Mean field theory

There are two time scales in the problem. One time scale is the time over which the scaled complex vibrational amplitude, $u(t)$, changes. This time scale is set by the reciprocal of the mode energy relaxation rate, $\tau_{osc} = \Gamma^{-1}$. The other time scale is set by the time $\tau_D \equiv L^2D^{-1}$ for a particle to diffuse a distance equal to the resonator length. Mean field theory applies in the limit: $\theta \equiv \tau_{osc}/\tau_D \to \infty$. In this limit, the particle distribution is given by

$$\rho_a(\{x_i\};t) \approx \prod_i \rho_a(x_i;|u^2(t)|), \tag{5.4}$$

where $\rho_a(x;|u^2|) = Z^{-1}\exp(-U_{eff}(x;|u^2|)/k_BT)$ is the single particle stationary distribution function for a fixed oscillation amplitude, $|u|$, and Z is a normalization constant. Here, I use the Einstein relation: $m\kappa D = k_BT$, where κ is the friction coefficient of the overdamped Brownian particles. In the mean field picture, the effect of the fast diffusing particles is just a frequency shift,

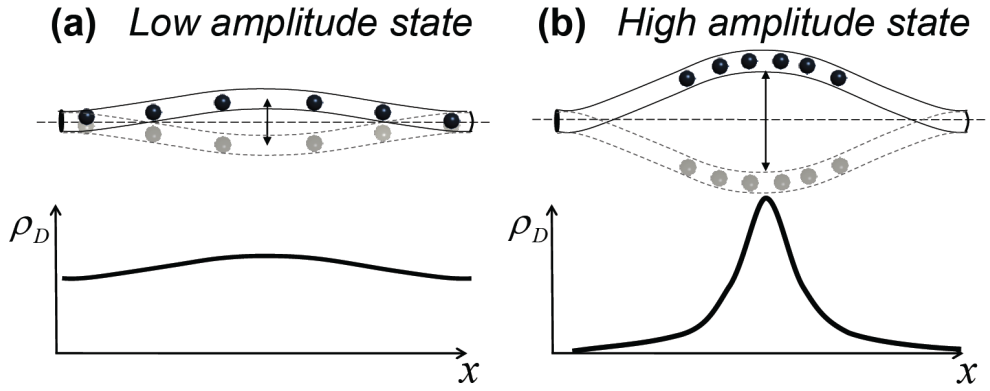

Figure 5.2: Nanobeam resonator with diffusing particles. (a) In the low-amplitude vibrational state, the particle density, $\rho_D(x)$, is almost uniform. (b) In the high-amplitude vibrational state the particles are driven toward the antinode and the distribution has a pronounced maximum there. The eigenfrequency of the mode is determined by the mass distribution. Diffusion induced bistability arises when the resonator is driven by an external field which resonates with the high-amplitude state configuration.

which effectively depends on the vibration amplitude $|u|$,

$$\begin{aligned} \Delta\omega_D(\{x_i\}) &\rightarrow \Delta\omega_D(|u|^2) \equiv \langle \Delta\omega_D(\{x_i\})\rangle_a \\ &= -\frac{\omega_0 m N}{2M}\int dx\ \phi^2(x)\rho_a(x;|u|^2). \end{aligned} \tag{5.5}$$

Thus, after eliminating the fast variables of the problem, we are left with an oscillator which has become effectively nonlinear (the eigenfrequency now depends on $|u|$). The dimensionless equation for $u(t=\tau\Gamma^{-1})$ is given by

$$\frac{du}{d\tau} = -\big[1 + i\big(\Omega + \nu_{00}(|u|^2)\big)\big]u - i, \tag{5.6}$$

where $\Omega = (\omega_F - \omega_0)/\Gamma$ is the scaled frequency detuning, $\tau = t\Gamma$ is the scaled time and $\nu_{00}(|u|^2) = -\Delta\omega_D(|u|^2)/\Gamma > 0$ is the scaled mean of the frequency fluctuations. The above equation determines the amplitude of the stationary solutions, u_{st},

$$|u_{st}^2| = \frac{1}{1 + \big[\Omega + \nu_{00}(|u_{st}^2|)\big]^2}. \tag{5.7}$$

The number of roots of Eq. (5.7) depends on two parameters; namely, $\Omega = (\omega - \omega_F)/\Gamma$ and $\beta_D = (F/4M\Gamma)^2/\kappa D$, where κ is the friction coefficient of the Brownian particles. Using the Einstein relation, $m\kappa D = k_B T$, the latter parameter can be interpreted as the ratio between the maximum kinetic energy

$\sim m(F/4M\Gamma)^2$ that the particle gains at the antinode due to the resonator motion, and the thermal energy k_BT. Thus, β_D measures the relative strength of the forces that lead to confinement with respect to the forces that cause diffusion. Equation (5.7) can have one or three roots. In order to have three roots, it is necessary that $\beta_D > \beta_{min}$ [$\beta_{min} \approx 1$ for $\bar{\nu} \equiv Nm\omega_0/2M\Gamma = 10$], as depicted in Fig. 5.3. Mean field theory predicts the regions in parameter space where bistability may arise. I say "may" because within the mean field picture the deviations of $\Delta\omega_D(\{x_i\})$ from its mean field value $\Delta\omega_D(|\tilde{u}|^2)$ are neglected. I refer to these deviations as fluctuations or nonadiabatic corrections. If the latter are comparatively large, then the stationary distribution of the oscillator subsystem does not exhibit two distinguishable peaks in phase space and also the interstate switching rates can be as large as Γ. Bistability can only arise if the fluctuations are comparatively small such that the oscillator distribution has two distinguishable peaks. This in turn guarantees that the interstate switching to be much smaller than Γ (condition for bistability). Below, I discuss the nature of the nonadiabatic corrections and show that their intensity is $\propto \theta^{-1}$.

5.3 Nonadiabatic corrections to the mean field theory

In this section I consider the nonadiabatic corrections to the mean field theory in the limit of fast diffusing particles, $\theta \equiv \tau_{osc}/\tau_D \gg 1$, where $\tau_{osc} = \Gamma^{-1}$ and $\tau_D = L^2/D$ are the two time scales present in the problem. In this limit, it is clear that the fluctuations have a short correlation time $\sim \tau_D/N \ll \tau_{osc}$ and they can be considered white (noise with zero correlation time). The probability distribution function of the fluctuations, at a given time, does not have to be Gaussian. However, if there is a large number of particles on the resonator, $N \gg 1$, then the fluctuations become Gaussian. This bears on the property of stability of the Gaussian distribution (the distribution of the sum of a large number of random numbers is approximately Gaussian). Thus, the nonadiabatic corrections to the mean field theory for a large number of fast diffusing particles are effectively white Gaussian fluctuations. Then, the dimensionless equations of motion for the oscillator are (in polar coordinates: $u = Re^{i\varphi}$)

$$\begin{aligned} \frac{dR}{d\tau} &= -R - \sin(\varphi), \\ \frac{d\varphi}{d\tau} &= -\big[\Omega + \nu_{00}(R^2)\big] - \frac{\cos(\varphi)}{R} + \mathcal{D}^{1/2}\xi(\tau), \qquad (N \gg 1) \end{aligned} \tag{5.8}$$

where $\xi(\tau)$ is a white and Gaussian noise source with a two-time correlation function equal to $\langle \xi(\tau_1)\xi(\tau_2)\rangle = 2\delta(\tau_1 - \tau_2)$ and $\delta(\cdot)$ is the Dirac function. Above, I have used a dimensionless time $\tau = \Gamma t$ and the relative frequency shift is $\nu_{00}(R^2) \equiv -\Delta\omega_D(|u|^2)/\Gamma$ with $\Delta\omega_D(|u|^2)$ given by Eq. (5.5). The

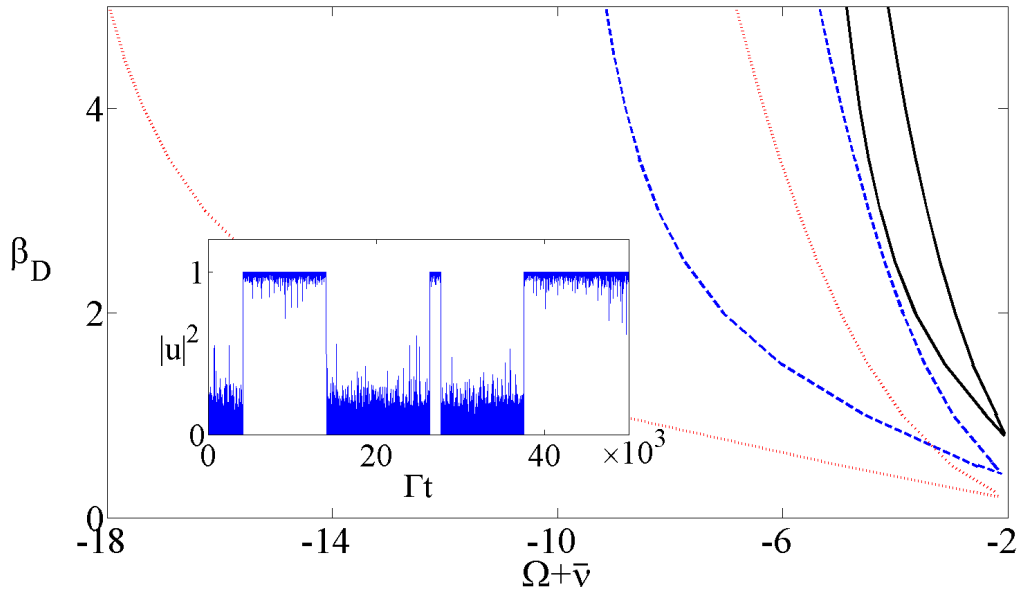

Figure 5.3: Wedge-like regions in parameter space where there are three stationary states (two stable and one unstable) according to the mean field picture, cf. Eq. (5.7). The parameter $\beta_D = (F/4M\Gamma)^2/\kappa D$ is the scaled driving intensity and $\Omega = (\omega - \omega_F)/\Gamma$ is the scaled frequency detuning. The solid, dashed and dotted lines shows the pairs of bifurcation lines for $\bar{\nu} = mN\omega_0/2M\Gamma = 5, 10$, and 20, respectively, and for the mode shape: $\phi(x) = 2^{1/2}\cos(\pi x/L)$. Bistability occurs inside the corresponding wedges. The inset shows a simulated scaled square amplitude of forced vibrations $|u|^2$ as a function of the scaled time Γt for $\theta \equiv \tau_{osc}/\tau_D = D/\Gamma L^2 = 1.01$, $\bar{\nu} = 10$ and $\Omega = -18.95$, and $\beta_D = 5$.

strength of the frequency fluctuations, causing phase diffusion, is given by the parameter $\mathcal{D}$,

$$\mathcal{D} = \int_0^\infty d\tau \left\langle \left[\zeta(\tau) - \langle\zeta(\tau)\rangle_a\right]\zeta(0)\right\rangle_a, \tag{5.9}$$

where $\zeta(\tau) = N^{-1}\sum_{i=1}^{N}\nu(z_i(\tau))$ and $\nu(z) = (\omega_0 mN/2M\Gamma)\phi^2(Lz)$ is the scaled frequency shift due a particle at position $x = Lz$. The average $\langle\cdot\rangle_a$ is calculated over realizations of particle trajectories $z_i(\tau)$, given by Eq. (5.13), with fixed $|u|$. Since the particles are noninteracting (this is only correct if $|u|$ varies slowly within the time scale relevant for diffusion; strictly speaking the particles indirectly interact through the oscillator), the strength of the fluctuations can be written as

$$\mathcal{D} = N^{-1}\int_0^\infty d\tau \left\langle [\nu(z_i(\tau)) - \langle\nu(z_i(\tau))\rangle_a]\nu(z_i(0))\right\rangle_a. \tag{5.10}$$

Below, I consider the case of a single particle and show that the above integral is $\propto D^{-1}$, cf. Eq. (5.21). Thus, the strength of the nonadiabatic corrections for

$N \gg 1$ fast diffusing particles is $\mathcal{D} \sim (ND)^{-1}$.

In the case that there is only one particle on the resonator and $\tau_D \ll \tau_{osc}$, the eigenfrequency fluctuations can be considered white but they are non-Gaussian (this is due to the nonlinear relation between the particle position, x, and the relative frequency shift $\Delta\omega_D(x)/\omega_0 \propto \phi^2(x)$, where $\phi(x)$ is the mode profile). However, I demonstrate that the reduced equation of motion for the oscillator (5.8), where the noise source $\mathcal{D}\xi(\tau)$ is Gaussian and white, can be used to calculate the shape of the oscillator stationary probability density near the stationary points u_{st}, predicted by the mean field theory. I also show that Eq. (5.8) can be used to calculate the the escape rates from the metastable equilibrium state for controlling parameters near the boundary of the wedge-like regions of bistability depicted in Fig. 5.3 (bifurcation points).

The dimensionless equation of motion for the oscillator is

$$\frac{du}{d\tau} = K_r + K_D, \tag{5.11}$$

where

$$K_r = -(1 + i\Omega)u - i, \quad K_D = -iu\nu(z). \tag{5.12}$$

Above, $\Omega = (\omega_F - \omega_0)/\Gamma$ is the scaled frequency detuning and

$$\nu(z) = (m\omega_0/2\Gamma M)\phi^2(Lz)$$

is the scaled frequency shift due a particle at a point $x = Lz$ and $\phi(x)$ is the mode shape. The dimensionless equation of motion for the overdamped Brownian particle is

$$\frac{dz}{d\tau} = -|u^2|\partial_z\Phi(z) + \theta^{1/2}\xi(\tau), \;\; \theta = \tau_{osc}/\tau_D, \tag{5.13}$$

where $\Phi(z) = -(F/4M\Gamma L)^2(\Gamma\kappa)^{-1}\phi^2(Lz)$, κ is the particle friction coefficient, $\tau_{osc} = \Gamma^{-1}$ is the time scale where oscillator state changes and $\tau_D = L^2/D$ is the time for a particle to diffuse a distance equal to L. The noise drive $\xi(t)$ is Gaussian and white with autocorrelation function $\langle\xi(\tau_1)\xi(\tau_2)\rangle = 2\delta(\tau_1 - \tau_2)$. Below, I consider the situation where there are two distinct time scales and θ is the large parameter of the theory. The limit $\theta \gg 1$ also implies that the diffusion length, $l_D = (D/\Gamma)^{1/2}$, over the time τ_{osc} is much larger than the resonator length, L.

The Einstein-Fokker-Planck equation for the probability density of the system, ρ, is

$$\begin{aligned} \partial_\tau\rho(u, u^*, z, \tau) &= -\{\partial_u[(K_r + K_D)\rho] + \text{c.c.}\} + L_z\rho, \\ L_z\rho &= \partial_z[|u|^2\partial_z\Phi(z) + \theta\partial_z]\rho. \end{aligned} \tag{5.14}$$

The boundary conditions are $\rho \to 0$ for $|u| \to \infty$ and $[|u|^2\partial_z\Phi + \theta\partial_z]\rho = 0$ at $z = \pm 1/2$ (reflecting boundary condition). The solution of the above equation

can be sought in the form

$$\rho(u,u^*,z,\tau)=\sum_{\alpha\geq 0}p_\alpha(u,u^*,\tau)\psi_\alpha(z;|u|^2), \tag{5.15}$$

where ψ_α satisfies the eigenvalue problem $L_z\psi_\alpha=-\lambda_\alpha\psi_\alpha$ with boundary conditions $\big[|u|^2\partial_z\Phi+\theta\partial_z\big]\psi_\alpha=0$ at $z=\pm 1/2$. This problem has eigenvalues $\lambda_0=0$ (with ψ_0 as the stationary distribution) and $\lambda_{\alpha>0}\sim\theta\gg 1$. Note that the eigenfunctions, ψ_α, and eigenvalues, λ_α, depend parametrically on $|u|$. Below, I also use the eigenfunctions $\bar\psi_\alpha$ of the adjoint eigenvalue problem: $L_z^\dagger\bar\psi_\alpha=-\lambda_\alpha\bar\psi_\alpha$, where $L_z^\dagger$ is the adjoint operator of L_z and $\bar\psi_\alpha$ satisfies the same boundary conditions as ψ_α. The expansion (5.15) is appropriate in the adiabatic limit $\theta\gg 1$. Substitution of Eq. (5.15) into Eq. (5.14) leads to the following set of equations for p_α,

$$\begin{aligned}\partial_\tau p_\alpha &= \sum_\beta \mathcal{L}_{\alpha\beta}p_\beta,\\ &= -\lambda_\alpha p_\alpha-[\partial_u(K_r p_\alpha)+\text{c.c.}]+\sum_\beta\nu_{\alpha\beta}\partial_\varphi p_\beta-\sum_\beta k_{\alpha\beta}p_\beta,\end{aligned} \tag{5.16}$$

where $\varphi=\ln(u/u^*)/2i$ is the oscillator phase coordinate,

$$\nu_{\alpha\beta}=\int dz\,\bar\psi_\alpha(z)\nu(z)\psi_\beta(z),$$

$k_{\alpha\beta}=\int dz\,\bar\psi_\alpha(K_r\partial_u+\text{c.c.})\psi_\beta$ and, since $\bar\psi_0=1$, $k_{0\alpha}=0$.

Note that the coefficient p_0 evolves in a dimensionless time scale of 1. The other coefficients, $p_{\alpha>0}$, decay to their quasi-stationary values in a dimensionless time $\approx\lambda_\alpha^{-1}\ll 1$. Since we are interested in the dynamics of the system for time scales $\gg\Gamma^{-1}$, we may assume that $\partial_\tau p_\alpha\approx 0$,

$$\partial_\tau p_0=-[\partial_u(K_r p_0)+\text{c.c.}]+\nu_{00}\partial_\varphi p_0+\sum_{\beta>0}\nu_{0\beta}\partial_\varphi p_\beta, \tag{5.17}$$

and, for $\alpha>0$,

$$\lambda_\alpha p_\alpha+[\partial_u(K_r p_\alpha)+\text{c.c.}]+\sum_{\beta>0}k_{\alpha\beta}p_\beta-\sum_{\beta>0}\nu_{\alpha\beta}\partial_\varphi p_\beta\approx -k_{\alpha0}p_0+\nu_{\alpha0}\partial_\varphi p_0. \tag{5.18}$$

To first order in θ^{-1}, the quasi-stationary solution of $p_{\alpha>0}$ is (p_α adiabatically follows p_0)

$$p_{\alpha>0}=\frac{1}{\lambda_\alpha}\big[-k_{\alpha0}p_0+\nu_{\alpha0}\partial_\varphi p_0\big]+O(\theta^{-2}). \tag{5.19}$$

Using the above approximation for $p_{\alpha>0}$ in the equation for p_0, Eq. (5.17), we arrive at

$$\begin{aligned}\partial_\tau p_0 &= -[\partial_u(K_r p_0)+\text{c.c.}]+\partial_\varphi\Big[\Big(\nu_{00}-\sum_{\beta>0}\frac{\nu_{0\beta}k_{\beta0}}{\lambda_\beta}\Big)p_0\Big]+\Big(\sum_{\beta>0}\lambda_\beta^{-1}\nu_{0\beta}\nu_{\beta0}\Big)\partial_\varphi^2 p_0\\ &\quad +a^{(2)}\theta^{-2}\partial_\varphi^3 p_0+a^{(3)}\theta^{-3}\partial_\varphi^4 p_0+\cdots,\end{aligned} \tag{5.20}$$

where the coefficients $a^{(n)}(|u|,\varphi) \sim O(1)$. It is tempting to dismiss the terms in the second line of Eq. (5.20) for $\theta \gg 1$. This is possible if $\theta^{-n}|\partial_\varphi^n p_0| \gg \theta^{-(n+1)}|\partial_\varphi^{(n+1)} p_0|$ for $n \geq 2$. If the stationary solution of Eq. (5.20) has the Eikonal form $p_0^{st} \sim \exp\big(-\theta S(|u|,\varphi)\big)$, the latter inequality essentially requires that $|\partial_\varphi S|^n \ll 1$. This can be verified near the maxima of p_0^{st}; i.e., near the stationary points u_{st} predicted by the mean field theory cf. Eq. (5.6). Mean field theory results if we consider only the zeroth order in θ^{-1} terms of Eq. (5.20). Near the points u_{st}, the first order in θ^{-1} terms of Eq. (5.20) give the leading contribution to the oscillator probability density, $p_0(u,u^*,t)$. In this approximation we have phase diffusion with diffusion coefficient $\mathcal{D} \propto 1/D$ given by

$$\begin{aligned}
\mathcal{D} &= \int_0^\infty d\tau \left\langle \big[\nu(z(\tau)) - \langle \nu(z(\tau))\rangle_a\big]\nu(z(0))\right\rangle_a, \\
&= \int_0^\infty d\tau \int_{-1/2}^{1/2} dz \int_{-1/2}^{1/2} dz_0\, \nu(z)\nu(z_0)P(z,\tau|z_0,0)\psi_0(z_0) - \nu_{00}^2, \\
&= \sum_{\alpha>0} \lambda_\alpha^{-1}\nu_{0\alpha}\nu_{\alpha 0}, \qquad (5.21)
\end{aligned}$$

where the average $\langle\cdot\rangle_a$ is taken over realizations of $z(\tau)$ given by Eq. (5.13) with fixed $|u|$ and $P(z,\tau|z_0,0) = \sum_\alpha e^{-\lambda_\alpha \tau}\psi_\alpha(z)\bar{\psi}_\alpha(z_0)$ is the probability that the particle gets to z at time τ given that it was at z_0 at time 0.

Far from the points u_{st}, we only have that $|\partial_\varphi S| \lesssim 1$ and the terms in the second line of Eq. (5.20) become important. Here, the distribution is not Gaussian and exponentially small. In problems of escape from a basin of attraction of a dynamical system, the escape probability is approximately given by $1/2$ times the probability that the system reaches the saddle point, assuming that at $t \to -\infty$ the particle was at the bottom of the basin of attraction. The factor $1/2$ comes from the probability that the system will actually cross the basin boundary due to small fluctuations.

Figure 5.3 depicts the wedge-like regions of bistability according to the adiabatic picture. If we choose the controlling parameters Ω (scaled frequency detuning) and β_D (scaled drive intensity) well inside the bistability region, the saddle point is far from the two stable points, $u_{st}^{(1,2)}$. Consequently, the switching rates are exponentially small and their calculation requires to take into account all the terms of Eq. (5.20). The calculation simplifies near the lines of bifurcation (boundary of the wedge-like region of bistability) where the saddle point is near one stable point, e.g. $u_{st}^{(1)}$. Thus, the switching rate from the metastable point, $u_{st}^{(1)}$, to the point $u_{st}^{(2)}$, can be calculated by taking into account only the first order term in $\theta^{-1} \ll 1$ of Eq. (5.20).

5.4 Bistability and interstate switching near the adiabatic bifurcation points

The inset of Fig. 5.3 depicts a numerical simulation for the scaled vibrational amplitude, $|u|$, as function of the the scaled time, $\tau = \Gamma t$, for $\Omega = -18.95$, $\beta_D = 5$, and $\bar{\nu} = m\omega_0/2M\Gamma = 10$ (this point in parameter space is close to the adiabatic bifurcation point (ABP): $\Omega_B = -19.145$ for the same values of β_D and $\bar{\nu}$), and $\theta = 1.01$. We note that the system switches between the low- and large- amplitude vibrational states depicted in Fig. 5.2 (a) and (b), respectively. Moreover, the switching rates (reciprocal of the mean residence times) are much smaller than Γ. This shows that the interstate switching events are rare near but not too close to the bifurcation points as long as $\theta \gtrsim 1$. Near the ABPs and for $\theta \gg 1$, we can calculate the switching rates from the metastable vibrational state (large-amplitude state) by considering the reduced equation of motion for the oscillator (in polar coordinates: $u = Re^{i\varphi}$),

$$\begin{aligned} \frac{dR}{d\tau} &= -R - \sin(\varphi), \\ \frac{d\varphi}{d\tau} &= -\big[\Omega + \nu_{00}(R^2)\big] - \frac{\cos(\varphi)}{R} + \mathcal{D}^{1/2}\xi(\tau), \end{aligned} \tag{5.22}$$

where $\mathcal{D}(R)$ is given by Eq. (5.21) and $\xi(\tau)$ is a white and Gaussian noise source with a pair-time correlation function equal to $\langle \xi(\tau_1)\xi(\tau_2)\rangle = 2\delta(\tau_1 - \tau_2)$ and $\delta(\cdot)$ is the Dirac function.

The calculation of the switching rate, W, from the metastable state proceeds as follows. We expand the the right-hand sides of Eq. (5.22) about the bifurcation point in phase space: (R_B, φ_B). Here, it is important to keep the second order terms in $\delta R = R - R_B$ and $\delta\varphi = \varphi - \varphi_B$. The effective phase diffusion coefficient is set to $\mathcal{D}(R_B)$. If we consider only the linear terms δR and $\delta\varphi$, the corresponding linear system has a direction where the drift term vanishes at $\Omega = \Omega_B$. Let us call the coordinate along this direction x_1 and the coordinate along the orthogonal direction x_2 . Then, we have (near a bifurcation point: $\Omega \approx \Omega_B$),

$$\begin{aligned} \frac{dx_1}{d\tau} &= -\delta\Omega/2 - 2x_1 + ax_1^2 + bx_1x_2 + cx_2^2 + O(x_1^3, x_2^3), \\ \frac{dx_2}{d\tau} &= -\delta\Omega/2 + dx_1^2 + ex_1x_2 + gx_2^2 + O(x_1^3, x_2^3), \end{aligned} \tag{5.23}$$

where $\delta\Omega = \Omega - \Omega_B$ and $a > 0, b < 0, c < 0, d > 0, e > 0, g > 0$ are constants depending on R_B and φ_B. From the above equations, we adiabatically eliminate x_1 by setting $\dot{x}_1 = 0$ and then $x_1 \approx -\delta\Omega/4$. The equation for the slow dynamic variable x_2 is

$$\frac{dx_2}{d\tau} \approx d(\delta\Omega/4)^2 - e(\delta\Omega/4)x_2 - \delta\Omega/2 + gx_2^2 + (\mathcal{D}/4)^{1/2}\xi(\tau). \tag{5.24}$$

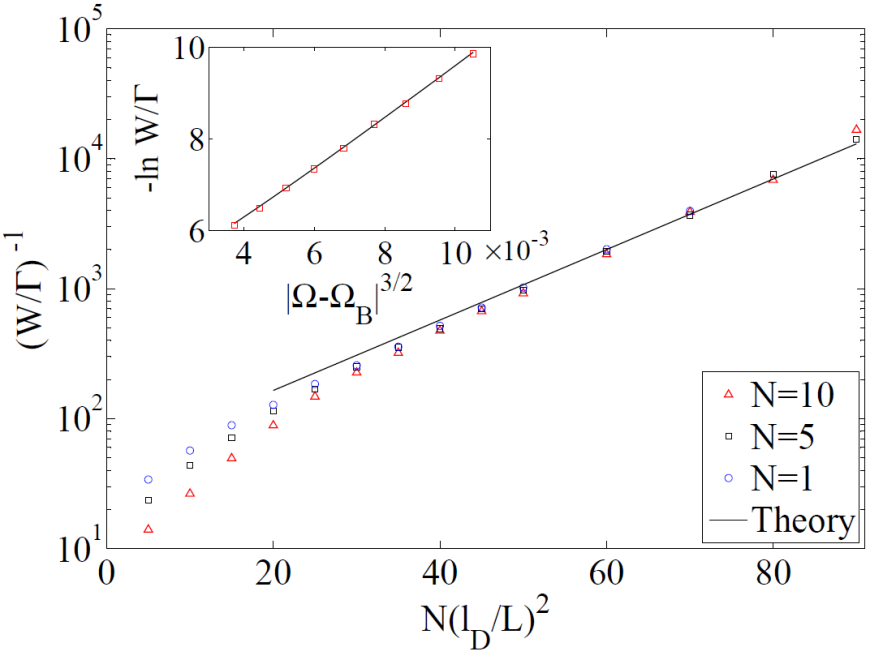

Figure 5.4: The switching rate W near a bifurcation point as function of the product of the diffusion coefficient D and the number of particles N for $\beta_D = 5$, $\bar{\nu} = 10$ and $\Omega - \Omega_B = 0.03$ ($\Omega_B = -19.145$). Inset: scaling of $\ln W/\Gamma$ with the distance to the bifurcation point $\Omega - \Omega_B$ for the same β_D and $\bar{\nu}$; $\theta = 5.1$ and $N = 1$. The discrete points are the results of simulations, the solid lines show the analytical predictions.

Neglecting the first two terms at the right-hand side of the above equation for $|\delta\Omega| \ll 1$, we find the standard Kramer's escape problem of an overdamped Brownian particle escaping from the metastable potential: $U(x_2) = (\delta\Omega/2)x_2 - gx_2^3/3$. The escape rate, W, is given by

$$W \sim \exp\left[-\Delta U/(\mathcal{D}/4)\right] \tag{5.25}$$

where $\Delta U \propto |\Omega - \Omega_B|^{3/2}$ is the effective barrier height that system must overcome in order to escape to the other basin of attraction. Notice that the exponent of the switching rate scales with the distance to the bifurcation point as $|\Omega - \Omega|^{3/2}$. The power $3/2$ is what one should expect if the fluctuations or noise leading to the escape are effectively Gaussian and white. This is what I find in numerical simulations, cf. inset of Fig. 5.4. I emphasize that the $3/2$-scaling is valid only near the adiabatic bifurcation points. Other types of scaling have been predicted for the scape rates in other dynamical systems far from bifurcation points [81].

5.5 Experimental realization of DIB

In order to observe DIB it is necessary that $\beta_D \approx mA^2\omega_0^2/2k_BT \gtrsim \beta_{min}$ (cf. Fig. 5.3) and $L^2\Gamma \lesssim D \lesssim L^2(\omega_0/2\pi)$. Here, A is the vibrational amplitude, ω_0 is the bare eigenfrequency, $\Gamma = \omega_0/2Q$ is the energy relaxation rate of the driven mode, Q is the quality factor, L is the resonator length, m and D are the mass and diffusion coefficient of the diffusing particles, respectively, and k_BT is the thermal energy.

CNT resonators are probably the best candidate to observe DIB. Recently, Chaste et al. have managed to make very short CNT resonators working at low temperatures $T \gtrsim 6K$ with parameters: $\omega_0/2\pi \approx 2$ GHz (fundamental flexural mode), $L \approx 150$ nm, diameter $d \approx 1.7$ nm, mode effective mass $M \approx 3 \times 10^{-19}$ g and quality factor $Q \gtrsim 10^3$. They have demonstrated that CNT resonators can be used as mass sensors with yoctogram resolution (1 yg =10^{-24} g) after current annealing the CNT to eliminate contaminants. They have also seen the frequency dips when Xenon atoms or naphthalene molecules are adsorbed on the CNT [25,33]. For Xenon atoms ($m \approx 2.2 \times 10^{-25}$ Kg), and assuming $A = 1$ nm, I find that $\beta_D \approx 0.2$. The latter value for β_D marginally satisfies the condition for DIB when there are $N \gtrsim 10$ Xe atoms on the CNT [$\beta_{min} \lesssim 0.2$ for $\bar{\nu} = Nm\omega_0/2M\Gamma \approx 27.5$ with $N = 10$]. The diffusion coefficient should be in the range 2.25×10^{-4} cm^{2}s$^{-1} < D < 0.45$ cm^{2}s^{-1}.

CHAPTER 6

Spintronics-based mesoscopic heat engine

In this chapter I present a quantum mechanical description of a mesoscopic heat engine, which has the simplest possible components; namely, a quantum harmonic oscillator (mechanical element) and a two level system (working substance). The latter is directly connected to two heat reservoirs held at different temperatures. I find that there exist three distinct regimes of operation of the heat engine; namely, cooling, heating and heat engine regimes. In both cooling and heating regimes, the vibronic distribution of the oscillator has a Boltzmann form with a certain effective temperature. The latter is smaller (larger) than the temperature of the cold (hot) reservoir in the cooling (heating) regime. In the heat engine regime, the Wigner distribution of the oscillator acquires a nonGaussian form. Its shape corresponds to a circular trajectory (with center at the origin) in phase space, cf. Fig. 6.4. Here, the oscillator develops sustained self oscillations, which can be thought of as the cycles of, e.g., a Stirling heat engine. Below, I consider a possible physical realization of a mesoscopic heat engine which can be used, e.g., to cool the fundamental flexural mode of a nanotube resonator.

6.1 Physical realization of a mesoscopic heat engine

I consider a mesoscopic heat engine which consists of a mechanical subsystem and a pair of spin polarized electrodes (baths) held at different temperatures with opposite spin polarizations. The left (right) electrode has spin polarization $\uparrow$ ($\downarrow$) along the z direction. No bias voltage is applied between the electrodes. The mechanical subsystem is the fundamental flexural mode of a carbon nanotube resonator suspended between the ferromagnetic electrodes, cf. Fig. 6.1. This structure has been recently realized experimentally [41]. The working substance is composed of electrons which flow along the nanotube under certain conditions. When the electrodes are 100 percent spin polarized, the current is zero if there is no spin-flipping mechanism inside the nanotube. The spin-flipping mechanism is induced by a nonuniform magnetic field, localized near the nanotube, as depicted in Fig. 6.1. When the nanotube is at its rest position ($x = 0$), only the z component of the magnetic field, B_z, is non

zero and it induces inside the nanotube an electronic two level system (TLS) with Zeeman energy $\Delta = \epsilon_\uparrow - \epsilon_\downarrow$. The energy of the spin-up (spin-down) level of the TLS is $\epsilon_\uparrow(\epsilon_\downarrow)$. The motion of the nanotube induces coherent transitions between the TLS levels due to the x component of the external magnetic field, B_x, which is assumed to vary as $B_x(x) \approx B'_x(x=0)x$. These coherent transitions are modeled by the following (*spin-mechanical* coupling) term in the Hamiltonian of the nanotube system,

$$H_{sm} = g\hat{u}\big(\hat{d}^\dagger_\uparrow \hat{d}_\downarrow + \hat{d}^\dagger_\downarrow \hat{d}_\uparrow\big), \tag{6.1}$$

where $\hat{d}_\sigma$ ($\hat{d}^\dagger_\sigma$) is the annihilation (creation) operator for electrons in the σ-level of the TLS, $\hat{u} = (\hat{b}^\dagger + \hat{b})/\sqrt{2}$ is the (dimensionless) nanotube displacement operator, and $\hat{b}$ ($\hat{b}^\dagger$) is the annihilation (creation) operator of mechanical quanta of the fundamental flexural mode of the nanotube. The spin-mechanical coupling factor g is proportional to $\mu_B x_0 B'_x(0)$, where $x_0 \equiv (\hbar/M\omega_0)^{1/2} \sim 10$ pm is the vibrational amplitude of the nanotube at its mechanical ground state and μ_B is the Bohr magneton. I assume that the fundamental flexural mode has an effective mass $M \approx 10^{-21}$ kg and resonance frequency $\omega_0 = 2\pi \times 100$ MHz.

Below, I consider the case of weak spin-mechanical coupling and also weak electronic coupling between the nanotube and the electrodes. Specifically, I assume that $g/\hbar$ and the tunneling rate at the left (right) junction, $\Gamma_{L(R)}$, are much smaller than the vibrational frequency; i.e., $\omega_0 \gg g/\hbar, \Gamma_{L,R}$. I also assume the resonance condition $\Delta = \hbar\omega_0$.

The operators $\hat{d}^\dagger_\uparrow \hat{d}_\downarrow$ and $\hat{b}$ vary in time as $\exp\big(it\Delta/\hbar\big)$ and $\exp(-i\omega_0 t)$, respectively, in the interaction picture. If we neglect the fast oscillating terms in the Hamiltonian (rotating wave approximation), the following simplified version of Eq. (6.1) results,

$$H_{sm} = \frac{g}{\sqrt{2}}\big(\hat{d}^\dagger_\uparrow \hat{d}_\downarrow \hat{b} + \text{H.c.}\big), \tag{6.2}$$

which describes the following coherent transitions within the nanotube subsystem,

$$|n+1,\downarrow\rangle \;\rightarrow\; |n,\uparrow\rangle \quad \text{(cooling process)}, \tag{6.3}$$

$$|n,\uparrow\rangle \;\rightarrow\; |n+1,\downarrow\rangle \quad \text{(heating process)}. \tag{6.4}$$

Above, $|n,\sigma\rangle$ is the state where the mechanical subsystem is in the nth Fock state and the TLS is in the σ-spin level [$\sigma = \uparrow,\downarrow$]. Note that the cooling (heating) process decreases (increases) by one the number of mechanical quanta in the mechanical subsystem.

In the absence of coupling to the electrodes, Eqs. (6.3)-(6.4) imply that the transition rate between the TLS levels is $\sim g\sqrt{n+1}$. In order to favor the cooling (heating) process, it is necessary that the occupation probability of the $\sigma = \downarrow$ ($\sigma = \uparrow$) level to be higher than the occupation probability of the $\sigma = \uparrow$

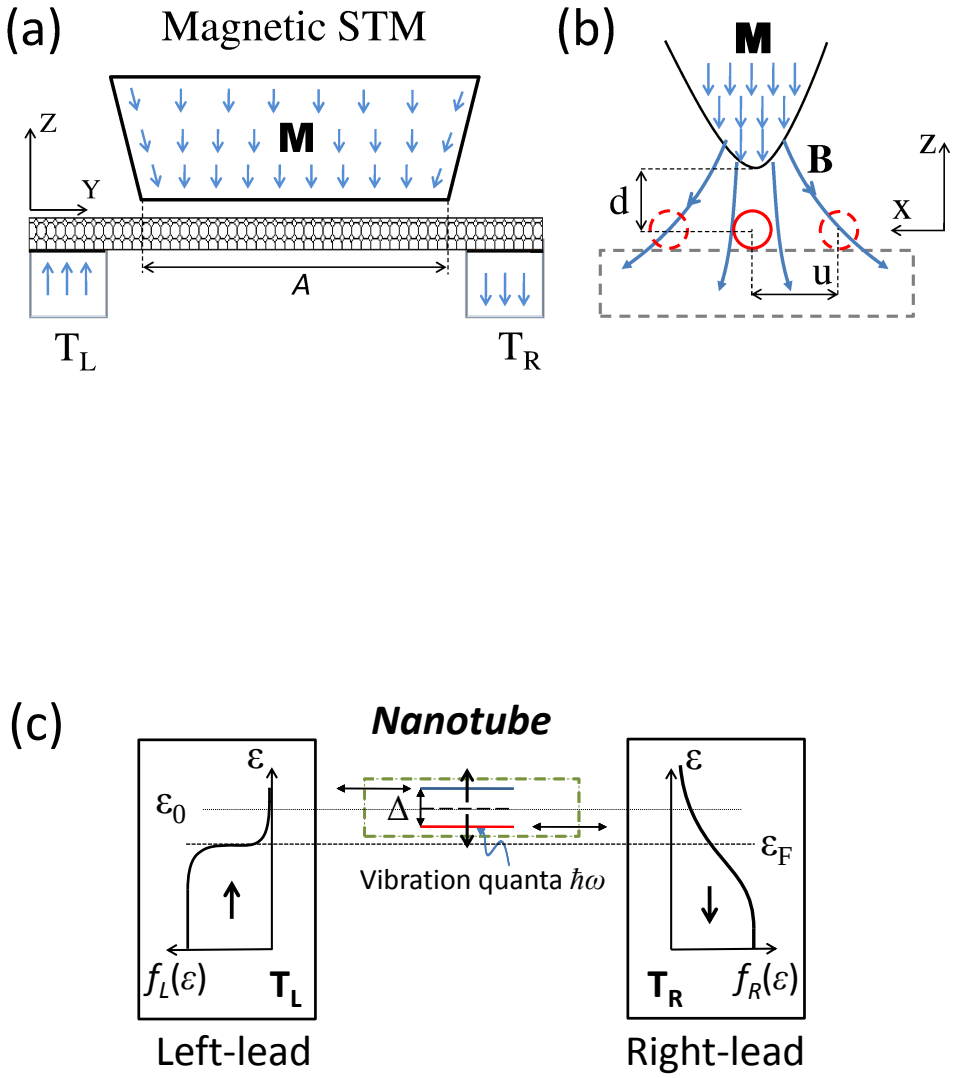

Figure 6.1: (a) A nanotube suspended between two spin-polarized leads and in proximity to a magnetic STM tip with magnetization **M**. The leads have opposite polarizations along the z direction. (b) Nonuniform magnetic field, **B**, created by the magnetic tip. The nanotube (circles) deflection, u, is in the x direction. (c) A doubly spin-degenerate electronic level exists in the nanotube at energy ϵ_0. The applied magnetic field splits this level into two levels $\sigma_z = \uparrow, \downarrow$ separated by an energy $\Delta \propto B_z \mu_B$. The leads are held at different temperatures $T_{L,R}$ with a zero bias voltage.

($\sigma = \downarrow$) level. This is achieved by coupling the nanowire system with electrodes at different temperatures [82] or different electrochemical potentials [83–86]. In particular, for the situation depicted in Fig. 6.1, effective cooling (heating) of the mechanical subsystem is achieved if the temperature of the right (left) electrode, T_R (T_L), is larger than the temperature of the left (right) electrode.

6.2 The effective temperature of the mechanical subsystem

In this section I discuss the result for the effective temperature, T^{eff}, of the mechanical subsystem. It turns out that T^{eff} can be made smaller (*cooling regime*) or larger (*heating regime*) than the temperature of both electrodes. In the cooling (heating) regime the heat engine works as a refrigerator (heat pump). There is also a regime of sustained self oscillations of the mechanical subsystem similar to the cycles of, e.g., a Stirling engine. In this regime the equilibrium position at $u = 0$ of the oscillator becomes unstable and self oscillations develop with a finite amplitude but random phase, cf. Fig. 6.4. I refer to this regime as the *heat engine regime*.

The effective temperature, T^{eff}, of the mechanical subsystem in the cooling and heating regimes can be found by an argument based on detailed balance (In paper VI, I use a method based on the Liouville-von Neumann equation to investigate also the regime of sustained self oscillations where detailed balance does not hold). If the mechanical subsystem exhibits detailed balance, then the following holds,

$$\begin{aligned} \frac{P_m(n+1)}{P_m(n)} &= \frac{\Gamma_{up}(n)}{\Gamma_{down}(n+1)}, \\ &= \frac{n_B}{n_B+1}, \end{aligned} \tag{6.5}$$

where $P_m(n) = (1+n_B)^{-1}\exp\big(-\hbar\omega_0 n/k_B T^{eff}\big)$ is the stationary distribution of the mechanical subsystem, $\Gamma_{down}(n+1)$ gives the transition rate from the $(n+1)$th Fock state to the nth Fock state [cooling process, cf. Eq. (6.3)], $\Gamma_{up}(n)$ gives the transition rate from the nth Fock state to the $(n+1)$th Fock state [heating process, cf. Eq. (6.4)], and $n_B = [\exp(\hbar\omega_0/k_B T^{eff}) - 1]^{-1}$.

For the case of the spintronics-based mesoscopic heat engine, we have

$$\frac{\Gamma_{up}(n)}{\Gamma_{down}(n+1)} = \frac{f_L \cdot \sqrt{n+1}g \cdot (1-f_R)}{f_R \cdot \sqrt{n+1}g \cdot (1-f_L)}, \tag{6.6}$$

where $f_{L(R)} \equiv f_F[(\epsilon_{\uparrow(\downarrow)} - \epsilon_{FL(R)})/k_B T_{L(R)}]$, f_F is the Fermi-distribution, and $\epsilon_{FL(R)}$ is the Fermi energy of the left (right) lead. Inserting Eq. (6.6) into Eq. (6.5), we find that the effective temperature, T^{eff}, of the mechanical subsystem is

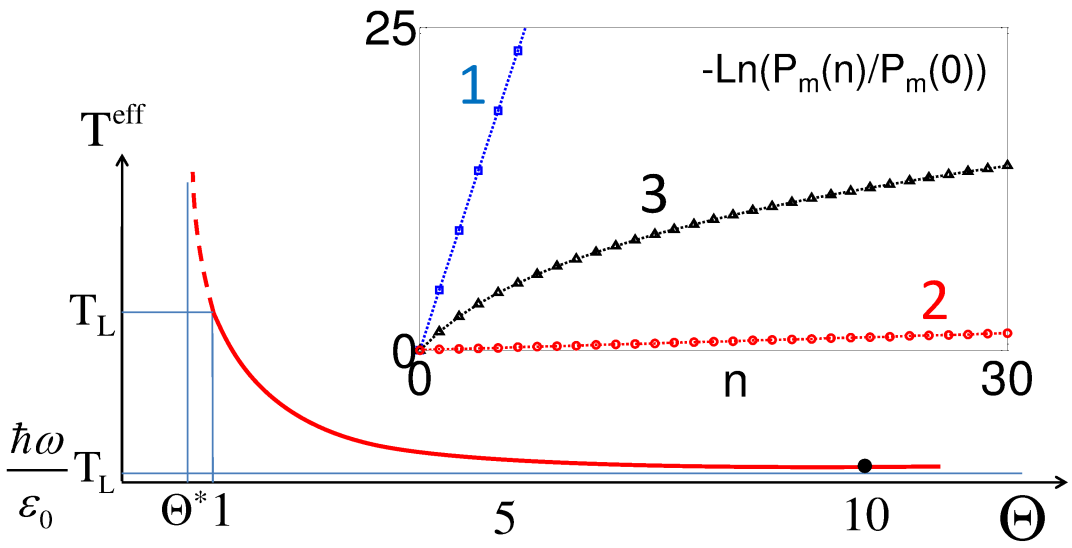

Figure 6.2: Effective temperature T^{eff} of the vibrational mode as function of the ratio $\Theta = T_R/T_L$. For $\Theta > 1$: $T^{eff} < \min\{T_L, T_R\}$ (cooling regime). For $\Theta^* < \Theta < 1$: $T^{eff} > \max\{T_L, T_R\}$ (heating regime). For $\Theta < \Theta^*$: no stationary distribution exits unless additional dissipation mechanisms are included (heat engine regime). Inset: Vibron stationary distribution in logarithmic scale when the mechanical subsystem interacts only with ferromagnetic leads (curve 1), only with a bosonic bath at temperature T_b and coupling parameter γ (curve 2) and, both the fermionic and bosonic baths (curve 3). We use $\omega_0/2\pi = 100$ MHz, $T_L = 0.02$ K, $\Theta = 10$, $T_b = (T_L + T_R)/2$, $\epsilon_0 = k_B T_R/2$, $\Gamma_L = \sqrt{2}g/\hbar$, $\Gamma_R = 1.62g/\hbar$ and $\gamma = 0.002g/\hbar$.

equal to

$$T^{eff} = T_L \frac{\hbar\omega_0}{\epsilon_0}\left[1 - \Theta^{-1} + \frac{\hbar\omega_0}{2\epsilon_0}\left(1 + \Theta^{-1}\right)\right]^{-1}, \tag{6.7}$$

where $\Theta = T_R/T_L$ and $\epsilon_0 = (\epsilon_\uparrow + \epsilon_\downarrow)/2$ is the zero field energy of the TLS inside the nanotube. Equation (6.7) gives the effective temperature for the mechanical subsystem in the case where the latter interacts only with the spin polarized leads through the TLS.

Figure 6.2 depicts the results for the effective temperature, T^{eff}, of the mechanical subsystem as function of $\Theta = T_R/T_L$. For $\Theta < \Theta^* \equiv (1-\hbar\omega_0/2\epsilon_0)/(1+\hbar\omega_0/2\epsilon_0)$, Eq. (6.7) gives $T^{eff} < 0$ and there is no stationary vibron distribution (a stationary distribution, $P_m(n)$, exists if the mechanical subsystem also interacts with other thermal baths, cf. paper VI). This is the heat engine regime where mechanical self oscillations develop, cf. Fig. 6.4. For $\Theta^* < \Theta < 1$, the mechanical subsystem acquires an effective temperature that is larger than the temperature of both leads; this is the heating regime. For $\Theta > 1$, the mechanical subsystem acquires an effective temperature that is smaller than the

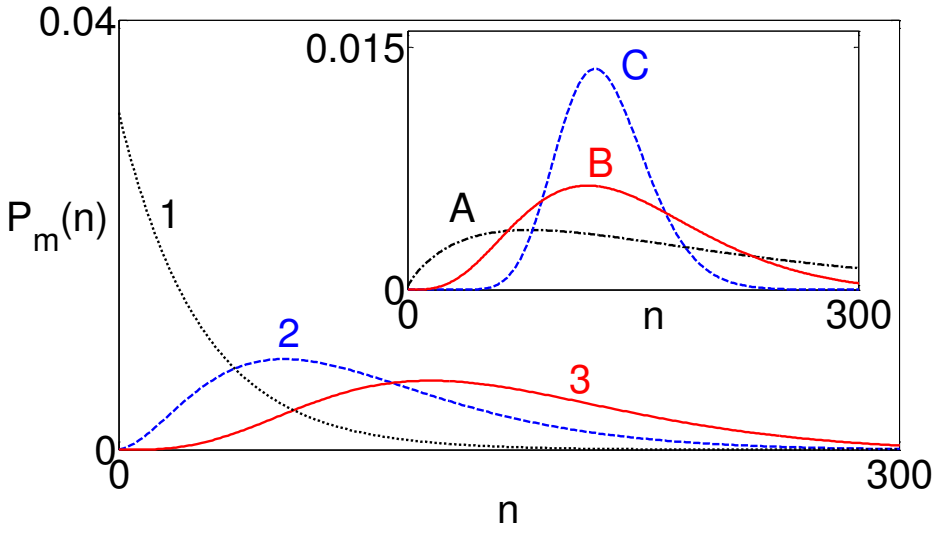

Figure 6.3: Vibron stationary distribution $P_m(n)$ when $\Theta < \Theta^*$. We include a bosonic bath with temperature T_b and coupling parameter γ. The stationary distribution exhibits a peak at n_{max}, which increases as γ gets smaller. We use $n_b\gamma\hbar/g \gg 1$ (curve 1), $n_b\gamma\hbar/g = 0.021$ (curve 2) and $n_b\gamma\hbar/g = 0.01$ (curve 3). Inset: The width of the distribution $P_m(n)$ scales inversely with T_b. $T_b(A) = 1.5$ K, $T_b(B) = 0.3$ K, $T_b(C) = 0.06$ K and $n_b\gamma\hbar/g = 0.01$ for all curves A, B and C.

temperature of both leads; this is the cooling regime. Here, T^{eff} is always greater than $T^{eff}_{min} = 2T_L/(1 + 2\epsilon_0/\hbar\omega_0)$, approaching this value as $\Theta \to \infty$. In other words, the mechanical subsystem does not achieve its mechanical ground state because there exist infrequent heating processes due to the finite temperature of the cold lead. Nevertheless, the average vibron number $\langle n\rangle = \sum_n nP_m(n) \sim \exp(-\epsilon_0/k_BT_L)$ can be exponentially small if $\epsilon_0 \gg k_BT_L$.

Figure 6.3 depicts the vibron stationary distribution, $P_m(n)$, in the heat engine regime ($\Theta < \Theta^*$). Here, the mechanical subsystem also interacts with a bosonic bath at temperature $T_b = (T_L + T_R)/2$ with a coupling factor γ (γ determines the oscillator energy relaxation rate due to coupling with the bosonic bath, cf. paper VI). Clearly, the stationary distribution is not of the Boltzmann form since detailed balance does not hold in the heat engine regime. The stationary distribution has a maximum at $n_{max} \sim \Gamma/\gamma$ where $\Gamma = \min\{\Gamma_L, \Gamma_R\}$.

Figure 6.4 depicts the Wigner distribution of the stationary state of the mechanical subsystem for the three regimes of the spintronics-based heat engine (weak interaction with a bosonic bath is assumed). In particular, in the heat engine regime, the vibrational mode has a finite vibrational amplitude but arbitrary phase. From a classical point of view, the stationary state observed in Fig. 6.4 (for $\Theta < \Theta^*$) is similar to a classical Van der Pol oscillator with a nonlinear friction coefficient, $\Gamma^{eff}(n)$, depicted in Fig. 6.5. For small vibra-

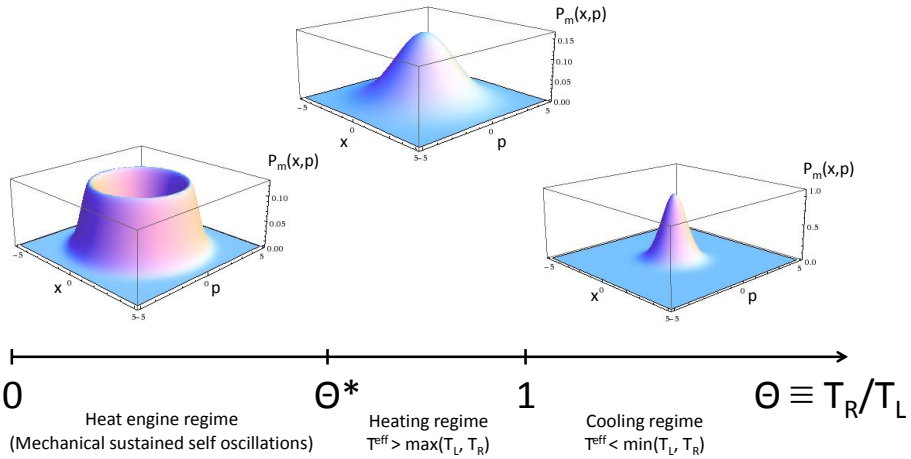

Figure 6.4: Wigner distribution, $P_m(x,p)$, of the stationary state of the mechanical subsystem corresponding to the three regimes of the spintronics-based heat engine; namely, heat engine regime ($\Theta < \Theta^*$), heating regime ($\Theta^* < \Theta < 1$) and cooling regime ($\Theta > 1$).

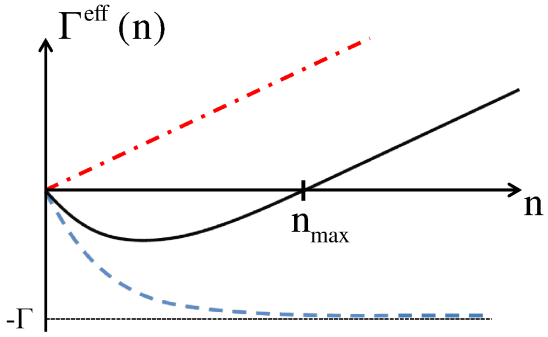

Figure 6.5: Oscillator effective damping rate, $\Gamma^{eff}(n)$, in the heat engine regime (cf. Figs. 6.3 and 6.4) as function of the oscillator quantum number n (solid line). The dashed line represents the contribution due to the heating processes, cf. Eq. (6.4); it saturates at $\Gamma = \min\{\Gamma_L, \Gamma_R\}$ and it has a slope $\propto g$ for small n. The dashed dotted line represents the contribution due to the bosonic thermal bath. This curve has a constant slope, $\propto \gamma$, where γ determines the oscillator quality factor, $Q \propto \omega_0/\gamma$.

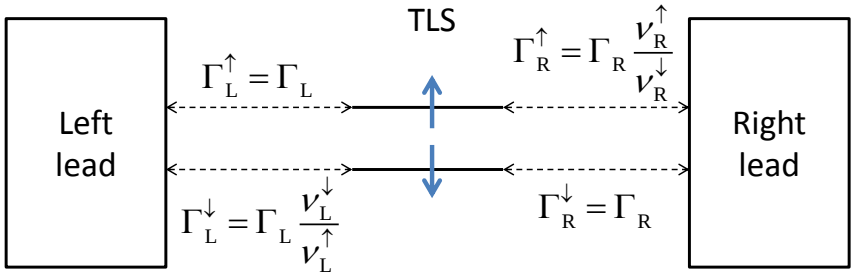

Figure 6.6: Transition rates between leads with partial spin polarization and the TLS.

tional amplitudes ($|u| \lesssim (\hbar n_{max}/M\omega_0)^{1/2}$) we have negative damping and for large vibrational amplitudes we have positive damping. Hence, the stationary point at $u = 0$ becomes unstable and the dynamical system develops an attractor in the form of a limit cycle with a finite amplitude $\approx (\hbar n_{max}/M\omega_0)^{1/2}$ but with a random phase, cf. Fig. 6.4 for $\Theta < \Theta^*$.

6.3 The case of leads with partial spin polarization

In this section I discuss the situation where the leads are partially spin polarized. In order to quantify the spin polarization I introduce the parameter $\eta_{L(R)}$, defined by

$$\eta_{L(R)} = 1 - \frac{\nu_{L(R)}^{\downarrow(\uparrow)}}{\nu_{L(R)}^{\uparrow(\downarrow)}}, \tag{6.8}$$

where $\nu_{L(R)}^{\uparrow}$ and $\nu_{L(R)}^{\downarrow}$ are the density of states with spin $\uparrow$ and $\downarrow$ at the left (right) lead, respectively. Figure 6.6 depicts the transition rates between the TLS and the partially spin polarized leads. The Lindblad master equation for the system is

$$\partial_t \rho = -\frac{i}{\hbar}[H_{nw}, \rho] + \sum_{\alpha=L,R;\,\sigma=\uparrow,\downarrow} \Gamma_\alpha^\sigma \mathcal{L}_{\alpha\sigma}, \tag{6.9}$$

where ρ and H_{nw} are the reduced density matrix and Hamiltonian of the nanotube system (cf. paper VI), respectively, and the rates Γ_α^σ are given in Fig. 6.6. The operators $\mathcal{L}_{\alpha\sigma}$ are defined by

$$\mathcal{L}_{\alpha\sigma}[\rho] = (1 - f_{\alpha\sigma})\hat{d}_\sigma \rho \hat{d}_\sigma^\dagger + f_{\alpha\sigma}(\hat{d}_\sigma^\dagger \rho \hat{d}_\sigma - \rho) - (1/2 - f_{\alpha\sigma})\{\hat{d}_\sigma^\dagger \hat{d}_\sigma, \rho\}, \tag{6.10}$$

where $\{\hat{A},\hat{B}\}$ denotes anticommutator, $f_{\alpha\sigma} = f_F[(\epsilon_\sigma - \epsilon_{F\alpha})/k_BT_\alpha]$, f_F is the Fermi distribution and $\epsilon_{F\alpha}$ is the Fermi level of the α lead. The stationary vibron distribution $P_m^{st}(n)$ has again a Boltzmann form with effective temperature T^{eff} given by

$$\exp\left(-\hbar\omega_0/k_BT^{eff}\right) = \frac{\left[(1-f_{R\downarrow})\Gamma_R^{\downarrow} + (1-f_{L\downarrow})\Gamma_L^{\downarrow}\right]\cdot\left[\Gamma_L^{\uparrow}f_{L\uparrow} + \Gamma_R^{\uparrow}f_{R\uparrow}\right]}{\left[f_{R\downarrow}\Gamma_{R\downarrow} + f_{L\downarrow}\Gamma_L^{\downarrow}\right]\cdot\left[\Gamma_L^{\uparrow}(1-f_{L\uparrow}) + (1-f_{R\uparrow})\Gamma_R^{\uparrow}\right]}. \quad (6.11)$$

I point out that if the leads are not spin polarized [$\eta_{L(R)} = 0$], then the effective temperature of the mechanical subsystem is smaller than $\max\{T_L,T_R\}$ and larger than $\min\{T_L,T_R\}$. The correction to the average vibron number due to partial spin polarization of the leads is [assuming $T_L = 0$ and $(1-\eta_\alpha) \ll 1$],

$$\langle n\rangle \approx \langle n\rangle_{\eta_\alpha=1} + \frac{\Gamma_R(1-f_{R\downarrow})f_{R\uparrow}}{\Gamma_L f_{R\downarrow}}(1-\eta_R). \quad (6.12)$$

6.4 Mechanical ground-state cooling

In this section I discuss the conditions for the mechanical subsystem to reach a stationary state with minimum average vibron number, $\langle n\rangle$. Here, I have to consider the possibility that the mechanical subsystem also interacts with the phononic thermal baths of the electrodes. For symmetric coupling, the effect of these baths is modeled by a single bosonic bath with temperature $T_b = (T_L+T_R)/2$ and coupling factor γ (i.e., the intrinsic oscillator quality factor is $Q = \omega_0/2\gamma$). The dissipation Lindblad operator, $\mathcal{L}_b$, due to the bosonic bath is given by

$$\mathcal{L}_b[\rho] = (n_b+1)\left(2b\rho b^\dagger - b^\dagger b\rho - \rho b^\dagger b\right) + n_b\left(2b^\dagger\rho b - bb^\dagger\rho - \rho bb^\dagger\right), \quad (6.13)$$

where $n_b = [\exp(\hbar\omega_0/k_BT_b) - 1]^{-1}$.

In the absence of coupling between the mechanical subsystem and the bosonic bath, the minimum average vibron number is obtained in the limit $\Theta \equiv T_R/T_L \gg 1$ and $\epsilon_0 \gg \hbar\omega_0$ [cf. Eq. (6.7)]. In the presence of coupling between the mechanical subsystem and the bosonic bath, mechanical ground state cooling [$\langle n\rangle \lesssim 1$] can be achieved if the maximum cooling rate $\sim gf_R$ (this cooling rate is obtained if $\Gamma_R(1-f_R) \lesssim g/\hbar \lesssim \Gamma_L$) is larger than the heating rate due to coupling to the bosonic bath, i.e.,

$$gf_R \gg \hbar\omega_0 n_b/Q.$$

Our analysis shows that for a nanotube with a fundamental flexural mode with resonance frequency $\omega_0 = 2\pi\cdot 100$ MHz ($\hbar\omega/k_B \approx 6$ mK) and realistic coupling parameter $g \approx 2\pi\cdot 10^6$ Hz (cf. paper VI) and quality factor $Q = 10^5$, the average vibron number can be reduced to $\langle n\rangle = 0.44$ for T_R=200 mK and T_L=20 mK. From Eq. (6.12), I find that ground state cooling of the mechanical vibrations with vibron number $\langle n\rangle \lesssim 1$ can still be achieved with a partial spin polarization of $\eta \gtrsim 50\%$.

CHAPTER 7

Conclusions

In this thesis I have summarized the main results of my PhD research within the field of Nanomechanics. I have discussed modeling of the mechanics of graphene resonators, mass sensing using the nonlinear dynamics of square graphene resonators, dephasing of the underdamped vibrational modes of nanomechanical resonators, and quantum mechanical study of the regimes of operation of a mesoscopic heat engine.

The mechanical description of monolayer graphene is a finite-strain elasticity theory, which can be used to model the (long wavelength) deformations of the membrane in graphene-based resonators, cf. papers I and II. This elasticity theory has been used to study the possibility of using the nonlinear dynamical response of graphene resonators to determine the mass and position of a single particle adsorbed on a square graphene resonator, cf. paper III.

I have also studied the effects of frequency noise, caused by random mass loading of small particles onto the resonator, in the response of underdamped vibrational modes of nanomechanical resonators. I consider a type of mass loading which is relevant for mass sensing applications. Here, the particles enter and leave at arbitrary points on the resonator and also the particles may diffuse along the nanoresonator. The results presented in chapter 4 apply to one-dimensional resonators. However, the main conclusions apply in general to harmonic oscillators with multiplicative noise. The main conclusions are the method of the interfering partial susceptibilities to calculate the oscillator susceptibility, the understanding of the existence of the fast and the slow frequency noise limits. As discussed in chapter 4 and in papers IV and VII, the slow frequency noise limit corresponds to a frequency noise whose correlation time, τ_c, is larger than the oscillator ring down time, Γ^{-1}, and the reciprocal of the standard deviation of the frequency fluctuations, Δ. In this limit, the oscillator susceptibility can deviate significantly from the standard Lorentzian susceptibility of underdamped oscillators. On the opposite limit, i.e. $\tau_c \ll \Gamma^{-1}, \Delta^{-1}$, the oscillator susceptibility tends to a Lorentzian susceptibility.

I have also considered the situation where the frequency noise is affected by the oscillator vibrational state (backaction). In particular, I study diffusion induced bistability of driven nanomechanical resonators where the backaction is induced by an inertial force, which drives the particles towards the

vibrational antinodes. If the particles diffuse comparatively fast along the resonator, the oscillator exhibits nonlinear phenomena in the form of bistability between a large amplitude vibrational state (with particles accumulated at the antinode) and a small amplitude vibrational state (with particles almost uniformly distributed along the resonator), cf. paper V. This type of nonlinear phenomena may have been already observed in recent experiments, performed by Bachtold et al. [25]. They observe sudden upward jumps in the eigenfrequency of the driven mode (fundamental flexural mode of a CNT resonator). These jumps would correspond to switching from the particle mass distribution peaked at the vibrational antinode to the mass distribution which is almost uniformly distributed.

I have also discussed the operation regimes of a spintronics-based mesoscopic heat engine. The latter is composed of spin polarized electrodes (heat baths), held at different temperatures, and the fundamental flexural mode of a carbon nanotube resonator (mechanical subsystem), suspended between the electrodes. I find that the stationary state of the mechanical subsystem is described by an effective temperature, which can be larger (heating regime) or smaller (cooling regime) than the temperatures of the heat baths. Moreover, it is possible to drive sustained mechanical self oscillations (heat engine regime), which can be thought of as the cyclic motion of, e.g., a Stirling heat engine. The mechanical subsystem in this latter regime behaves as a Van der Pol oscillator with nonlinear damping, which is negative (positive) for comparatively small (large) oscillation amplitudes. Here, the stationary state has a finite amplitude but random phase, cf. Fig. 6.5.

My recent research in dephasing of the vibrational modes of nanomechanical resonators indicates that the latter can be used to study surface physics and transport phenomena in nanomechanical resonators. For instance, it has been demonstrated that phase transitions of adsorbed atoms on the surface of carbon nanotubes or the formation of monolayers on the nanotube surface can be studied by monitoring the changes in the resonance frequency of, e.g., the fundamental flexural mode [87]. Here, the fluctuations in the mass density of the adatoms lead to fluctuations in the vibrational frequency (dephasing), which could be characterized by measuring the cumulants of the (complex) amplitude fluctuations of a driven vibrational mode. It is also important to investigate the contribution to dephasing due to typical driving setups of nanoelectromechanical resonators. For instance, electrostatic driving induced dephasing can exist if the charge fluctuations in the nanoresonator or the substrate below are comparatively slow. Similarly to mass loading induced dephasing, the net effect of charge fluctuations with a comparatively short RC time is a weak broadening of the absorption spectrum of the vibrational modes. The effect of the charge fluctuations is significant (e.g., change of shape of the absorption spectrum lines) if the charge fluctuations are comparatively slow. This occurs in poor conductors, where the RC time can be comparable to the oscillator ring down time and to the reciprocal of the typi-

cal size of the induced frequency fluctuations.

Acknowledgements

I would like to thank my supervisor Dr. Andreas Isacsson for his constant support during the realization of the work presented in this thesis. I also would like to thank other scientists with whom I have worked and shared ideas during my PhD research: Prof. Jari M. Kinaret, Prof. Mark I. Dykman and Dr. Leonid Y. Gorelik. I am also grateful to Prof. Mark I. Dykman for kindly hosting me at his research group at Michigan State University during the summer of 2010.

I also would like to thank all the other members of the Condensed Matter Theory Group for creating an stimulating research environment and for their help in work and other matters. I also acknowledge the Swedish VR and SSF for the financial support.

BIBLIOGRAPHY

[1] B. I. Yakobson, C. J. Brabec, and J. Bernholc, "*Nanomechanics of Carbon Tubes: Instabilities beyond Linear Response*", Phys. Rev. Lett. **76**, 2511 (1996).

[2] D. R. Nelson, *Statistical mechanics of membranes and surfaces*. World Scientific Singapore, 2004.

[3] J. Atalaya, A. Isacsson, and J. M. Kinaret, "*Continuum Elastic Modeling of Graphene Resonators*", Nano Lett. **8 (12)**, 4196 (2008).

[4] M. Dykman and M. Krivoglaz, "*Theory of nonlinear oscillator interacting with a medium*", in Soviet Physics Reviews, edited by I.M.Khalatnikov (Harwood Academic, New York) **5**, 265 (1984).

[5] R. B. Karabalin, M. C. Cross, and M. L. Roukes, "*Nonlinear dynamics and chaos in two coupled nanomechanical resonators*", Phys. Rev. B **79**, 165309 (2009).

[6] H. J. R. Westra, M. Poot, H. S. J. van der Zant, and W. J. Venstra, "*Nonlinear Modal Interactions in Clamped-Clamped Mechanical Resonators*", Phys. Rev. Lett. **105**, 117205 (2010).

[7] U. Weiss, *Quantum dissipative systems*. World Scientific, 1999.

[8] A. Croy, D. Midtvedt, A. Isacsson, and J. M. Kinaret, "*Nonlinear Damping in Graphene Resonators*", arXiv:1204.0911v1.

[9] M. D. LaHaye, O. Buu, B. Camarota, and K. C. Schwab, "*Approaching the Quantum Limit of a Nanomechanical Resonator*", Science **304**, 74 (2004).

[10] A. D. O'Connell, M. Hofheinz, M. Ansmann, R. C. Bialczak, M. Lenander, E. Lucero, M. Neeley, D. Sank, H. Wang, M. Weides, J. Wenner, J. M. Martinis, and A. N. Cleland, "*Quantum ground state and single-phonon control of a mechanical resonator*", Nature **464**, 697 (2010).

[11] A. Voje, J. M. Kinaret, and A. Isacsson, "*Generating macroscopic superposition states in nanomechanical graphene resonators*", Phys. Rev. B **85**, 205415 (2012).

[12] F. Marquardt and S. M. Girvin, "*Trend: Optomechanics*", Physics **2**, 40 (2009).

[13] K. L. Ekinci and M. L. Roukes, "*Nanoelectromechanical systems*", Review of Scientific Instruments **76**, 061101 (2005).

[14] B. Lassagne, Y. Tarakanov, J. Kinaret, D. Garcia-Sanchez, and A. Bachtold, "*Coupling mechanics to charge transport in carbon nanotube mechanical resonators*", Science **325**, 1107 (2009).

[15] Y. A. Tarakanov and J. M. Kinaret, "*A Carbon Nanotube Field Effect Transistor with a Suspended Nanotube Gate*", Nano Lett. **7 (8)**, 2291 (2007).

[16] J. Svensson, Y. Tarakanov, D. S. Lee, J. M. Kinaret, Y. W. Park, and E. E. B. Campbell, "*A carbon nanotube gated carbon nanotube transistor with 5 ps gate delay*", Nanotech. **19**, 325201 (2008).

[17] J. Svensson, N. Lindahl, H. Yun, M. Seo, D. Midtvedt, Y. Tarakanov, N. Lindvall, O. Nerushev, J. Kinaret, S. Lee, and E. E. B. Campbell, "*Carbon Nanotube Field Effect Transistors with Suspended Graphene Gates*", Nano Lett. **11 (9)**, 3569 (2011).

[18] J. M. Kinaret, T. Nord, and S. Viefers, "*A carbon-nanotube-based nanorelay*", Appl. Phys. Lett. **82**, 1287 (2003).

[19] Y. T. Yang, C. Callegari, X. L. Feng, K. L. Ekinci, and M. L. Roukes, "*Zeptogram-Scale Nanomechanical Mass Sensing*", Nano Lett. **6**, 583 (2006).

[20] T. P. Burg, M. Godin, S. M. Knudsen, W. Shen, G. Carlson, J. S. Foster, K. Babcock, and S. R. Manalis, "*Weighing of biomolecules, single cells and single nanoparticles in fluid*", Nature **446**, 1066 (2007).

[21] K. Jensen, K. Kim, and A. Zettl, "*An atomic-resolution nanomechanical mass sensor*", Nat. Nanotech. **3**, 533 (2008).

[22] B. Lassagne, D. Garcia-Sanchez, A. Aguasca, and A. Bachtold, "*Ultrasensitive Mass Sensing with a Nanotube Electromechanical Resonator*", Nano Lett. **8**, 3735 (2008).

[23] A. K. Naik, M. S. Hanay, W. K. Hiebert, X. L. Feng, and M. L. Roukes, "*Towards single-molecule nanomechanical mass spectrometry*", Nat. Nanotech. **4**, 445 (2009).

[24] J. Lee, W. J. Shen, K. Payer, T. P. Burg, and S. R. Manalis, "*Toward Attogram Mass Measurements in Solution with Suspended Nanochannel Resonators*", Nano Lett. **10**, 2537 (2010).

[25] J. Chaste, A. Eichler, J. Moser, G. Ceballos, R. Rurali, and A. Bachtold, "*A nanomechanical mass sensor with yoctogram resolution*", Nat. Nanotech. **7**, 301 (2012).

[26] A. N. Cleland and M. L. Roukes, "*A nanometre-scale mechanical electrometer*", Nature **392**, 160 (1998).

[27] D. Rugar, R. Budakian, H. J. Mamin, and B. W. Chui, "*Single spin detection by magnetic resonance force microscopy*", Nature **430**, 329 (2004).

[28] S. S. Verbridge, J. M. Parpia, R. B. Reichenbach, L. M. Bellan, and H. G. Craighead, "*High quality factor resonance at room temperature with nanostrings under high tensile stress*", J. Appl. Phys. **99**, 124304 (2006).

[29] A. K. Hüttel, G. A. Steele, B. Witkamp, M. Poot, L. P. Kouwenhoven, and H. S. J. van der Zant, "*Carbon Nanotubes as Ultrahigh Quality Factor Mechanical Resonators*", Nano Lett. **9 (7)**, 2547 (2009).

[30] E. A. Laird, F. Pei, W. Tang, G. A. Steele, and L. P. Kouwenhoven, "*A High Quality Factor Carbon Nanotube Mechanical Resonator at 39 GHz*", Nano Lett. **12 (1)**, 193 (2012).

[31] A. Geim and K. Novoselov, "*The rise of graphene*", Nat. Materials **6 (3)**, 183 (2007).

[32] A. R. Barton, J. Parpia, and H. G. Craighead, "*Fabrication and performance of graphene nanoelectromechanical systems*", J. Vac. Sci Technol. B **29**, 050801 (2011).

[33] J. Chaste, M. Sledzinska, M. Zdrojek, J. Moser, and A. Bachtold, "*High-frequency nanotube mechanical resonators*", Appl. Phys. Lett. **99**, 213502 (2011).

[34] V. Sazonova, Y. Yaish, H. Üstünel, D. Roundy, T. A. Arias, and P. L. McEuen, "*A tunable carbon nanotube electromechanical oscillator*", Nature **431**, 284 (2004).

[35] A. Eriksson, S. Lee, A. A. Sourab, A. Isacsson, R. Kaunisto, J. M. Kinaret, and E. E. B. Campbell, "*Direct Transmission Detection of Tunable Mechanical Resonance in an Individual Carbon Nanofiber Relay*", Nano Lett. **8 (4)**, 1224 (2008).

[36] F. Cottone, H. Vocca, and L. Gammaitoni, "*Nonlinear Energy Harvesting*", Phys. Rev. Lett. **102**, 080601 (2009).

[37] M. Kac, "*Can One Hear the Shape of a Drum?*", The American Mathematical Monthly **73 (4) Part 2**, 1 (1966).

[38] C. Gordon, D. L. Webb, and S. Wolpert, "*One cannot hear the shape of a drum*", Bull. Amer. Math. Soc. **27**, 134 (1996).

[39] P. G. Steeneken, K. L. Phan, M. J. Goossens, G. E. J. Koops, G. J. A. M. Brom, C. van der Avoort, and J. T. M. van Beek, "*Piezoresistive heat engine and refrigerator*", Nat. Phys. **7**, 354 (2011).

[40] N. Linden, S. Popescu, and P. Skrzypczyk, "*How Small Can Thermal Machines Be? The Smallest Possible Refrigerator*", Phys. Rev. Lett. **105**, 130401 (2010).

[41] L. E. Hueso, J. M. Pruneda, V. Ferrari, G. Burnell, J. P. Valdés-Herrera, B. D. Simons, P. B. Littlewood, E. Artacho, A. Fert, and N. D. Mathur, "*Transformation of spin information into large electrical signals using carbon nanotubes*", Nature **445**, 410–413 (2007).

[42] J. Atalaya, "*Elasticity Theory for Graphene Membranes*", Master's thesis, Dept. of Physics, University of Gothenburg, 2008.

[43] A. Fasolino, J. H. Los, and M. I. Katsnelson, "*Intrinsic ripples in graphene*", Nat. Materials **6**, 858 (2007).

[44] R. Roldán, A. Fasolino, K. V. Zakharchenko, and M. I. Katsnelson, "*Suppression of anharmonicities in crystalline membranes by external strain*", Phys. Rev. B **83**, 174104 (2011).

[45] C. Nisoli, P. E. Lammert, E. Mockensturm, and V. H. Crespi, "*Carbon Nanostructures as an Electromechanical Bicontinuum*", Phys. Rev. Lett. **99**, 045501 (2007).

[46] Y. Huang, J. Wu, and K. C. Hwang, "*Thickness of graphene and single-wall carbon nanotubes*", Phys. Rev. B **74**, 245413 (2006).

[47] M. Arroyo and T. Belytschko, "*Finite crystal elasticity of carbon nanotubes based on the exponential Cauchy-Born rule*", Phys. Rev. B **69**, 115415 (2004).

[48] K. N. Kudin, G. E. Scuseria, and B. I. Yakobson, "*C2F, BN, and C nanoshell elasticity from ab initio computations*", Phys. Rev. B **64**, 235406 (2001).

[49] J. P. Wilber, C. B. Clemons, G. W. Young, A. Buldum, and D. D. Quinn, "*Continuum and atomistic modeling of interacting graphene layers*", Phys. Rev. B **75**, 045418 (2007).

[50] P. N. Keating, "*Effect of Invariance Requirements on the Elastic Strain Energy of Crystals with Application to the Diamond Structure*", Phys. Rev. **145**, 637 (1966).

[51] R. M. Martin, "*Elastic Properties of ZnS Structure Semiconductors*", Phys. Rev. B **1**, 4005 (1970).

[52] C. Lobo and J. L. Martins, "*Valence force field model for graphene and fullerenes*", Z. Phys. D **39(2)**, 159 (1997).

[53] L. D. Landau and E. M. Lifshitz, *Theory of Elasticity*. Pergamon Press, 1959.

[54] A. D. Drozdov, *Finite Elasticity and Viscoelasticity*. World Scientific, 1996.

[55] A. H. Nayfeh and D. T. Mook, *Nonlinear Oscillators*. Wiley-VCH, 2004.

[56] K. Samadikhah, J. Atalaya, C. Huldt, A. Isacsson, and J. M. Kinaret, "*General Elasticity Theory of Graphene Membranes based on Molecular Dynamics*", MRS J. Proceedings **1057-II10-20** (2007 Fall Meeting).

[57] J. S. Bunch, S. S. Verbridge, J. S. Alden, A. M. van der Zande, J. M. Parpia, H. G. Craighead, and P. L. McEuen, "*Impermeable Atomic Membranes from Graphene Sheets*", Nano Lett. **8 (8)**, 2458 (2008).

[58] C. Lee, X. Wei, J. W. Kysar, and J. Hone, "*Measurement of the Elastic Properties and Intrinsic Strength of Monolayer Graphene*", Science **321**, 385 (2008).

[59] C. Chen, S. Rosenblatt, K. I. Bolotin, W. Kalb, P. Kim, I. Kymissis, H. L. Stormer, T. F. Heinz, and J. Hone, "*Performance of Monolayer Graphene Nanomechanical Resonators with Electrical Readout*", Nat. Nanotech. **4**, 861 (2009).

[60] K. L. Ekinci, Y. T. Yang, and M. L. Roukes, "*Ultimate limits to inertial mass sensing based upon nanoelectromechanical systems*", J. Appl. Phys. **95**, 2682 (2004).

[61] G. A. Steele, A. K. Hüttel, B. Witkamp, M. Poot, H. B. Meerwaldt, L. P. Kouwenhoven, and H. S. J. van der Zant, "*Strong Coupling Between Single-Electron Tunneling and Nanomechanical Motion*", Science **325**, 1103 (2009).

[62] A. Eichler, J. Moser, J. Chaste, M. Zdrojek, I. Wilson-Rae, and A. Bachtold, "*Nonlinear damping in mechanical resonators made from carbon nanotubes and graphene*", Nat. Nanotech. **6**, 339 (2011).

[63] J. S. Aldridge and A. N. Cleland, "*Noise-Enabled Precision Measurements of a Duffing Nanomechanical Resonator*", Phys. Rev. Lett. **94**, 156403 (2005).

[64] C. Stambaugh and H. B. Chan, "*Supernarrow Spectral Peaks near a Kinetic Phase Transition in a Driven Nonlinear Micromechanical Oscillator*", Phys. Rev. Lett. **97**, 110602 (2006).

[65] I. Kozinsky, H. W. C. Postma, O. Kogan, A. Husain, and M. L. Roukes, "*Basins of Attraction of a Nonlinear Nanomechanical Resonator*", Phys. Rev. Lett. **99**, 207201 (2007).

[66] J. Atalaya, J. M. Kinaret, and A. Isacsson, "*Nanomechanical mass measurement using nonlinear response of a graphene membrane*", EPL **91(4)**, 48001 (2010).

[67] K. L. Ekinci, X. M. H. Huang, and M. L. Roukes, "*Ultrasensitive nanoelectromechanical mass detection*", Appl. Phys. Lett. **84**, 4469 (2004).

[68] J. S. Aldridge and A. N. Cleland, "*Noise-Enabled Precision Measurements of a Duffing Nanomechanical Resonator*", Phys. Rev. Lett. **94**, 156403 (2005).

[69] H. Risken, *The Fokker-Planck Equation*. Springer, Berlin, 1996.

[70] Z. A. Maizelis, M. L. Roukes, and M. I. Dykman, "*Detecting and characterizing frequency fluctuations of vibrational modes*", Phys. Rev. B **84**, 144301 (2011).

[71] V. Weisskopf and E. Wigner, "*On the natural Broad Lines in the Radiation of the harmonic Oscillators*", Z. Phys. **65**, 18 (1930).

[72] M. I. Dykman, M. Khasin, J. Portman, and S. Shaw, "*Spectrum of an oscillator with jumping frequency and the interference of partial susceptibilities*", Phys. Rev. Lett. **105**, 230601 (2010).

[73] H. Kramers, "*Brownian motion in a field of force and the diffusion model of chemical reactions*", Physica **7**, 284 (1940).

[74] J. Atalaya, A. Isacsson, and M. I. Dykman, "*Diffusion-Induced Bistability of Driven Nanomechanical Resonators*", Phys. Rev. Lett. **106**, 227202 (2011).

[75] P. W. Anderson, "*A mathematical model for the narrowing of spectral lines by exchange or motion*", J. Phys. Soc. Jpn. **9**, 316 (1954).

[76] R. Kubo and K. Tomita, "*A general theory of magnetic resonance absorption*", J. Phys. Soc. Jpn. **9**, 888 (1954).

[77] R. Kubo, "*Note on the stochastic theory of resonance absorption*", J. Phys. Soc. Jpn. **9**, 935 (1954).

[78] J. Atalaya, A. Isacsson, and M. I. Dykman, "*Diffusion-induced dephasing in nanomechanical resonators*", Phys. Rev. B **83**, 045419 (2011).

[79] D. T. Gillespie, "*Exact stochastic simulation of coupled chemical reactions*", J. Phys. Chem. **81**, 2340 (1977).

[80] R. Mannella, "*A Gentle Introduction to the Integration of Stochastic Differential Equations*", Stochastic Processes in Phys. Chem. Biol. **557**, 353 (2000).

[81] M. Parker, A. Kamenev, and B. Meerson, "*Noise-Induced Stabilization in Population Dynamics*", Phys. Rev. Lett. **107**, 180603 (2011).

[82] J. Atalaya and L. Y. Gorelik, "*Spintronics-based mesoscopic heat engine*", Phys. Rev. B **85**, 245309 (2012).

[83] S. Zippilli, G. Morigi, and A. Bachtold, "*Cooling Carbon Nanotubes to the Phononic Ground State with a Constant Electron Current*", Phys. Rev. Lett. **102**, 096804 (2009).

[84] G. Sonne, M. E. Peña-Aza, L. Y. Gorelik, R. I. Shekhter, and M. Jonson, "*Cooling of a Suspended Nanowire by an ac Josephson Current Flow*", Phys. Rev. Lett. **104**, 226802 (2010).

[85] S. Zippilli, A. Bachtold, and G. Morigi, "*Ground-state-cooling vibrations of suspended carbon nanotubes with constant electron current*", Phys. Rev. B **81**, 205408 (2010).

[86] F. Santandrea, L. Y. Gorelik, R. I. Shekhter, and M. Jonson, "*Cooling of Nanomechanical Resonators by Thermally Activated Single-Electron Transport*", Phys. Rev. Lett. **106**, 186803 (2011).

[87] Z. Wang, J. Wei, P. Morse, J. G. Dash, O. E. Vilches, and D. H. Cobden, "*Phase Transitions of Adsorbed Atoms on the Surface of a Carbon Nanotube*", Science **327**, 552 (2010).